Universidade de Brasília

Faculdade de Tecnologia

NUMERICAL STUDY ON THE IMPACT OF BLADE SWEEP ANGLES IN HYDROKINETIC TURBINE EFFICIENCY

Thiago Vieira de Souza

MASTER'S THESIS

GRADUATE PROGRAM IN MECHANICAL SCIENCES

Brasília

2025

Universidade de Brasília

Faculdade de Tecnologia

ESTUDO NUMÉRICO DO IMPACTO DE ÂNGULOS DE CURVATURA DE PÁS NA EFICIÊNCIA DE TURBINAS HIDROCINÉTICAS

Thiago Vieira de Souza

Master's Thesis submitted in partial fulfillment of the requirements for the degree of Master of Science in Mechanical Sciences.

Professor Advisor: Prof. Dr. Taygoara Felamingo de Oliveira

Co-advisor: Prof. Dr. Rafael Castilho Faria Mendes

Brasília

2025

FICHA CATALOGRÁFICA

Vieira de Souza, Thiago.

NUMERICAL STUDY ON THE IMPACT OF BLADE SWEEP ANGLES IN HYDROKINETIC TURBINE EFFICIENCY / Thiago Vieira de Souza; professor advisor Taygoara Felamingo de Oliveira; co-advisor Rafael Castilho Faria Mendes. -- Brasília, 2025.

125 p.

Master's Thesis (Graduate Program in Mechanical Sciences) -- Universidade de Brasília, 2025.

1. Hydrokinetic turbines. 2. Swept blades. 3. CFD. 4. BEM theory. 5. Aerodynamic optimization.I. Felamingo de Oliveira, Taygoara, orient. II. Castilho Faria Mendes, Rafael, coorient. III. Título.

Universidade de Brasília
Faculdade de Tecnologia

NUMERICAL STUDY ON THE IMPACT OF BLADE SWEEP ANGLES IN HYDROKINETIC TURBINE EFFICIENCY

Thiago Vieira de Souza

Master's Thesis submitted in partial fulfillment of the requirements for the degree of Master of Science in Mechanical Sciences.

Trabalho aprovado. Brasília, 30 de outubro de 2025:

Prof. Dr. Taygoara Felamingo de Oliveira,
UnB/FT/PCMec
Orientador

Prof. Dr. Luciano Gonçalvez Noleto,
UnB/FCTE
Examinador interno

Prof. Dr. Jerson Rogério Pinheiro Vaz,
UFPA
Examinador externo

Profa. Dra. Simone Monteiro e Silva,
UnB/PPG-CM
Examinadora interna (suplente)

Dedico este trabalho à minha querida mãe, que cuidou da minha educação desde os primeiros anos, que sempre colocou os sonhos dos filhos à frente dos próprios, que me ensinou a importância de ser um bom profissional e, acima de tudo, um bom ser humano. Sua dedicação inabalável me possibilitou ingressar na universidade e construir uma carreira digna, e ainda hoje continua a velar por mim com o mesmo cuidado e amor.

Agradecimentos

À minha família, por ter me proporcionado as condições necessárias para que eu pudesse me dedicar aos estudos e por ter incentivado minha qualificação profissional. À minha mãe, a quem sempre recorri nos momentos de atribulação, que me motivou ao longo da minha carreira acadêmica e profissional. Aos meus avós, cuja colaboração foi fundamental para minha formação. Ao meu irmão, sempre disposto a oferecer suporte técnico em sua área de conhecimento, além de todo companheirismo e partilha.

À minha amada esposa, que esteve mais próxima de mim do que ninguém, apoiando todas as minhas decisões e tendo paciência infindável para me acompanhar nesta difícil jornada. Obrigado por compreender minha ausência no lar, enquanto eu conciliava trabalho e pós-graduação. Por me estender a mão em cada percalço, por ajudar a tratar as feridas e por me fazer acreditar no meu próprio potencial. Por acalmar minha ansiedade e aliviar meu estresse. Principalmente, por me inspirar a ter ambições e a lutar para crescer, tanto na esfera profissional quanto pessoal.

Aos amigos e amigas que acompanharam de perto os altos e baixos desta trajetória, meu sincero agradecimento. Em especial aos colegas de laboratório Arthur Leite, Ramiro Bertolina e Kaajal Gopie, cujo companheirismo manteve viva a chama da motivação. As risadas, o suporte técnico, as longas noites de estudo e a partilha diária foram fundamentais para o desenvolvimento deste trabalho e para minha formação enquanto pesquisador.

Ao meu coorientador, Dr. Rafael Faria Castilho Mendes, agradeço por toda a atenção e diligência. Sua disponibilidade para se reunir, discutir e pôr as mãos na massa foi essencial. Sempre com bom humor e disposição, compartilhou comigo seu vasto conhecimento e habilidades valiosas, sem as quais este trabalho não teria sido possível.

Finalmente, agradeço ao meu orientador, Dr. Taygoara Felamingo de Oliveira, a mente brilhante com quem tive o privilégio de conviver. Mais do que seu vasto conhecimento técnico, admiro sua capacidade de inspirar e motivar, qualidade que certamente marcou a trajetória de centenas de discentes sob sua tutela, seja como orientandos ou como alunos de suas disciplinas. Obrigado pela paciência, pela forma respeitosa e horizontal de lidar com todos, e por responder efusivamente a qualquer questionamento, por mais trivial que fosse. Obrigado pela sinceridade de seus comentários, pela assertividade das orientações e por acreditar em mim mesmo nos momentos em que eu próprio duvidava.

A cada desafio vencido e a cada passo dado, descobri que este trabalho é menos sobre mim e mais sobre todos que caminharam ao meu lado. Que este não seja o ponto de chegada, mas sim o ponto de partida para os novos empreendimentos que virão.

“Queremos saber
O que vão fazer
Com as novas invenções
Queremos notícia mais séria
Sobre a descoberta da antimatéria
E suas implicações
Na emancipação do homem
[...]
Pois se foi permitido ao homem
Tantas coisas conhecer
É melhor que todos saibam
O que pode acontecer
(Gilberto Gil)"

Abstract

Hydrokinetic turbines represent a promising technology for renewable energy generation with minimal environmental impact. Among several geometric optimization strategies aimed at improving turbine performance, the application of sweep angles to turbine blades, widely studied in wind energy systems, remains underexplored in hydrokinetic contexts. This study investigates the aerodynamic performance of hydrokinetic turbines equipped with swept blades, including both forward and backward configurations, through Computational Fluid Dynamics (CFD) simulations. A baseline model with straight blades and variations with sweep angles of 10°, 20°, and 30° were analyzed using a modified Blade Element Momentum (BEM) theory combined with radial coordinate transformation, enabling a consistent and low-cost computational approach. The simulations were performed under identical operating conditions, employing the $k - \omega$SST turbulence model to assess both energy efficiency and aerodynamic behavior.

The results indicate a reduction of approximately 7% to 9% in the maximum power coefficient C_P for turbines with a 30° sweep, in both backward and forward orientations, when compared to the baseline model. Despite this decrease in C_P, complementary analyses revealed important insights into aerodynamic performance. In particular, the backward-swept blades exhibited more favorable wake characteristics, with improved boundary layer behavior, delayed flow separation and reduced turbulence intensity. Moreover, the recovery length for pressure and velocity downstream of the rotor was also more favorable in the backward-swept configuration. These findings highlight a trade-off between efficiency and flow control that may guide future design strategies.

This research addresses a relevant gap in the literature, characterized by the scarcity of studies focused on hydrokinetic turbines with swept blades and the lack of standardization in swept-blade analysis methodologies. By proposing a consistent and replicable numerical framework, the present work contributes a valuable tool for the geometric optimization of hydrokinetic turbine blades using sweep angles, combining physical fidelity with computational efficiency.

Keywords: Hydrokinetic turbines. Swept blades. CFD. BEM theory. Aerodynamic optimization.

Resumo

Turbinas hidrocinéticas representam uma tecnologia promissora em energias renováveis, com impacto ambiental reduzido. Dentre as diversas estratégias de otimização voltadas para o aumento de performance de turbinas, a aplicação de ângulos de curvatura às pás das turbinas, amplamente estudadas para turbinas eólicas, permanece pouco explorada em contextos de energia hidrocinética. O presente estudo investiga a performance aerodinâmica de turbinas hidrocinéticas equipadas com pás curvadas, incluindo configurações de curvatura para frente e para trás, por meio de simulações de dinâmica de fluidos computacional (CFD). Um modelo de turbina de referência com pás convencionais e variações de ângulos de curvatura de 10°, 20° e 30° foram analisados utilizando uma modificação da teoria Blade Element Momentum combinada com uma transformação de coordenada radial, possibilitando uma abordagem consistente e de baixo custo computacional. As simulações foram conduzidas sob condições operacionais idênticas, utilizando o modelo de turbulência k–ω SST para avaliar tanto a eficiência energética quanto o comportamento aerodinâmico.

Os resultados indicam uma redução de aproximadamente 7% a 9% no coeficiente de potência máximo C_P para turbinas com ângulo de curvatura de 30°, tanto na configuração para trás quanto para frente, em comparação com o modelo de referência. Apesar dessa diminuição no C_P, análises complementares revelaram importantes evidências sobre o desempenho aerodinâmico. Em particular, as pás curvadas para trás apresentaram comportamento mais favorável da região da esteira, com descolamento retardado do escoamento e menor intensidade de turbulência. Além disso, o comprimento de recuperação de pressão e velocidade a jusante do rotor também se mostrou mais favorável para a configuração curvada para trás. Esses achados evidenciam um equilíbrio entre eficiência e controle do escoamento, que pode orientar futuras estratégias de projeto.

Esta pesquisa aborda lacunas relevantes na literatura, caracterizada pela escassez de estudos voltados para turbinas hidrocinéticas com pás curvadas e pela ausência de padronização nas metodologias de avaliação dessas geometrias. Ao propor uma estrutura metodológica numérica consistente e replicável, o presente trabalho contribui com uma ferramenta de otimização geométrica para pás de turbinas hidrocinéticas baseadas em curvatura das pás, combinando fidelidade física e eficiência computacional.

Palavras-chave: Turbinas hidrocinéticas. pás curvadas. CFD. Teoria BEM. Otimização aerodinâmica.

List of figures

List of tables

List of abbreviations and acronyms

ANEEL	Brazilian Electricity Regulatory Agency
BEM	Blade Element Momentum
BHATT	Bidirectional Horizontal-axis Tidal Turbine
CAD	Computer-aided Design
CFD	Computational Fluid Dynamics
HPP	Hydroelectric Power Plant
IEA	International Energy Agency
IPCC	Intergovernmental Panel on Climate Change
MHP	Micro Hydropower
MRF	Multiple Reference Frame
PAT	Pump-as-turbine
RANS	Reynolds-averaged Navier-Stokes
RMS	Root Mean Square
SHP	Small Hydropower
SST	Shear Stress Transport
TCT	Tidal Current Turbine
TKE	Turbulent Kinetic Energy
UNFCCC	United Nations Framework Convention on Climate Change
WHO	World Health Organization
WRI	World Resources Institute

Contents

1 Introduction

1.1 Motivation

The global energy demand has risen substantially by 2024, driven by population growth and industrial development. Societal and environmental challenges press the growing urgency to shift towards renewable energy sources to address climate change issues, resource scarcity and the need for more sustainable growth models. The traditional reliance on fossil fuels has led to extensive environmental degradation and greenhouse gas emissions, directly contributing to climate change and its associated impacts, such as extreme weather conditions, biodiversity loss and sea-level rise.

The Intergovernmental Panel on Climate Change (IPCC) indicates that the adverse impacts of human-caused climate change will intensify, causing extreme weather conditions to become more widespread and pronounced with every increment of warming. Therefore, the urgency to mitigate climate change impacts remains a driving force for expanding renewable energy investments. Cutting emissions quickly and sharply to reduce global greenhouse gases by nearly half by 2030 is required to prevent the worst impacts of climate change (Calvin *et al.*, 2023).

Regarding climate change mitigation, the Paris Agreement sets the following long-term goals for all parties legally bound to the treaty, according to the United Nations Framework Convention on Climate Change (UNFCCC):

- Substantially reduce global greenhouse gas emissions to hold global temperature increase to well below $2°C$ above pre-industrial levels and pursue efforts to limit it to $1.5°C$ above pre-industrial levels, recognizing that this would significantly reduce the risks and impacts of climate change;
- Periodically assess the collective progress towards achieving the purpose of this agreement and its long-term goals;
- Provide financing to developing countries to mitigate climate change, strengthen resilience and enhance abilities to adapt to climate impacts.

Renewable energy sources like hydrokinetic, solar, and wind are crucial in curbing greenhouse gas emissions and reducing the ecological footprint of energy production. According to the World Resources Institute (WRI), the energy sector accounts for nearly 72% of global greenhouse gas emissions, a major driver of climate change (WRI, 2023). By investing in renewable sources, societies can make strides toward achieving the Paris Agreement's targets.

Global reliance on fossil fuels has exposed nations to volatile markets, economic instability, and supply chain disruptions. Being locally sourced, renewable energy offers a more resilient energy model, enhancing energy security, especially in developing regions. In addition, renewable energy diversification reduces reliance on imported fuels, enhancing national energy security. This transition reduces susceptibility to supply disruptions, particularly for nations vulnerable to energy market fluctuations. Hydrokinetic turbines, wind, and solar installations can be decentralized, decreasing vulnerability to single-point failures in traditional power grids and fostering a more resilient energy infrastructure (IRENA, 2023).

Moreover, according to the World Health Organization (WHO), energy is linked to many sustainable development priorities, including public health, gender equality, food security, clean water, education and economic growth. In urban areas, air pollution has been linked to respiratory illnesses, cardiovascular diseases, and other health issues. Renewable energy adoption is associated with improved public health outcomes by reducing air and water pollution, common byproducts of fossil fuel combustion (HEPA, 2024).

Although global efforts to pursue cleaner and renewable energy sources have increased, the world remains highly dependent on carbon-based forms of energy. According to the International Energy Agency (IEA), fossil fuels (*i.e.*, coal, natural gas, and oil) continue to comprise the majority of the world's total energy supply. This dependence has grown from 1990 to 2022, as illustrated in figure 1.1.

Figure 1.1 – World's total energy supply by source

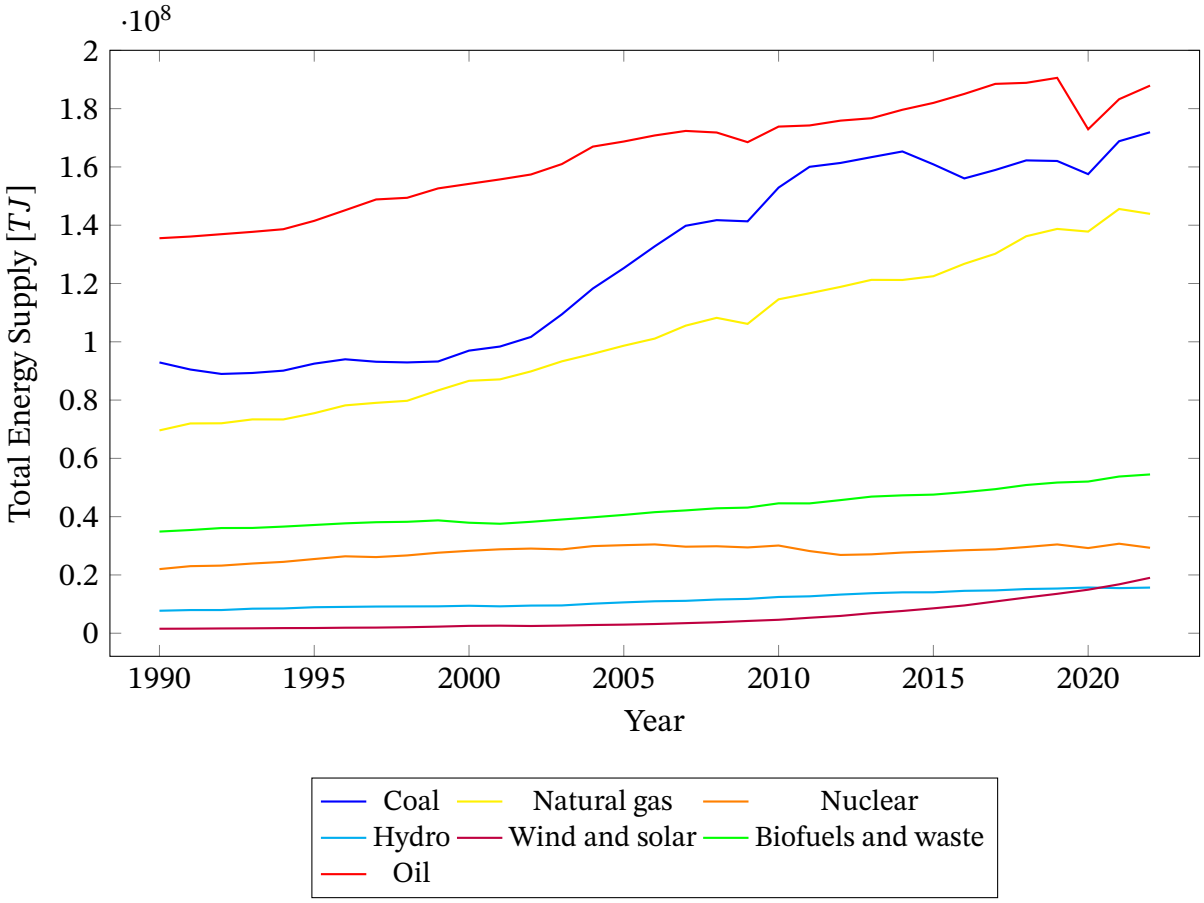

Source: IEA (2024)

Coal remains the most widely utilized energy source for electricity generation globally, followed by natural gas and hydropower, despite the increasing development of renewable energy technologies. Figure 1.2 illustrates the distribution of electricity generation by source, as reported by IEA (2024).

Figure 1.2 – World's electricity generation by source

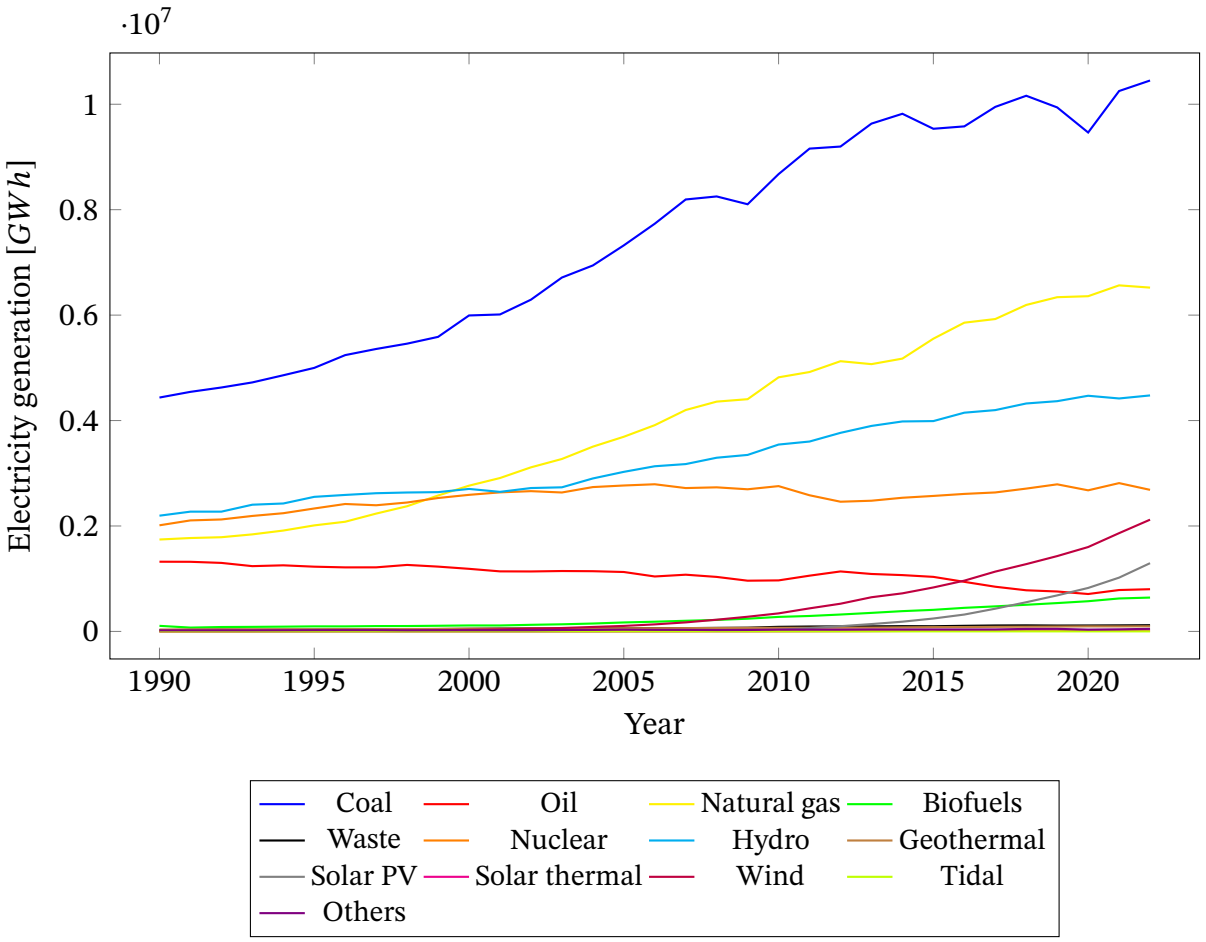

Source: IEA (2024)

Wind and solar energy have shown exponential growth among low-carbon and renewable electricity sources worldwide, according to IEA (2024). Nevertheless, hydropower continues to account for the largest share of electricity generated from clean sources, as illustrated in figure 1.3 and figure 1.4. This suggests that hydropower will continue to play a significant role in the global energy matrix for the foreseeable future.

Figure 1.3 – Low-carbon electricity generation by source

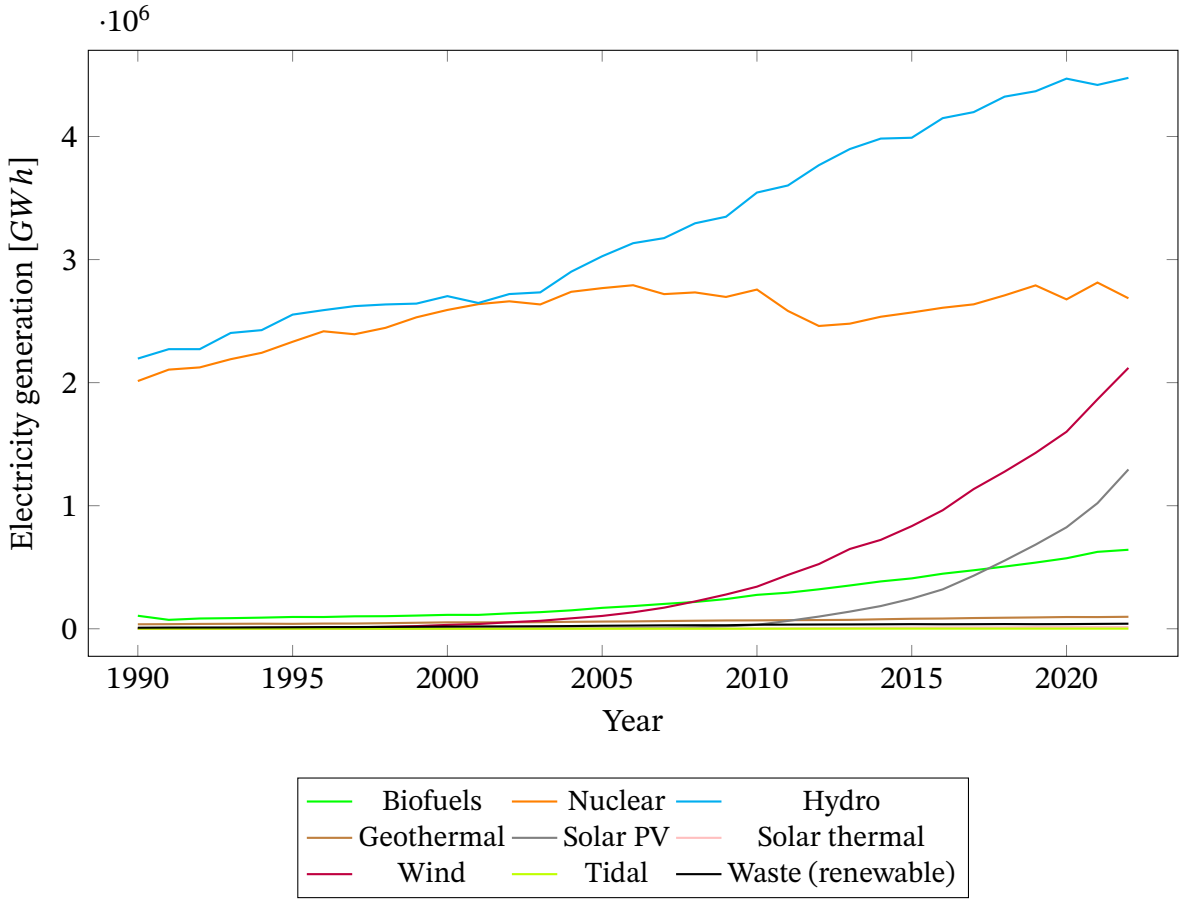

Source: IEA (2024).

Figure 1.4 – Renewable electricity generation by source (non-combustible)

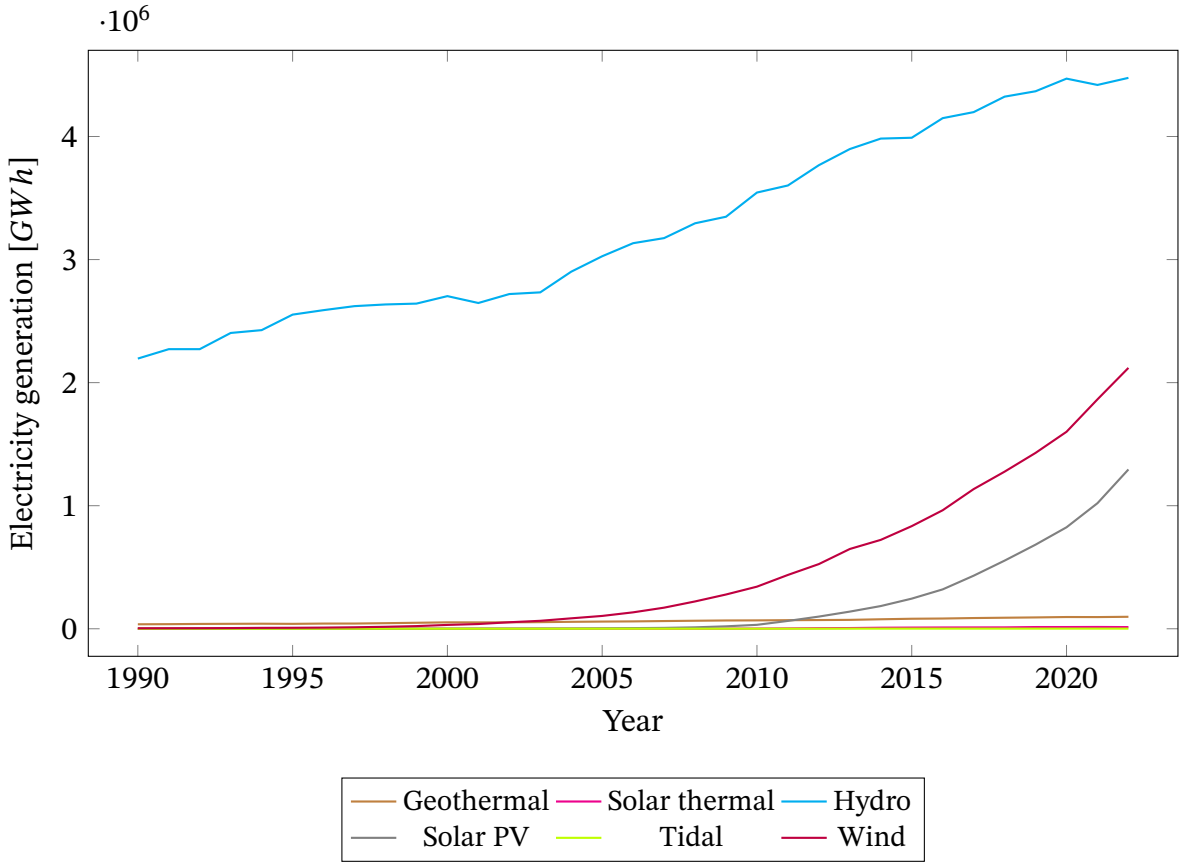

Source: IEA (2024).

Hydrokinetic technology, which generates power from river and ocean currents, exemplifies an alternative for the shift toward energy resilience. This form of energy is particularly valuable in water-abundant regions like Brazil, where rivers can provide a stable, predictable energy flow, reducing dependency on imports and fossil fuels. Brazil has one of the most renewable energy-focused portfolios globally, ranking third in renewable energy capacity and electricity generation, as reported by IRENA (2023). The country's total energy supply is primarily sourced from oil, followed by biofuels and hydropower, respectively. In terms of electricity capacity and generation, hydropower is the predominant contributor, producing 425,966 GWh in 2023, according to IEA (2024). The figures below (see figure 1.5 and figure 1.6) represent the Brazilian total energy supply and electricity generation by source.

Figure 1.5 – Brazilian total energy supply by source

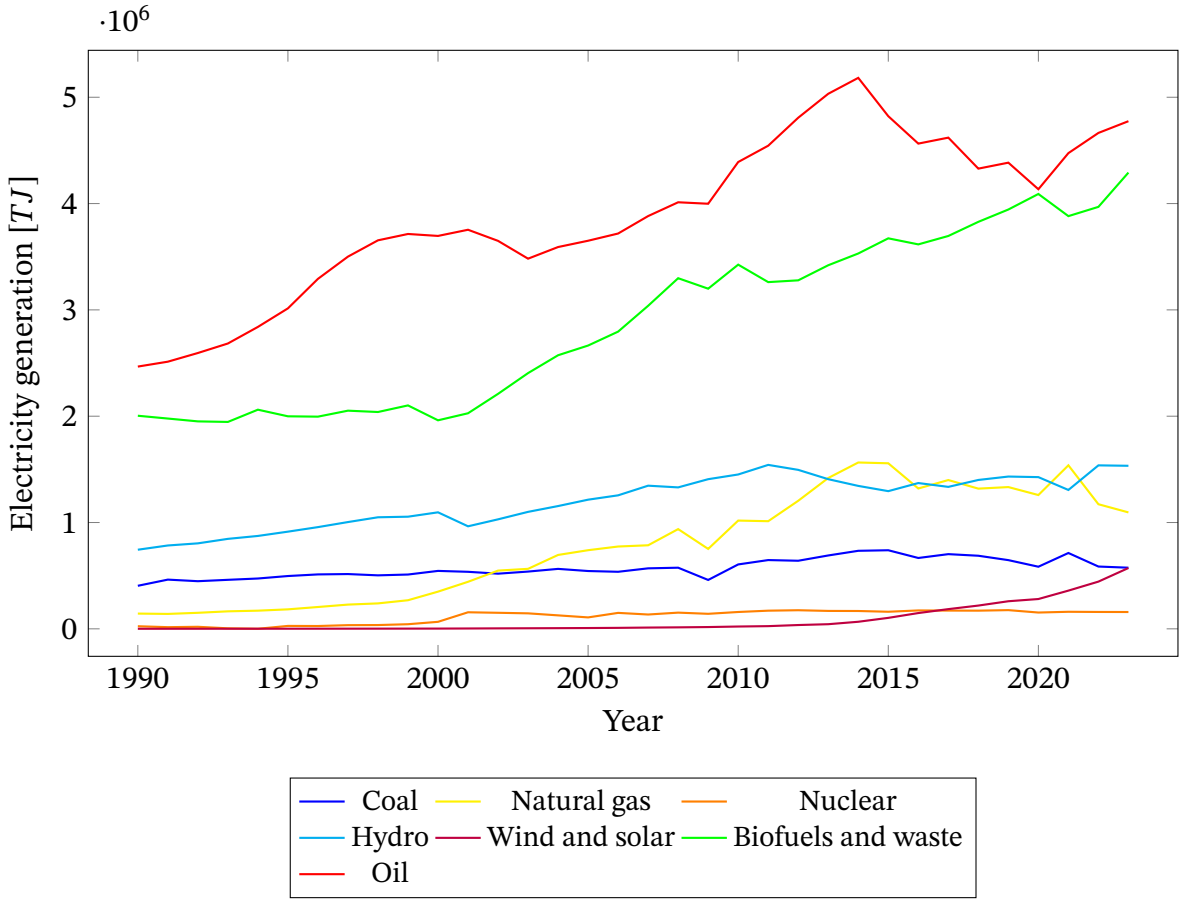

Source: IEA (2024).

Figure 1.6 – Brazilian electricity generation by source

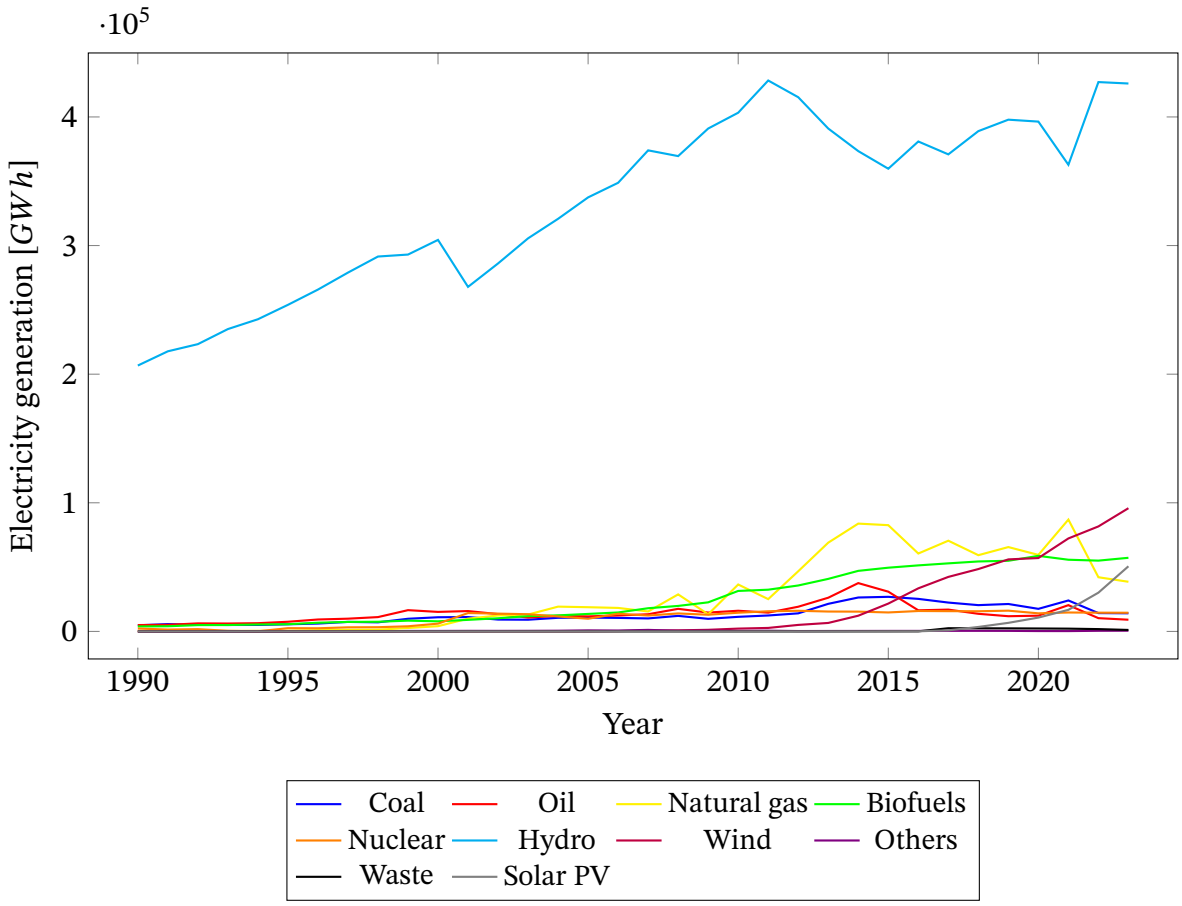

Source: IEA (2024).

The renewable energy sector has become one of the fastest-growing sectors for job creation and economic stimulation. In Brazil, renewables accounted for approximately 46% of the national energy mix in 2023, with hydropower as a primary source, according to the Brazilian Ministry of Mines and Energy. The report by MME-EPE (2022) indicates that, in 2021, hydropower contributed approximately 62% to the national installed capacity, including Hydroelectric Power Plants (HPPs), Small Hydropower (SHP) plants, and Micro Hydropower (MHP) plants. Hydropower expansion is occurring across all regions of Brazil and is projected to add approximately 7.9 GW over the ten-year horizon, according to the same report. Figure 1.7 illustrates the Brazilian installed capacity, evaluated in 2021.

Figure 1.7 – Installed capacity - Brazil, 2021

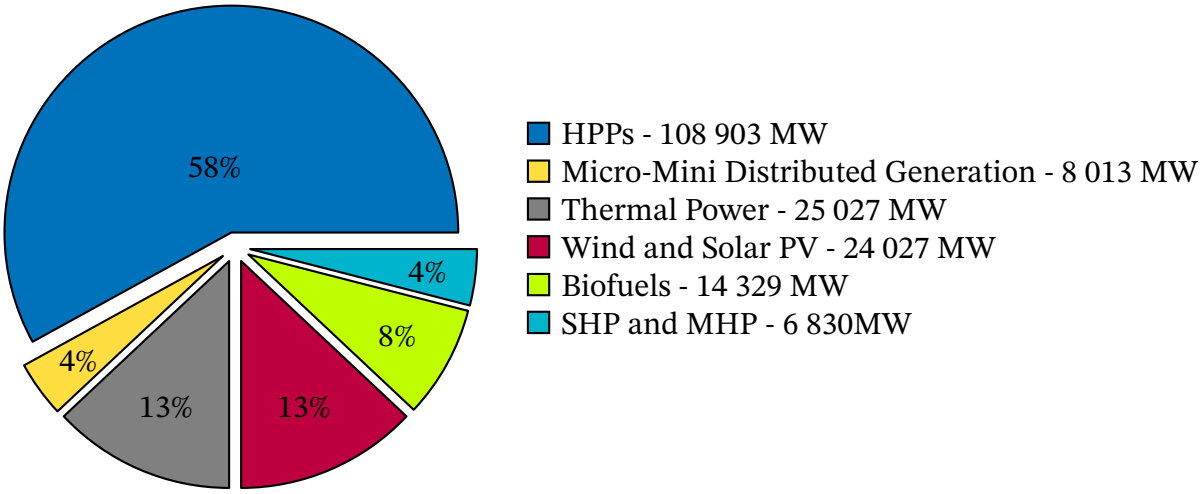

Source: MME-EPE (2022)

The Brazilian Energy Development Plan also considers the potential and benefits of expanding small-scale hydropower generation, particularly SHPs and MHPs, for which a large number of untapped projects exist. These systems provide several advantages to the Brazilian electricity matrix, including synergies with other renewable sources (*e.g.*, wind, biomass, and solar), as well as enhanced operational and storage flexibility in the short-term operational horizon. Such advantages are expected to become increasingly evident with the implementation of hourly pricing and the anticipated development of capacity remuneration mechanisms (MME-EPE, 2022). Accordingly, the Investment Decision Model includes SHP and MHP projects as candidates for expansion, starting from 2024.

In particular, SHPs can take advantage of reservoirs originally designed for other purposes, such as water supply, to also generate electricity. This presents opportunities for integrated resource optimization. Similarly, repowering and modernization of existing HPPs provide a viable path to expand Brazil's hydropower capacity while enhancing the efficiency of water use for electricity generation. These strategies improve the reliability and operational performance of existing infrastructure while avoiding the environmental and social impacts associated with the construction of new projects.

International Hydropower Association (2024) also highlights the growing relevance of innovative small-scale hydropower technologies, especially in mini-grids and rural areas, including hydrokinetic systems. In Brazil, the future of SHPs is likely to follow international trends, prioritizing modular modernization and reduced environmental impact. Niebuhr *et al.* (2019) further notes that the hydrokinetic industry has moved beyond its demonstration phase, with full-scale projects already under construction and operational globally.

Regarding existing HPPs, previous editions of the Ministry's report identified signif-

icant opportunities for energy and capacity gains in the National Interconnected System through repowering and modernization of existing infrastructure. Given the scale, importance, and age of Brazil's current hydropower complex, a technical potential of 50 GW has been estimated for modernization and repowering of existing facilities (MME-EPE, 2022).

In addition, mechanisms to promote the hybridization of existing plants (*e.g.*, installation of photovoltaic systems on hydropower reservoirs or wind farm sites) can optimize the use of shared electrical infrastructure, minimize the need for new construction, and reduce environmental impacts. While current regulations within the National Interconnected System already permit land-sharing and operational synergies, ANEEL (Brazilian Electricity Regulatory Agency) has recently approved specific regulatory frameworks for hybrid and associated power plants (MME-EPE, 2022).

According to Els *et al.* (2018), hydrokinetic technology is being studied to be used in larger hydropower plants, aiming at the conversion of kinetic energy present in large rivers, tidal flows and ocean streams for on-grid distributed generation and its integration in the electricity sector. This aligns with the modernization and expansion goals for the existing hydroelectric complex in Brazil, outlined by MME-EPE (2022).

The information presented suggests that hydropower will continue to play a central role in Brazil's long-term energy strategy. Significant investments have already been made in enhancing existing facilities (HPPs, SHPs, and MHPs) to improve energy extraction. Advances in turbine design, including innovations in hydrokinetic turbine blade optimization, are further improving the efficiency and operational performance of renewable systems. For example, optimizing blade geometry and orientation in both wind and hydrokinetic turbines can enhance energy yield and reliability. These innovations also help expand the applicability of renewable energy systems to a wider range of geographic and environmental contexts, facilitating broader adoption.

Brazil's electric power system has seen a rapid expansion of variable renewables, especially wind and solar (Empresa de Pesquisa Energética (EPE), 2025). Although this strengthens the low-carbon profile of the National Interconnected System, it also intensifies operational challenges such as curtailment (renewable output reduction due to network or system constraints) and steep ramp events during sunrise, sunset, or cloud passages, which increasingly demand complex dispatch strategies from the system operator Operador Nacional do Sistema Elétrico (2025).

In this context, river hydrokinetic turbines emerge as a complementary resource with a temporal behavior distinct from wind and solar. By extracting kinetic energy directly from free-flowing rivers, without dams, these systems benefit from hydrological regimes that vary seasonally rather than daily. As a result, their power output is smoother and more predictable, allowing generation to continue during PV ramp-down periods and nighttime. This localized, low-intermittency production can support riverside communities and small

load centers, easing transmission constraints and mitigating local curtailment.

Beyond their environmental appeal, hydrokinetic technologies may contribute to system stability under high levels of wind and solar penetration by providing decentralized generation precisely during periods when photovoltaic becomes unavailable.

Nevertheless, key challenges remain. As noted by Niebuhr *et al.* (2019), reducing system costs, optimizing turbine arrays, and balancing energy extraction with environmental preservation are essential tasks for hydrokinetic systems to achieve large-scale commercial viability.

1.2 State of the art

The energy conversion in turbomachinery is based on extracting the kinetic energy from fluid motion to generate mechanical power at the rotor shaft, which is subsequently converted into electrical energy. The maximum recoverable energy from the flow depends on how effectively the fluid velocity is managed across the turbine rotor. For wind energy applications, according to Hansen (2008), the theoretical maximum power available occurs when the flow velocity is reduced to zero behind the rotor, as defined by:

$$P = \frac{1}{2}\dot{m}U_0^2 = \frac{1}{2}\rho A U_0^3, \tag{1.1}$$

where ρ is the fluid density, A is the rotor swept area, and U_0 is the undisturbed inlet velocity. For horizontal-axis turbines, $A = \pi R^2$.

In practice, the Betz limit demonstrates that this ideal condition is physically unfeasible, establishing a theoretical efficiency limit through the power coefficient C_P, whose maximum is given by:

$$C_P = \frac{16}{27} \approx 0.593. \tag{1.2}$$

As noted by Hansen (2008), extracting all kinetic energy would require the downstream velocity to be null, which would prevent flow continuity through the rotor, and that is physically impossible. Modern turbines operate near this limit, typically achieving C_P values up to 0.5.

To assess aerodynamic performance, the Blade Element Momentum (BEM) theory is widely adopted. This method couples global momentum conservation with local blade element analysis, discretizing the blade span into radial sections and evaluating aerodynamic loads on each segment (Hansen, 2008). BEM remains a standard approach due to its computational efficiency and its capacity to produce accurate results for steady-state regimes.

In this framework, the blade is divided into elements, and the loads are assumed to vary linearly between adjacent radial positions r_i and r_{i+1}, as illustrated in figure 1.8.

Figure 1.8 – Assumption of linear load variation between radial positions r_i and r_{i+1}

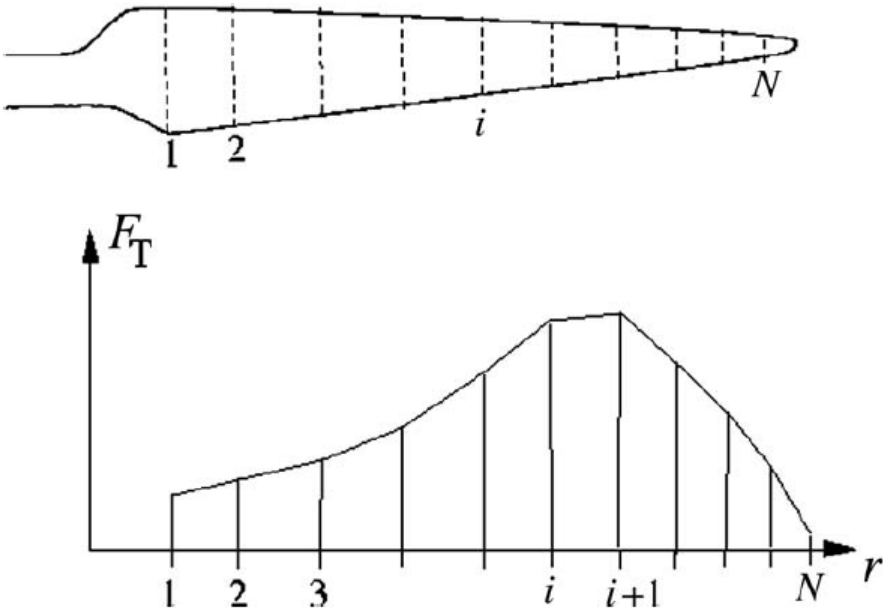

Source: (Hansen, 2008).

The power coefficient C_P is defined as the ratio between the actual extracted power and the total available power:

$$C_P = \frac{P}{\frac{1}{2}\rho A U^3} \tag{1.3}$$

This coefficient strongly depends on the tip-speed ratio λ, expressed as:

$$\lambda = \frac{\omega R}{U} \tag{1.4}$$

where ω is the rotor angular velocity.

The tip-speed ratio influences the induced flow field and the aerodynamic load distribution along the blade. Therefore, plotting C_P as a function of λ provides valuable insight into turbine performance relative to the Betz limit.

For the analysis of complex flow phenomena, especially in non-conventional geometries, Computational Fluid Dynamics (CFD) is a powerful numerical tool. CFD enables the solution of the Navier–Stokes equations in three-dimensional domains, allowing for the evaluation of local flow variables such as velocity, pressure, turbulence, and boundary layer

characteristics, parameters that are difficult to obtain through experiments or analytical models.

According to White *et al.* (2011), commercial CFD platforms have expanded the ability of engineers to simulate viscous flow in complex geometries, provided that the mesh and boundary conditions are well defined. Cengel and Cimbala (2013) further states that, despite inherent limitations in turbulence modeling, CFD yields sufficiently accurate results for many engineering problems when validated against experimental data.

The selection of an appropriate turbulence model is an important factor in the reliability of CFD simulations, as its influence must be understood in conjunction with other modeling considerations, particularly the boundary conditions and the numerical formulation adopted. As highlighted by Silveira-Neto (2020), mesh refinement alone does not guarantee accurate results, since the predictive capability of a turbulent flow simulation depends on the interaction between grid resolution, physical modeling, and boundary conditions.

Among the classical two-equation closures, the k–ε model has shown robust performance for free-stream and fully developed turbulent flows, although its applicability may be limited in regions strongly affected by near-wall behavior or adverse pressure gradients. The k–ω formulation, in contrast, generally offers improved near-wall predictions and better sensitivity to boundary layer development, particularly in flows involving separation or strong gradients (Wilcox *et al.*, 1998). Nonetheless, both models have advantages and limitations depending on the flow configuration, and their suitability must be evaluated on a case-by-case basis.

Aiming to combine the strengths of both models, Menter introduced the k-ω Shear Stress Transport (SST) model, which blends k-ω near the wall with k-ε in the free stream. According to Wilcox *et al.* (1998), the SST formulation enhances stability and accuracy in simulations with flow separation, making it well suited for turbomachinery and aerodynamic studies.

In the pursuit of enhanced turbine efficiency, both active and passive optimization strategies have been developed. Active methods, such as pitch control, introduce complexity and energy demands. Passive methods, including diffusers and blade geometry modifications, offer performance gains without additional energy input. Among passive techniques, blade sweep (a curvature applied to the blade span) has gained attention for its potential to improve energy capture while mitigating loads.

According to Larwood, Dam, and Schow (2014), blade sweep modifies pressure and mass distribution, promoting torsional flexibility at the blade tip and passively reducing aerodynamic loads in turbulent flows. The geometry of the sweep proposed by the authors is defined by:

$$y = d_{\text{tip}} \left(\frac{x - x_{\text{start}}}{L_{\text{blade}} - x_{\text{start}}} \right)^{\gamma} \tag{1.5}$$

where y is the local deflection from the pitch axis, d_{tip} is the tip displacement, x is the radial coordinate, x_{start} is the starting point of the sweep, L_{blade} is the blade length, and γ is the sweep exponent. Figure 1.9 depicts the blade sweep parameters.

Figure 1.9 – Swept blade parameters

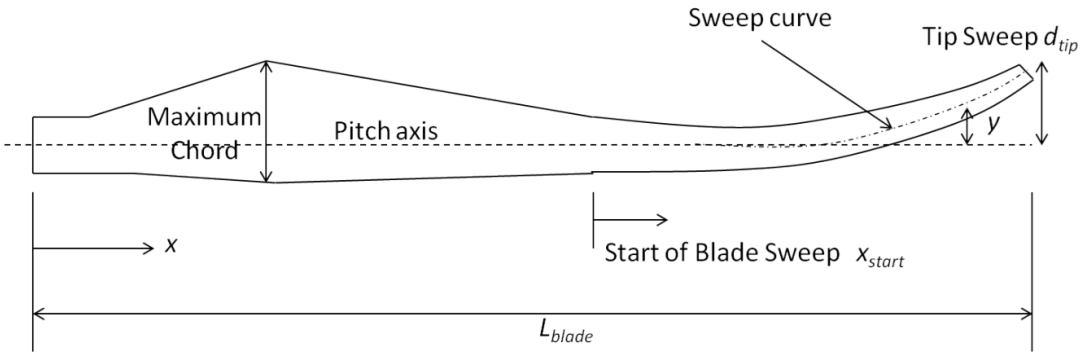

Source: (Larwood; Dam; Schow, 2014).

This approach, coupled with an aeroelastic analysis using the CurveFAST code (derived from NREL FAST), was validated against experimental data and other software tools, such as Adams^{TM}. The simulations included wind loads generated according to the IEC 61400-1 Class II standard, with statistical analysis based on the Rayleigh distribution to estimate annual energy production. According to Larwood, Dam, and Schow (2014), among the parameters analyzed, such as tip sweep, torsional stiffness, and sweep curvature exponent, the tip sweep magnitude had the greatest influence on energy production, resulting in a 6% increase in annual output and a concurrent reduction in structural loads when compared to straight-bladed configurations. However, in large-scale turbines (above $5MW$), torsional instabilities were observed at speeds exceeding the nominal operating point, indicating that the implementation of sweep angles must account for these structural limitations.

Although Larwood, Dam, and Schow (2014) note that blade sweep can increase the rotor diameter while maintaining structural loads within acceptable limits, in their analysis, the larger swept area results from a load-alleviation mechanism enabled by sweep, not from an intentional attempt to enhance power extraction. In the present work, the rotor diameter is intentionally kept fixed to avoid improvements from increased swept area. The central question is whether sweep alone can alter load distribution and improve power extraction. Thus, swept blades are examined as a passive strategy to relieve loads and potentially enhance performance without changing rotor size.

Moreover, Kaya *et al.* (2018) stated that geometric optimization of turbine blades has become an effective strategy to enhance aerodynamic efficiency and reduce structural loads.

In their study, a parametric investigation was conducted to assess the impact of sweep angles on blade performance, considering both forward and backward configurations (aligned with or opposite to the direction of rotor rotation, respectively) in horizontal-axis wind turbines. Using a scaled turbine model with a diameter of $0.9m$ (NTNU turbine), the effects of the sweep initiation point and tip displacement were analyzed in relation to the power coefficient (C_P) and thrust coefficient (C_T).

The authors proposed a mathematical formulation to define the blade deflection along the radial direction, allowing independent adjustment of both the sweep start location and tip offset. The expression is given by:

$$z_{\text{offset}} = \frac{(r_r - r_{ss})(R - P_s)}{(R - r_{ss})} \cdot M \left(\frac{(1 - P_r)(1 - P_{rss})}{P_r} \right) \tag{1.6}$$

where z_{offset} denotes the local displacement relative to the pitch line, r_r is the local radius, r_{ss} is the sweep starting point, R is the total blade radius, $P_s = d/R$ represents the tip displacement ratio, M is the sweep mode (controlling curvature intensity), and $P_r = r_r/R$, $P_{rss} = r_{ss}/R$ are normalized radial positions.

A total of 32 blade configurations (16 forward-swept and 16 backward-swept) were evaluated using the CFD software Ansys Fluent. The mesh consisted of 4.8 million elements, and the simulations employed the Realizable k–ε turbulence model under a $10m/s$ wind flow and a tip-speed ratio of $\lambda = 6$. The mesh was refined to ensure $y^+ \approx 1$ near the blade surfaces, enabling accurate capture of wall-bounded flow effects. The forward-swept blades showed a 2.9% increase in C_P, while the backward-swept blades achieved up to a 5.4% reduction in C_T.

A numerical approach was proposed by Zuo *et al.* (2016) to optimize the blade stacking line of swept blades, defined as the trajectory of airfoil centroids from root to tip, using biomimetic principles inspired by bird wings. The objective was to evaluate the aerodynamic performance of the models at high tip-speed ratios ($\lambda > 7$), a regime in which conventional straight-bladed turbines using the LN221 airfoil tend to exhibit reduced performance. The proposed configuration is illustrated in figure 1.10.

Figure 1.10 – Sketch map of the swept blade

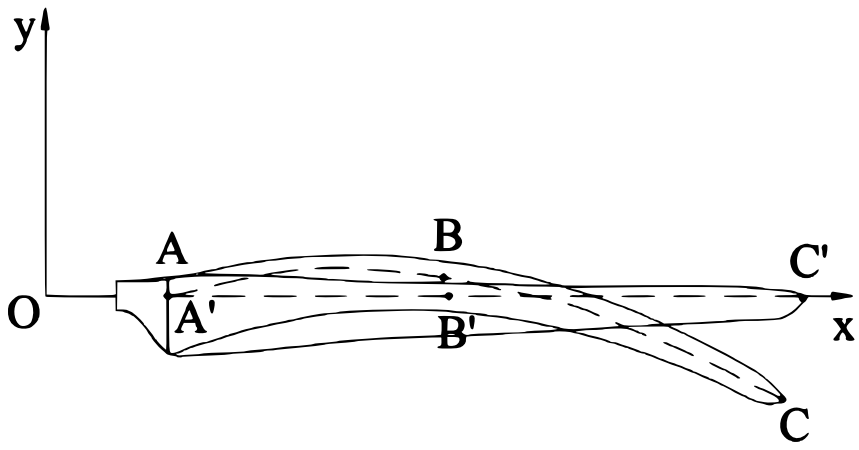

Source: (Zuo *et al.*, 2016).

Based on this configuration, the blade curvature is defined through Lagrangian polynomial interpolation of points $A(x_A, y_A)$, $B(x_B, y_B)$, and $C(x_C, y_C)$, resulting in the stacking line equation:

$$y = \frac{(x - x_C)(x - x_C)}{(x_B - x_A)(x_B - x_C)} \cdot y_B + \frac{(x - x_A)(x - x_B)}{(x_C - x_A)(x_C - x_B)} \cdot y_C \tag{1.7}$$

To maintain the same swept area as the straight blade, the coordinates of point C must satisfy the condition $x_C^2 + y_C^2 = R^2$.

An unstructured mesh with 2.81 million elements was generated using ICEM CFD, ensuring adequate spatial resolution. The CFD simulations were carried out in Ansys Fluent, employing the k–ω SST turbulence model. The computational domain was divided into stationary and rotating zones, as depicted in figure 1.11.

Figure 1.11 – Computational domain and mesh

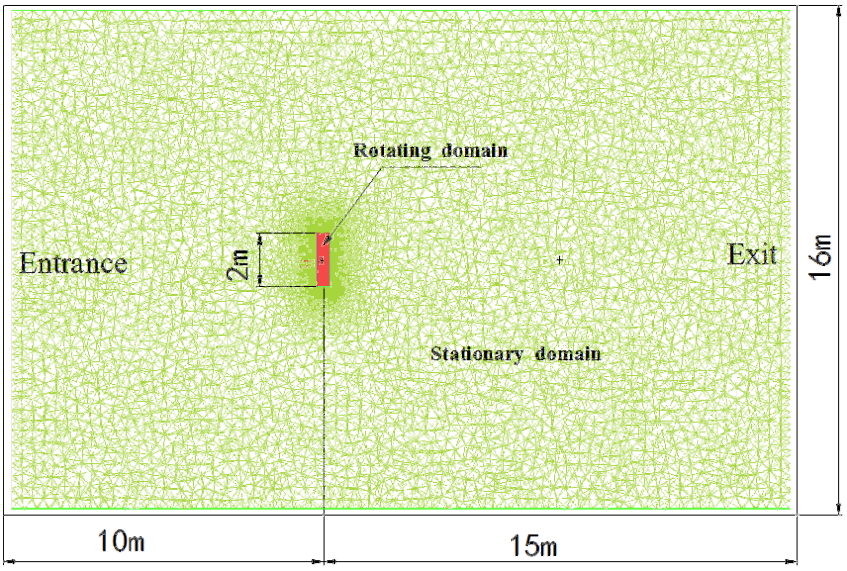

Source: (Zuo *et al.*, 2016).

The results demonstrated that the swept blade achieved a power coefficient (C_P) 3.2% higher than that of the straight blade at a tip-speed ratio of $\lambda = 9.82$ (Zuo *et al.*, 2016). Furthermore, the swept blade experienced significantly lower thrust forces, particularly at higher wind speeds, underscoring the aerodynamic advantages of the swept blade configuration.

In addition to applications in wind turbines, Liu *et al.* (2022) conducted a systematic investigation into the impact of swept blades on bidirectional horizontal-axis tidal turbines (BHATTs), which operate under both ebb and flood tide conditions. The study aimed to evaluate how various sweep configurations (forward, backward, upstream, and downstream) affect the hydrodynamic performance of the turbines, particularly in terms of the power coefficient (C_P) and thrust coefficient (C_T). The sweep configurations analyzed are illustrated in figure 1.12.

Figure 1.12 – Sketch of four directions of the swept blade, with the cyan arrow being te direction of the incoming flow

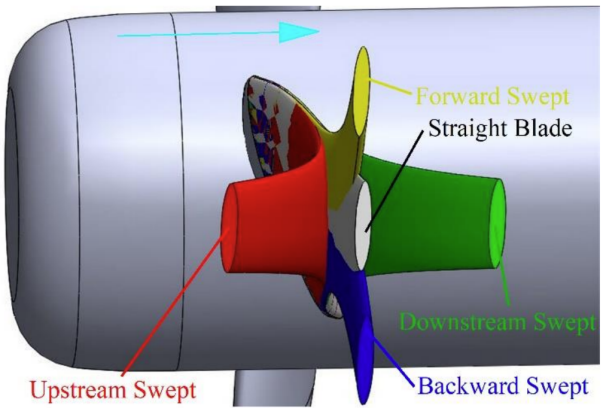

Source: (Liu *et al.*, 2022).

The blade curvature was defined using the following piecewise function:

$$dl = \begin{cases} d_{\text{tip}} \left(\dfrac{r - r_{ss}}{R - r_{ss}} \right)^{z}, & \text{if } r \geq r_{ss} \\ 0, & r < r_{ss} \end{cases} \tag{1.8}$$

where dl is the distance between the center of the blade section and the pitch line, d_{tip} is the tip displacement, r is the local radius, r_{ss} is the sweep initiation point, R is the total blade radius, and z is an exponent controlling the curvature smoothness.

The numerical simulations were carried out in OpenFOAM using the interDyMFoam solver and the k–ω SST turbulence model. The computational domain comprised a stationary region and a rotating region containing the rotor, coupled via the sliding mesh technique. The inlet flow velocity was set to $2.4 m/s$.

According to Liu *et al.* (2022), downstream-swept blades resulted in a 3.2% increase in output power and a 3.7% growth in thrust. Detailed flow analysis revealed significant changes in radial and axial velocity distributions around the blades and within the wake, including alterations in streamlines near the suction side and the formation of tip vortices. These performance variations in BHATTs were attributed to the complex flow field modifications induced by blade sweep.

The study by Zheng *et al.* (2024) investigated the influence of blade sweep on the energy efficiency and hydrodynamic reliability of tidal turbines through CFD simulations and experimental analysis. The geometric parameters assessed included the sweep length (L) and sweep angle (β), focusing on their effects on the power coefficient (C_P) and the cavitation number (σ). The numerical model was developed in Ansys Fluent using an unstructured mesh with 8.5 million elements (after mesh convergence), employing a Multiple Reference

Frame (MRF) approach and the RNG k–ε turbulence model. The computational domain and boundary conditions are illustrated in figure 1.13.

Figure 1.13 – Computational domain and boundary conditions of the numerical model

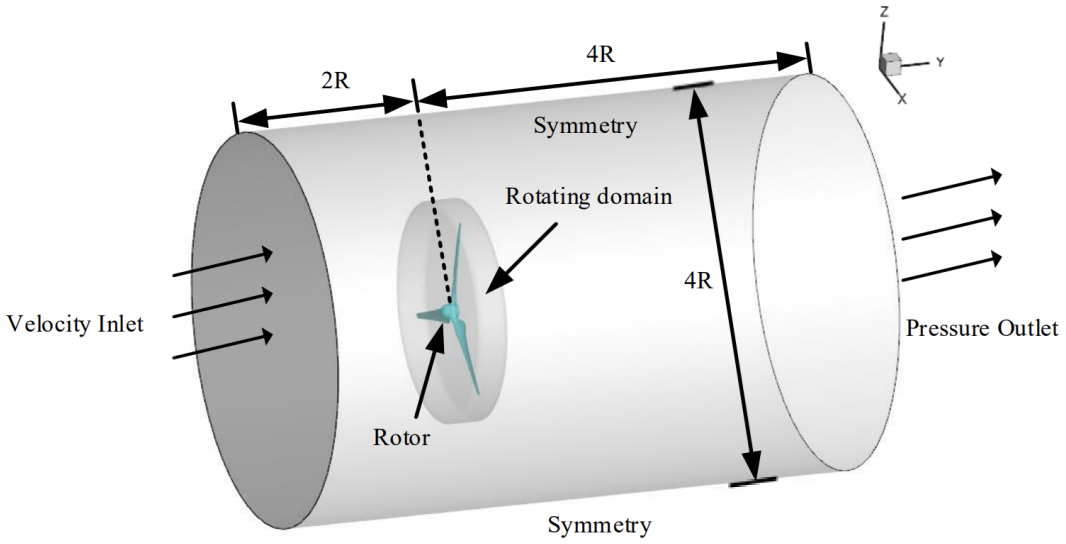

Source: (Zheng *et al.*, 2024).

The key findings reported by Zheng *et al.* (2024) are summarized as follows:

- The power coefficient (C_P) of the swept-blade tidal current turbine (TCT) increased by 5–17%, depending on the tip-speed ratio (TSR).
- The swept-blade design demonstrated enhanced cavitation resistance compared to the straight-blade configuration, particularly under harsh marine conditions.
- The maximum power coefficient ($C_P = 0.41654$) was achieved with a sweep length of $0.544m$ and a sweep angle of 28.88°.

Wang *et al.* (2023) investigated the hydrodynamic performance of a pump-as-turbine (PAT), a widely adopted device in micro-hydropower systems and energy recovery applications, through CFD simulations validated against experimental data.

The hydrodynamic performance of a pump-as-turbine (PAT), a widely adopted device in micro-hydropower systems and energy recovery applications, was investigated by Wang *et al.* (2023) through CFD simulations validated against experimental data. Various sweep angles were evaluated with respect to energy efficiency, load reduction, pressure distribution, and entropy generation under different flow regimes. A structured mesh comprising 1.2 million hexahedral elements was employed. The simulations adopted the k–ε turbulence model and a Transient Rotor–Stator approach with a time step of $3.33 \times 10^{-4}s$, simulating ten complete revolutions of the rotor.

The results demonstrated a 0.58% increase in C_P with an 8° backward-sweep angle. Additionally, the backward-swept blade configuration led to reductions in turbulent kinetic energy and entropy generation at the outlet, as well as smaller vortex structures and lower overall flow unsteadiness. The backward-swept geometry was shown to reduce hydraulic losses, improve flow uniformity, and extend the high-efficiency operating range of the PAT (Wang *et al.*, 2023).

An optimization strategy for wind turbine blade geometry, using artificial neural networks under synthetically generated turbulent flow, was proposed by Sessarego *et al.* (2020). The objective was to accurately capture both aerodynamic and structural effects of curved geometries. A Latin Hypercube Sampling method was employed to explore various combinations of sweep and pre-bend configurations, aiming to maximize the power coefficient C_P and minimize the thrust coefficient C_T.

The blade geometry was defined by the following expression:

$$y = d_{tip}\left(\frac{x - x_{start}}{L_{\text{blade}-x_{\text{start}}}}\right)^{\gamma} \quad , \tag{1.9}$$

where y denotes the local curvature deflection (either sweep or pre-bend), d_{tip} is the tip displacement, x is the radial position, x_{start} marks the onset of curvature, L_{blade} is the total blade length, and γ controls the curvature distribution along the span.

The combination of neural networks and gradient-based optimization yielded blade designs that produced, on average, approximately 1% more power with only a slight increase in mean thrust (0.02%) compared to straight-bladed designs. However, the authors note that the effect of sweep on power output remains inconclusive and warrants further investigation (Sessarego *et al.*, 2020).

With regard to hydrokinetic turbines, no established optimization procedures have yet been reported in the literature, as noted by Gemaque, Vaz, and Saavedra (2022). The authors propose an optimization strategy for hydrokinetic turbine blades using backward-sweep angles, aiming to enhance energy efficiency, reduce axial loads, and mitigate cavitation effects. The approach is based on a modified Blade Element Momentum (BEM) theory, incorporating a radial transformation function to account for sweep effects. The local radius r is transformed into an effective swept radius r_i as follows:

$$\Phi\left(\frac{r}{R},\beta_i\right) = \left(\frac{r}{R}\right)^{\beta} \quad , \tag{1.10}$$

$$r_i = \frac{r}{R} \cdot \Phi\left(\frac{r}{R},\beta_i\right) \tag{1.11}$$

The proposed model includes adjustments to several aerodynamic parameters, including the relative velocity W, flow angle φ, twist angle θ, bound circulation Γ, Glauert's correction factor F_P, chord distribution c, and the performance coefficients C_P, C_T, and C_Q.

The optimization procedure focuses on maximizing the product $a'(1-a)$ in the power coefficient expression, leading to optimal relationships between axial and tangential induction factors, based on Glauert's classic formulations:

$$a' = \frac{1-3a}{4a-1} \quad , \tag{1.12}$$

$$c = \frac{8\pi r_i F \sin\varphi\cos\varphi}{BC_n} \cdot \frac{a}{1+a} \quad , \quad \theta = \varphi - \alpha \tag{1.13}$$

Figure 1.14 provides a schematic representation of the variable transformations involved in the swept-blade optimization:

Figure 1.14 – Simplified illustration of the variable transformation on a swept blade

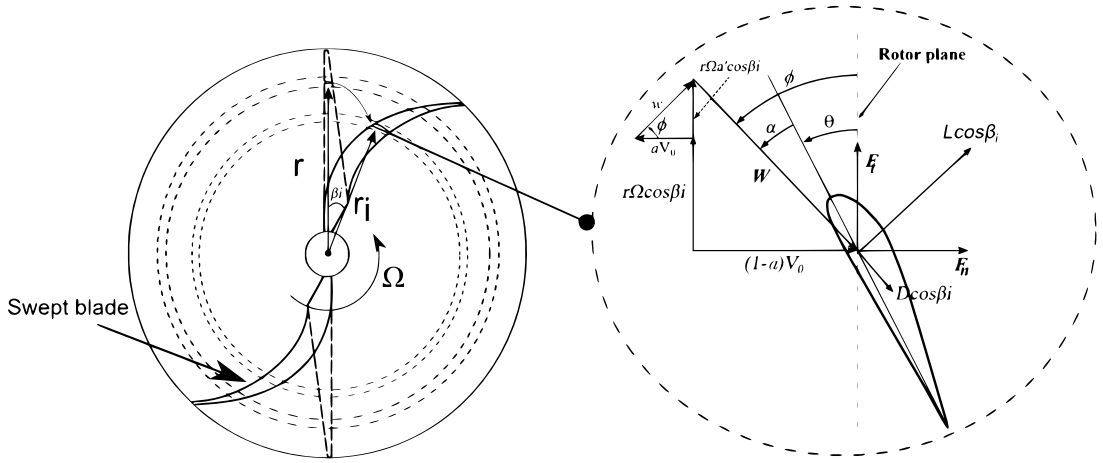

Source: (Gemaque; Vaz; Saavedra, 2022).

Using the SG6040 airfoil profile, suitable for low Reynolds number applications, the proposed implementation was validated against experimental data. At a tip-speed ratio $\lambda = 1.93$, the backward-swept blade configuration demonstrated an 81% increase in power coefficient relative to the straight-bladed reference. Additionally, regarding a global performance analysis, the torque was increased by approximately 18%, although thrust did not consistently decrease. The study also observed that Prandtl's tip-loss factor was not sensitive to sweep effects. The optimized swept-blade model achieved a power coefficient of 0.529, compared to 0.46 for the conventional configuration, approaching the theoretical Betz limit.

Overall, the methodology introduced by Gemaque, Vaz, and Saavedra (2022) shows great potential for the development of more efficient and structurally robust hydrokinetic turbines, offering performance improvements alongside reduced cavitation and axial loading.

The reviewed literature highlights the growing interest in blade sweep as a passive optimization strategy for horizontal-axis turbines, demonstrating its potential to improve power performance, reduce structural loads, and enhance cavitation resistance. Most studies,

however, focus on wind turbine applications and often rely on idealized geometries or limited operating conditions. While recent efforts have explored sweep effects through CFD, significant variations in modeling approaches, turbulence treatment, and sweep formulations hinder the establishment of consistent conclusions, particularly regarding hydrokinetic turbines, where geometric constraints and flow regimes differ substantially. In light of these gaps, the present study proposes a systematic CFD-based investigation of forward and backward sweep configurations applied to a validated hydrokinetic turbine geometry, aiming to reassess the performance trends predicted by simplified models and provide more physically grounded insights into the aerodynamic effects of blade curvature.

1.3 Objectives

Within this context, the present study aims to investigate the influence of blade sweep, based on the methodology proposed by Gemaque, Vaz, and Saavedra (2022), on the aerodynamic performance of hydrokinetic turbines through CFD simulations. The analysis is conducted using a geometry previously developed and validated by Mendes (2015), and the results presented herein seek to critically re-examine the preliminary findings reported in Souza, Oliveira, and Mendes (2024a) and Souza, Oliveira, and Mendes (2024b).

1.3.1 Specific objectives

With the intention to achieve the aforementioned goals, the specific objectives are defined:

- Model turbine geometries with forward and backward sweep configurations using various sweep angles, following the methodology proposed by Gemaque, Vaz, and Saavedra (2022);
- Implement a validated CFD approach, including a mesh independence study and the application of the k–ω SST turbulence model;
- Investigate discrepancies between CFD results and those derived analytically from the modified BEM theory;
- Validate the simulation results by comparing them with experimental data obtained for the selected turbine geometry;
- Evaluate the global performance of each turbine configuration by analyzing the power coefficient C_P as a function of the tip-speed ratio λ;
- Examine the aerodynamic effects associated with each blade configuration through the analysis of pressure fields, turbulence intensity, velocity streamlines, and wall-related parameters;
- Analyze the wake behavior associated with each geometry;

- Reassess the preliminary conclusions reported in Souza, Oliveira, and Mendes (2024a) and Souza, Oliveira, and Mendes (2024b) in light of the updated results and additional insights provided by the refined simulations.

2 Methodology

This chapter presents the methodological framework adopted to investigate the performance of hydrokinetic turbines equipped with straight, backward-swept, and forward-swept blade configurations. The primary objective of this approach is to validate the reliability of the computational fluid dynamics (CFD) models and ensure the precision of the power coefficients (C_P) calculated under various operational conditions.

Initially, the chapter describes the geometric definitions of the turbine models, detailing the parameters and modifications applied to each blade configuration. Subsequently, the CFD simulation setup and boundary conditions are presented. In particular, the use of the $k-\omega SST$ turbulence model is briefly mentioned here, with further elaboration in the simulation section, given its recognized accuracy for boundary layer and separation flow predictions.

Finally, the mesh convergence study conducted to verify the independence of the numerical results from the mesh resolution is discussed, aiming to ensure the reliability of the simulation results.

2.1 Geometry definition

Gemaque, Vaz, and Saavedra (2022) propose an extension of the Blade Element Momentum (BEM) theory to incorporate the effects of blade sweep in wind turbines. This modification is introduced through a radial transformation function, which adjusts the radial position along the blade according to the local sweep angle. The transformed radial position is defined by the following expression:

$$\Phi\left(\frac{r}{R},\beta_i\right) = \left(\frac{r}{R}\right)^{\beta_i} \tag{2.1}$$

where Φ represents the transformation function, r is the radial position, R is the turbine radius at the blade tip and β denotes the local sweep angle.

Accordingly, the radial position r_i is given by:

$$r_i = \frac{r}{R}\Phi\left(\frac{r}{R},\beta_i\right) \tag{2.2}$$

The main advantages of the modified BEM formulation include its low computational cost and ease of implementation. Furthermore, the results reported by the author indicate an increase of up to 18% in the power coefficient for a 30° backward-swept configuration. Among the limitations of the model are the simplifications regarding boundary layer behavior and cavitation effects.

The NACA 4415 airfoil was adopted for the blade profile, while the distributions of local radius, chord, twist angles, and number of blades follow the configuration proposed by Junior *et al.* (2019), which was optimized to maximize energy extraction. Their blade profiles were obtained through the classical Glauert optimization, which links axial and tangential induction factors and applies the high-induction correction, producing the chord and twist distributions that maximize power under steady, non-stalling flow. This geometry has been previously analyzed and validated through wind tunnel experiments, allowing direct comparison with the results obtained in the present work.

The adoption of this configuration ensures methodological consistency and reinforces the reliability of the simulations performed. The geometric parameters used in the turbine design are summarized in table 2.1.

Table 2.1 – Blade parameters utilized in the turbine design

Radius [m]	**Chord [m]**	**Twist Angle [°]**
0.1500	0.2900	43.6900
0.2180	0.3800	40.6800
0.2860	0.4400	37.8600
0.3540	0.4900	35.2200
0.4210	0.5200	32.7300
0.4890	0.5300	30.4100
0.5570	0.5400	28.2300
0.6250	0.5300	26.1900
0.6930	0.5000	24.2900
0.7610	0.4700	22.5200
0.8290	0.4300	20.8700
0.8960	0.3800	19.3200
0.9640	0.3100	17.9000
1.0320	0.2200	16.5700
1.1000	0	15.3400

It is important to note that the geometric parameters were scaled by a factor of 0.1 to enable direct comparison with the results obtained from wind tunnel experiments conducted on scaled turbine models. This approach eliminates the need for additional mathematical scaling, allowing direct validation of the numerical results against the experimental data.

Using a MATLAB script that implements the modified BEM theory, the geometry of a single blade was generated by inputting the maximum sweep angle β for each configuration. To illustrate the outcome of the procedure, figure 2.1 presents the geometries for the straight blade (figure 2.1a) and the 30° backward-swept blade (figure 2.1b).

Figure 2.1 – Blade geometry designed with the modified BEM theory

(a) Straight blade

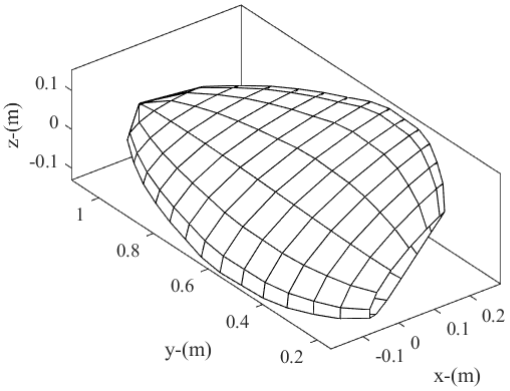

(b) 30° backward-swept blade

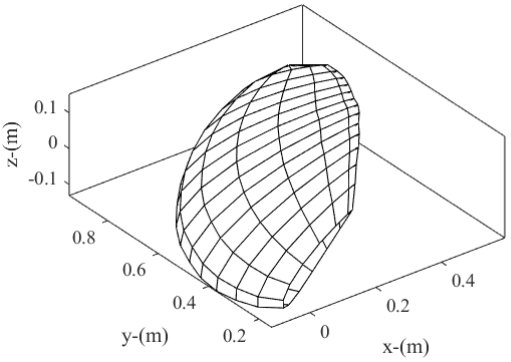

Following the same procedure, blade geometries were developed for sweep angles of 10°, 20°, and 30°, in both backward and forward orientations. It is important to emphasize that the rotor diameter was kept constant, preventing any trivial performance gains associated with an increased swept area.

Once the blade geometries were defined, three-dimensional computer-aided design (CAD) models were created for each configuration using SolidWorks. These models were generated based on spline curves exported from the MATLAB code. As shown in figure 2.2, some challenges were encountered near the blade tip, where the chord length approaches zero. To address this, the Loft function was used to complete the blade surfaces, which resulted in minor geometric imprecision near the tips for some models.

Figure 2.2 – Spline curves with cross-sectional profiles used for blade modelling

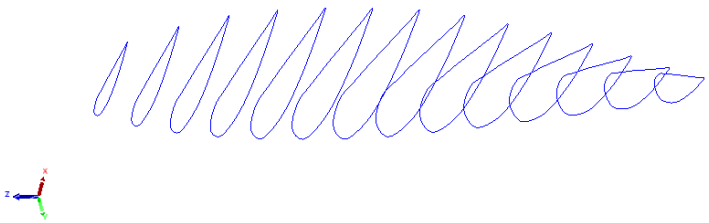

Figure 2.3 displays the resulting 3D CAD models for the straight-bladed turbine (figure 2.3b) and a backward-swept configuration (figure 2.3a).

Figure 2.3 – 3D CAD turbine models of the turbine configurations

(a) Backward-swept model

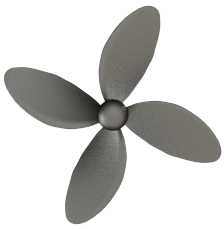

(b) Straight model

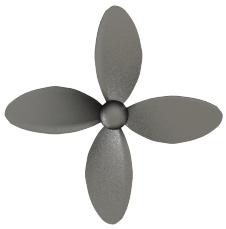

The turbine models were then imported into Ansys DesignModeler to define the geometry for the CFD simulations. A rectangular prism with cross-sectional dimensions of $4D \times 4D$ and a total length of $15D$ was defined as the stationary domain. The turbine rotor was placed at a distance of $2D$ from the inlet face and centered vertically within the prism. A cylindrical region of diameter $1.1D$, enclosing the turbine model, was defined as the rotating domain. Additionally, a second cylinder with length $6D$ was added downstream of the rotor, adjacent to the suction side, to act as a body of influence and capture wake effects more accurately.

Figure 2.4 – Geometry configuration for the CFD simulations

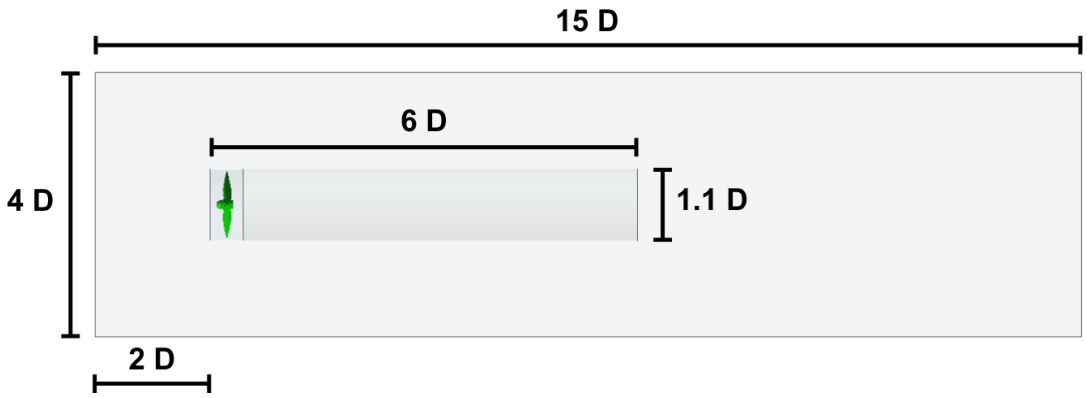

2.2 Simulation setup and boundary conditions

The simulation setup was structured to enable direct comparison with the experimental wind tunnel results reported by Junior *et al.* (2019). A steady-state simulation of standard airflow was defined, incorporating the following boundary conditions:

- **Inlet velocity:** A Dirichlet boundary condition was applied, prescribing a constant inlet velocity of 10 m/s normal to the inlet face. The pressure field was subsequently determined to satisfy the governing fluid motion equations. A medium turbulence intensity of 5% was also applied at the inlet.

- **Outlet pressure:** At the outlet face, a Dirichlet condition was imposed, setting the outlet pressure equal to atmospheric pressure, *i.e.*, zero relative pressure.
- **Openings:** The lateral faces of the domain were defined as openings with atmospheric pressure, ensuring that the domain boundaries did not interfere with the internal flow.
- **No-slip condition:** All solid surfaces of the turbine were modeled as walls, imposing zero relative velocity (no-slip condition) at the fluid-solid interface.

Figure 2.5 illustrates the arrangement of the boundary conditions within the simulation domain.

Figure 2.5 – Boundary conditions defined for the CFD simulations

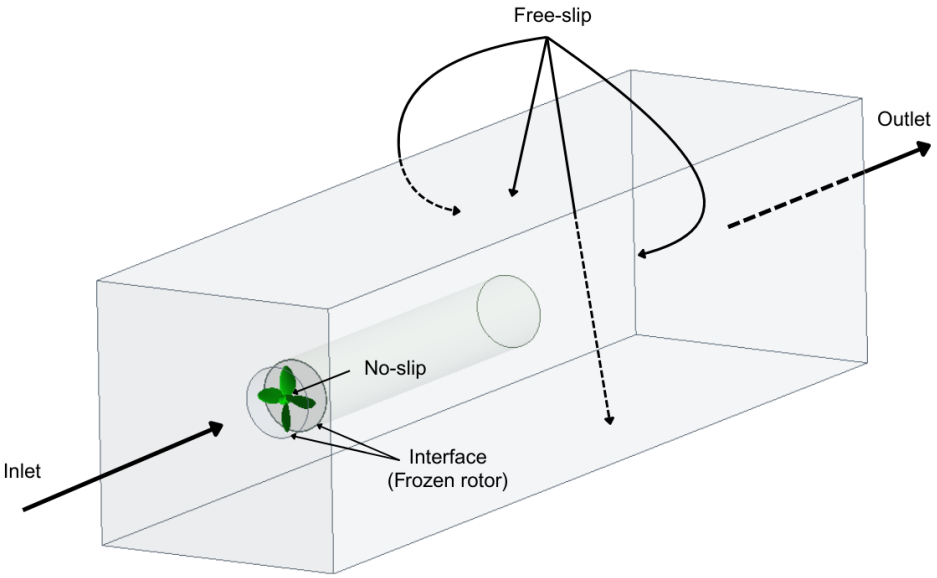

2.3 Mesh convergence study

Following the definition of the simulation geometry and boundary conditions, the meshing process was initiated using the straight-bladed turbine as the reference model. The mesh sensitivity study presented in this section addresses four key regions of the simulation domain:

- Inflation layers
- Turbine surface
- Rotating domain
- Cylinder of influence

Each of these mesh regions was analyzed individually, with the influence of element size evaluated separately for one region at a time before proceeding to the next. This approach aimed to isolate the effects of mesh refinement in each critical area of the domain.

2.3.1 Inflation layers

Given the use of an unstructured mesh, the implementation of inflation layers on the turbine surface was considered essential. These layers, composed of cells expanding in the direction normal to the turbine surface, are critical for accurately capturing boundary layer effects and resolving velocity profiles near the wall, thereby improving the prediction of wall shear stress.

In CFD, flow variables are computed with linear interpolation between cell centroids, which does not reflect the true variation of velocity or temperature near solid surfaces. Therefore, in regions with steep gradients, finer cells are required to resolve the field accurately. In the classic case of flow over a flat plate, frequently referenced in fluid dynamics studies, the velocity gradient normal to the surface is significantly larger than along the wall, *i.e.*, $\frac{\partial U}{\partial y} \gg \frac{\partial U}{\partial x}$.

Consequently, inflation layers must encompass the full boundary layer thickness δ_{99} to ensure accurate results. The mesh must also feature finer elements near the surface, particularly for simulations using the Reynolds-Averaged Navier-Stokes (RANS) approach.

As outlined by Schlichting and Gersten (2016), a key parameter used for assessing the resolution of the boundary layer is the dimensionless wall distance, y^+, represented by equation (2.3). This parameter establishes a relationship between the friction velocity u_τ, the distance from the surface y, and the kinematic viscosity ν as follows:

$$y^+ = \frac{y u_\tau}{\nu}. \tag{2.3}$$

Hence, it is necessary to estimate the total height of the inflation layers, denoted as y_T , along with determining the number of layers N. Subsequently, the first cell height y_H and the growth ratio G can be calculated.

Assuming the application of two inflation layers to a specific surface, the total height can be determined by:

$$y_T = y_H + y_H G. \tag{2.4}$$

If a third layer, larger than the previous ones, is introduced to the surface, the total height would then be calculated with the expression:

$$y_T = y_H + y_H G + y_H G^2. \tag{2.5}$$

Similarly, if N inflation layers are applied to a certain surface, the total height becomes:

$$y_T = y_H + y_H G + y_H G^2 + y_H G^3 + ... + y_H G^{N-1}, \tag{2.6}$$

or simply

$$y_T = \sum_{k=0}^{N-1} y_H G^k. \tag{2.7}$$

Equation 2.7 can be expressed as a geometric series, as described in Andrews (1998), which yields the expression:

$$y_T = y_H \frac{1 - G^N}{1 - G}. \tag{2.8}$$

Empirical correlations for estimating the boundary layer thickness can be found in the literature, such as those in Cengel and Cimbala (2013), which gives:

$$\delta_{99} = \frac{4.91L}{\sqrt{Re_L}}, \quad Re < 5 \times 10^5, \text{and} \tag{2.9}$$

$$\delta_{99} = \frac{0.38L}{Re_L^{1/5}}, \quad Re > 5 \times 10^5, \tag{2.10}$$

where Re represents the Reynolds number and L is the characteristic length of the geometry. The Reynolds number can easily be estimated based on the present work's setup, considering the fluid density ρ, the free stream velocity U, the characteristic length L and the dynamic fluid viscosity μ.

A correlation is also given by Schlichting and Gersten (2016) to estimate the skin friction coefficient c_f for $Re < 10^9$, denoted as

$$c_f = [2 \log_{10}(Re) - 0.65]^{-2.3}. \tag{2.11}$$

Once the skin friction coefficient has been computed, it is possible to determine the wall shear stress τ_w and consequently the friction velocity u_τ with the expressions

$$\tau_w = \frac{1}{2} \rho U^2 c_f, \text{and} \tag{2.12}$$

$$u_\tau = \sqrt{\frac{\tau_w}{\rho}}. \tag{2.13}$$

Last, the equation for y^+ can be expressed in terms of the distance from the geometry surface to the first cell centroid from the inflation layers y_p, with $y_H = 2y_p$ as follows:

$$y^+ = \frac{\rho y_p u_\tau}{\mu}, \text{and} \tag{2.14}$$

$$y_p = \frac{y^+ \mu}{u_\tau \rho}. \tag{2.15}$$

Based on this methodology, the inflation layer parameters for the present study were calculated under standard air conditions, with a characteristic length equal to the turbine diameter ($0.22m$), a free-stream velocity of $10m/s$, and a target $y^+ = 1$, as commonly recommended in the literature. The results are summarized in table 2.2.

Table 2.2 – Inflation layers' parameters defined for the convergence study

Mesh Parameter	**Value**
Boundary layer thickness δ_{99} [m]	2.87×10^{-3}
First cell height y_H [m]	1×10^{-5}
Growth ratio G	1.03
Number of layers	25

Figure 2.6 presents the implementation of inflation layers along the turbine surface, highlighting their role in near-wall flow resolution.

Figure 2.6 – Inflation layers applied to the model's surface

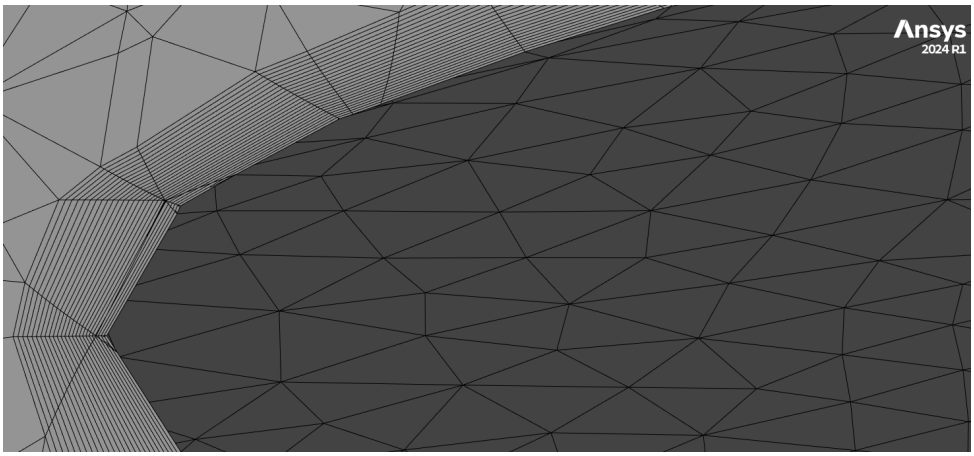

2.3.2 Turbine surface

Once the inflation parameters were defined and the geometry was imported into the meshing environment, an initial mesh was generated with the element sizes specified in table 2.3.

Table 2.3 – Initial mesh element sizes defined at the start of the mesh convergence study.

Mesh Region	Element Size [m]
Turbine surface	1e-3
Rotating domain	5e-3
Cylinder of influence	1e-2

Among all mesh regions, the turbine surface proved to be the most sensitive to the element sizes, concerning variations in the output power coefficient C_P. Therefore, it was addressed first in the mesh convergence study. Simulations were performed using varying element sizes on the blade surface, monitoring both the average dimensionless wall distance y^+ and the resulting C_P. Mesh refinement proceeded until the variation in C_P stabilized and the maximum y^+ approached unity. The results are presented in table 2.4.

Table 2.4 – Mesh refinement on the turbine surface

Element Size [m]	C_P	y^+_{ave}	y^+_{max}	Number of Nodes
1e-3	0.319712	0.513646	7.06557	1070396
8e-4	0.305454	0.535081	19.2977	1287714
7.5e-4	0.307784	0.531370	12.2752	1438529
7e-4	0.307554	0.533156	10.3696	1438529
6e-4	0.323801	0.528603	7.7530	3006120
5e-4	0.329180	0.530497	1.5925	4363448
4e-4	0.329977	0.531412	25.5131	6438026
3e-4	0.332399	0.533438	2.0383	11386616

A tolerance of 1×10^{-2} in the variation of the power coefficient C_P was defined as acceptable for this study. Based on this criterion, the turbine surface mesh was set to an element size of $5\times 10^{-4}\ m$, as the resulting variation in C_P compared to the next refined mesh was below the established threshold. Additionally, this configuration yielded a maximum y^+ value of 1.59, which is close to the recommended target value, and maintained a total node count below 5 million, thereby ensuring computational efficiency.

2.3.3 Rotating domain

Subsequently, the element sizes within the rotating domain were evaluated. As in the analysis presented in subsection 2.3.2, mesh refinement was performed until variations in the power coefficient C_P became negligible and the maximum y^+ approached unity. The results of this refinement process are summarized in table 2.5.

Table 2.5 – Mesh refinement in the rotating domain

Element Size [m]	C_P	$y^+_{\mathbf{ave}}$	$y^+_{\mathbf{max}}$	**Number of Nodes**
8e-3	0.295414	0.548875	12.2548	3060093
7e-3	0.287005	0.552669	26.1483	2147423
6e-3	0.323011	0.522279	1.4920	4075524
6.5e-3	0.308274	0.530820	42.4869	3883173
5e-3	0.329180	0.530497	1.5925	4633448
5.5e-3	0.330329	0.526516	1.5120	4251846
4e-3	0.320527	0.538066	14.9654	3368077
3e-3	0.346309	0.535754	5.8686	4686435
2e-3	0.346638	0.530076	10.4737	4473257
1e-3	0.354151	0.524860	3.5094	10460876

Based on these results, an element size of $6 \times 10^{-3} m$ was selected for the rotating domain, as it ensured minimal variation in C_P compared to finer meshes, while maintaining a low y^+_{max} and an acceptable number of nodes. This configuration provided a balance between accuracy and computational efficiency, in line with the criterion adopted in the previous step.

Figure 2.7 illustrates the mesh configuration, where the finer elements on the turbine surface and the coarser elements in the rotating domain enclosing it can be clearly observed.

Figure 2.7 – Detail of the mesh refinement in the rotating domain.

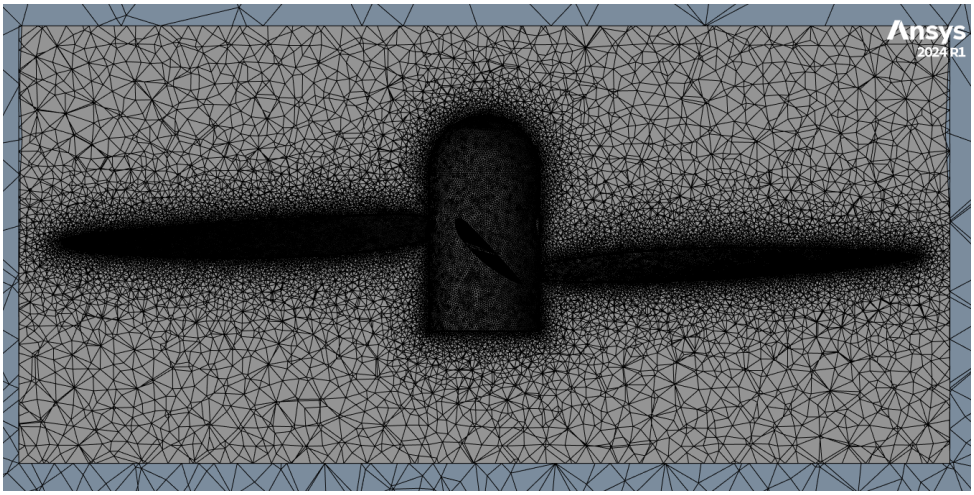

2.3.4 Cylinder of influence

To capture wake effects downstream of the turbine, a $6D$-long cylindrical body of influence was positioned at the outlet portion of the rotating domain, immediately downstream of the rotor, as described in section 2.1. A mesh sensitivity study was conducted for this region, with simulations performed using different element sizes. For each case, the

resulting power coefficient C_P and wall distance parameters y^+ were recorded. The results are summarized in table 2.6.

Table 2.6 – Refinement of the mesh elements in the cylinder of influence

Element Size [m]	C_P	$y^+_{\mathbf{ave}}$	$y^+_{\mathbf{max}}$	**Number of Nodes**
3e-2	0.327585	0.559202	19.7749	3044911
2e-2	0.307206	0.541633	16.4280	2513135
1e-2	0.323011	0.522279	1.4920	4075524
9e-3	0.303953	0.539260	12.6320	2652119

Based on these results, the element size in the cylinder of influence was set to $1 \times 10^{-2}\ m$, as it provided a refined representation of the wake region, a low y^+_{max} and consistent values of C_P, ensuring both accuracy and stability in the numerical results.

2.3.5 Number of iterations

Finally, the number of iterations required for solution convergence was evaluated. CFD simulations were conducted with varying iteration counts using the mesh configurations defined in subsection 2.3.1, subsection 2.3.2, subsection 2.3.3, and subsection 2.3.4. The results are presented in table 2.7.

Table 2.7 – Study on the number of iterations required for the convergence of the simulations.

Number of Iterations	C_P	$y^+_{\mathbf{ave}}$	$y^+_{\mathbf{max}}$
100	0.323011	0.522279	1.49201
300	0.310986	0.519821	1.48002
350	0.309827	0.519679	1.47801
400	0.309494	0.519630	1.47792
500	0.309494	0.519630	1.47792
600	0.309494	0.519630	1.47792

The results indicate that solution convergence was achieved after 400 iterations, as the power coefficient C_P and wall distance metrics stabilized beyond this point.

With the completion of the mesh convergence study, the optimal element sizes and iteration count were defined. The final mesh configuration used in the CFD simulations is summarized in table 2.8.

Table 2.8 – Final mesh configuration adopted in the CFD simulations.

Mesh Region	Element size [m]
Turbine surface	5×10^{-4}
Rotating domain	6×10^{-3}
Cylinder of influence	1×10^{-2}
Total number of nodes	4 075 524
Number of iterations	400

The resulting mesh remains within the 5-million-node limit, enabling multiple simulation runs with low computational cost and reduced processing time, while preserving accuracy and numerical stability. A visual representation of the final mesh configuration, obtained after the complete mesh convergence study, is provided in figure 2.8, illustrating the overall discretization strategy adopted for the computational domain.

Figure 2.8 – Final mesh configuration adopted for the CFD simulations.

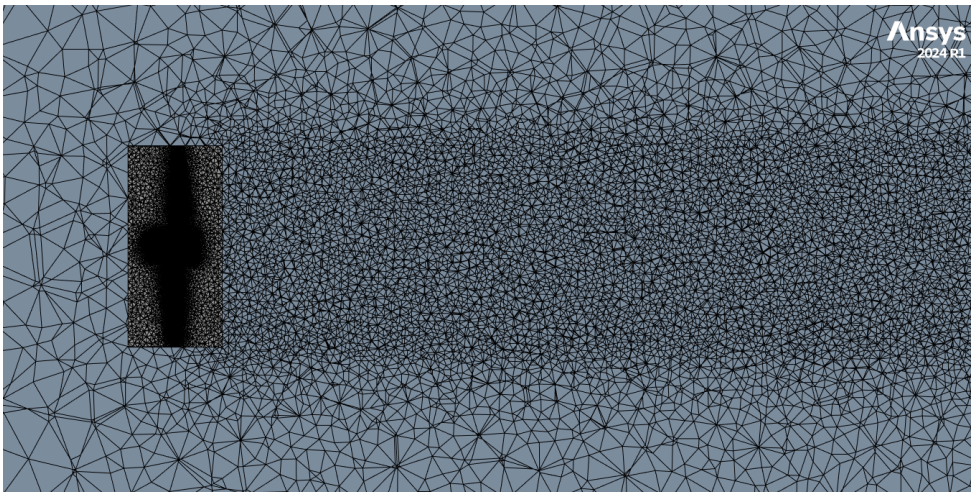

2.3.6 Mesh quality

Beyond the stabilization of the C_P and dimensionless wall distance y^+ values, additional mesh quality indicators were evaluated, including skewness, orthogonal quality, aspect ratio, and element quality. The metrics provided by Ansys Meshing revealed extreme values in specific regions of the domain. However, the zones of aerodynamic interest exhibited quality levels sufficient to ensure that the relevant flow physics were accurately captured.

- **Skewness**: This metric quantifies element distortion on a scale from 0 to 1. The mesh exhibited skewness values ranging from 0.0012 to 0.9725. Although elements with skewness above 0.95 are typically considered critical, spatial inspection showed that these elements were located far from the rotor, in regions with mild pressure and velocity gradients. The average skewness was approximately 0.2, and in regions

relevant to aerodynamic loading, values remained below 0.3, which falls within the recommended range in the literature.

- **Orthogonal quality**: This metric measures how well the elements align with geometric features and flow direction, with values ranging from 0.011 to 0.998 and an average of 0.79. Elements with orthogonality below 0.05, typically considered critical, occurred only in peripheral regions, such as transitions between inflation layers and the bulk mesh, where flow gradients are small. In the regions of interest, orthogonal quality remained above 0.7, ensuring reliable resolution of aerodynamic phenomena.
- **Aspect ratio**: Strongly influenced by boundary-layer refinement, this parameter should ideally remain below 1000. The mesh presented aspect ratios between 1.15 and 540, values consistent with recommended practices for turbomachinery simulations and boundary-layer resolving meshes.
- **Element quality**: Ranging from 0.00117 to 1, with an average of 0.35. Although elements with quality below 0.05 are often deemed as degenerate, these represented an extremely small fraction of the total elements and were confined to regions with negligible aerodynamic relevance. Since the solver achieved stable convergence and the C_P values remained consistent across refinements, it can be inferred that these low-quality elements did not compromise the simulation results.

Table table 2.9 below summarizes the mesh quality indicators obtained from the meshing software, following the sensitivity analysis.

Table 2.9 – Mesh metrics obtained after the sensibility study.

Metric	Minimum	Maximum	Average	Standard Deviation
Skewness	$1.12e^{-7}$	0.97	0.20	0.12
Orthogonal Quality	$1.14e^{-2}$	0.99	0.79	0.14
Aspect Ratio	1.16	540.35	29.01	23.92
Element Quality	$1.17e^{-3}$	1	0.35	0.39

Despite the presence of some highly distorted elements, an expected feature of unstructured meshes, these occurred only in peripheral regions with negligible aerodynamic influence. In the critical zones surrounding the rotor, the mesh exhibited adequate skewness, orthogonal quality, aspect ratio, and element quality, within the ranges recommended in ANSYS Inc. (2023). Combined with the stabilization of the C_P values and the consistent achievement of average $y^+ > 1$, these indicators confirm that the mesh provides sufficient resolution to accurately capture the boundary-layer behavior and the relevant three-dimensional flow structures across the rotor.

3 Results

This chapter presents the results obtained through CFD simulations, focusing on the influence of blade sweep angles on the performance of hydrokinetic turbines. The main objective of the analyses is to evaluate how forward and backward sweep angles applied to the turbines' blades impact the power coefficient C_P and other relevant flow properties, such as turbulence intensity and pressure distribution.

The methodology adopted in this study builds upon the modified Blade Element Momentum Theory (BEM) proposed by Gemaque, Vaz, and Saavedra (2022) to account for radial transformations induced by the sweep angle. Numerical models were created for straight blades and swept blades with angles of 5°, 10°, 20°, and 30°. The CFD simulations were conducted under identical operating conditions, allowing for a direct comparison of the aerodynamic performance among the different configurations.

The results are organized in such a way as to provide a comprehensive understanding of how blade geometry influences turbine efficiency and flow dynamics. Initially, the assessment of the dimensionless wall distance y^+ is presented, followed by an analysis of the power coefficient C_P as a function of the tip-speed ratio λ for the baseline and swept models. Further sections explore the pressure distribution on the blade surfaces, the intensity of turbulence in the wake region, and the length of pressure and velocity recovery. Finally, an assessment of flow separation, turbine solidity, and aerodynamic forces is provided to offer deeper insights into the performance characteristics of the studied turbines.

Preliminary findings from earlier stages of the present work were published in two scientific conference papers (Souza, Oliveira, and Mendes (2024b); Souza, Oliveira, and Mendes (2024a)), which highlighted the initial outcomes regarding the impact of backward sweep angles on power coefficients and a comparative analysis between forward and backward-swept blades. The following sections expand upon those results, integrating additional analyses and a more detailed discussion of the underlying physical phenomena.

3.1 Dimensionless wall distance

The dimensionless wall distance y_+ is a crucial parameter in CFD simulations, particularly when assessing the boundary layer behavior near solid surfaces. Appropriate $y+$ values are vital for accurately capturing velocity profiles and wall shear stress, which significantly affects the reliability of simulation results. In this study, the $y+$ values were monitored over the turbine blade surfaces for different sweep angles to guarantee proper resolution of the near-wall region.

Figure 3.1 displays the contour plot of y^+ values over the turbine surface obtained from Ansys CFX post-processing.

Figure 3.1 – Dimensionless wall distance y^+ contour plot for the turbine with straight blades, indicating uniform values below 1 across most of the surface

(a) Pressure side (b) Suction side

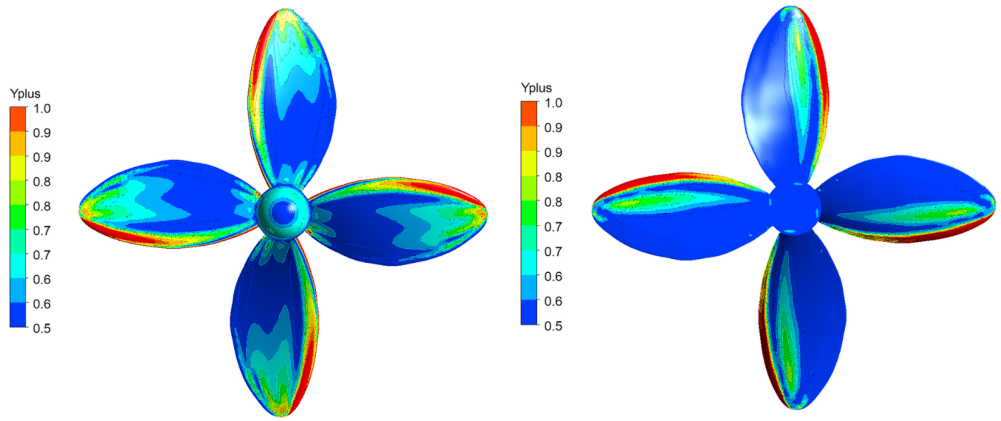

The accuracy of the CFD simulations relies heavily on the proper resolution of the near-wall region, as indicated by the dimensionless wall distance y^+. According to Schlichting and Gersten (2016), $y^+ < 5$ ensures that the viscous sublayer is captured, while $y^+ < 1$ corresponds to the purely viscous region of the boundary layer, where the flow is fully dominated by viscous forces. In this study, the mean y^+ value of approximately 0.56 and a maximum of 1.77 indicate that most of the blade surface lies within or near this purely viscous region, ensuring that the sublayer is well-resolved without the need for wall functions. In the contour plot shown in figure 3.1, the blue regions indicate y^+ values below 1, confirming that the mesh is sufficiently refined to capture the viscous sublayer. In contrast, red regions near the leading edge display y^+ values slightly above 1 (but below 5), suggesting acceptable localized flow transition.

This behavior is consistent with expected hydrodynamic physics and confirms that the mesh quality is adequate for accurately capturing wall shear stress and velocity gradients, which are critical for precise turbine power coefficient calculations.

3.2 Comparison between CFD simulations and experimental results

The simulated results of the power coefficient for the straight-bladed turbine were compared with the experimental data reported by Junior *et al.* (2019), obtained from wind tunnel experiments conducted at the Laboratory of Energy and Environment, University of Brasília. Validating the results of the numerical models is essential to ensure both the

reliability of the model and the assumptions adopted in its development. This step ensures that the CFD calculations reproduce real physical phenomena with reasonable accuracy, thereby supporting the use of the model for predictions and decision-making with scientific credibility.

The experimental setup featured an open-loop wind tunnel with a test section of $1.2m \times 1.2m \times 2m$ and a controlled airspeed up to 20 m/s, maintaining a turbulence intensity below 0.2% (Junior *et al.*, 2019). The power coefficient C_P was measured for different tip-speed ratios λ using a one-tenth scaled turbine model. Torque was measured with a torsional load cell with an accuracy of $\pm 10^{-4} N.m$ and a Wheatstone bridge at the generator shaft, with rotation regulated by a PWM-PID system. Additionally, the small-scale turbine used in the wind tunnel, with runners manufactured by 3D printing and verified for dimensional precision under $0.1mm$, provided a reliable experimental reference (Junior *et al.*, 2019).

The C_P ratio curves obtained numerically were compared with the experimental results by plotting both against the tip-speed ratio λ. A considerable discrepancy was observed between the peak values of the power coefficient, as clearly shown in figure 3.2. This difference can be attributed to several factors: friction effects in the wind-tunnel wall, absent in the CFD model, distinct turbulence levels between experimental and numerical conditions, and the omission of the turbine tower in the simulations, which tends to increase the simulated C_P values. In addition, the λ corresponding to the peak power coefficient differed between cases, with the maximum occurring at $\lambda = 1.47$ in the experiments and at $\lambda = 1.95$ in the numerical results.

Figure 3.2 – Power coefficients (C_P) vs Tip-speed ratio (λ) curves obtained from experimental data and CFD simulations using the straight-bladed turbine model.

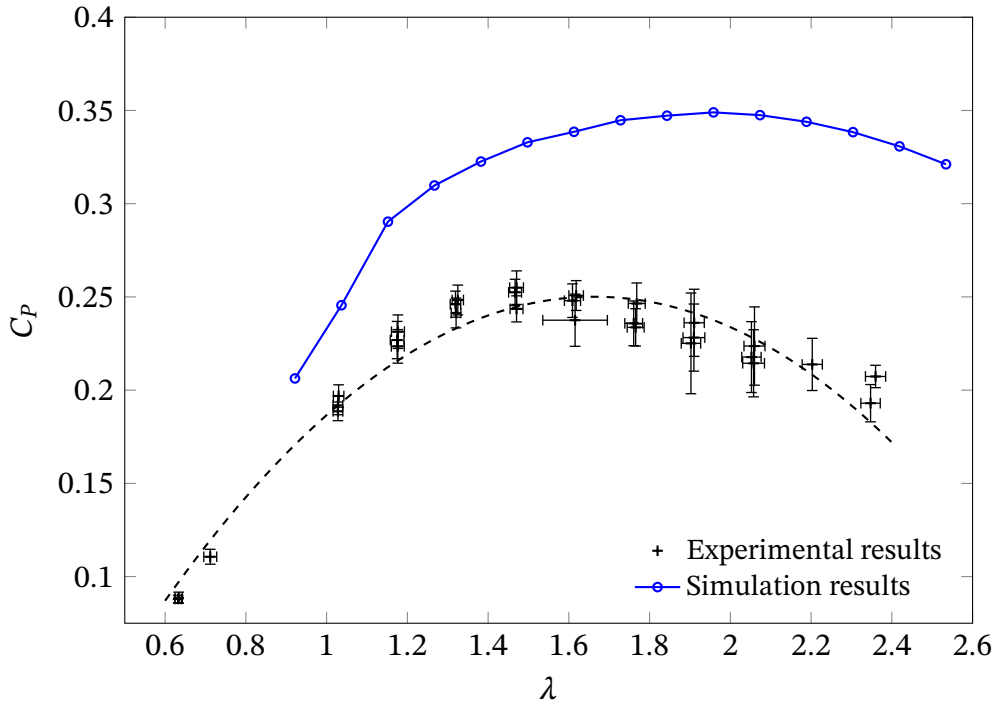

The discrepancies observed between the numerical and experimental results were non-negligible for the turbine model containing only the rotor. Therefore, a new model was developed, comprising the rotor, nacelle, and tower. The inclusion of the turbine tower was expected to bring numerical results closer to experimental data by accounting for wake interactions between the tower and rotor and the resulting turbulence effects observed in experiments. The presence of the tower and the turbine's electric motor introduces additional aerodynamic resistance, potentially reducing measured C_P values.

The mesh for the new model was generated using the same methodology described in section 2.3 (body sizing for the stationary and rotating domains, face meshing, and inflation layers applied to the turbine surface), with the addition of a mesh region and boundary condition: a body sizing of 1×10^{-3} and a no-slip condition were applied to the tower and nacelle. All other mesh parameters were kept unchanged. The final mesh consisted of approximately 5 million nodes, similar to the previous model, in order to avoid excessive computational costs. Figure 3.3 illustrates the mesh employed for the turbine model including the tower and nacelle.

Figure 3.3 – Mesh configuration adopted for the turbine model with tower and nacelle, comprised of approximately 5 million nodes.

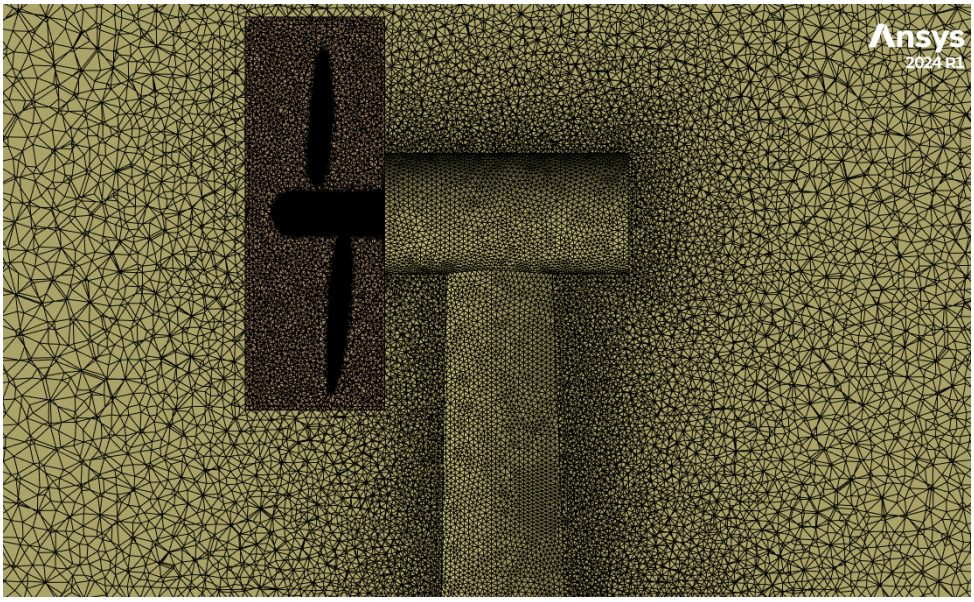

The CFD simulations that included the tower and nacelle showed results much closer to the experimental data, considerably reducing the discrepancies previously observed, as illustrated in figure 3.4. The difference between the peak C_P values was reduced to 0.03, while the corresponding λ values shifted from 1.47 in the experimental results to 1.73 in the simulations. Moreover, the overall behavior of the curves appears consistent in both cases.

Figure 3.4 – Power coefficients (C_P) vs Tip-speed ratio (λ) curves obtained from experimental data and CFD simulations using the straight-bladed turbine model including tower and nacelle.

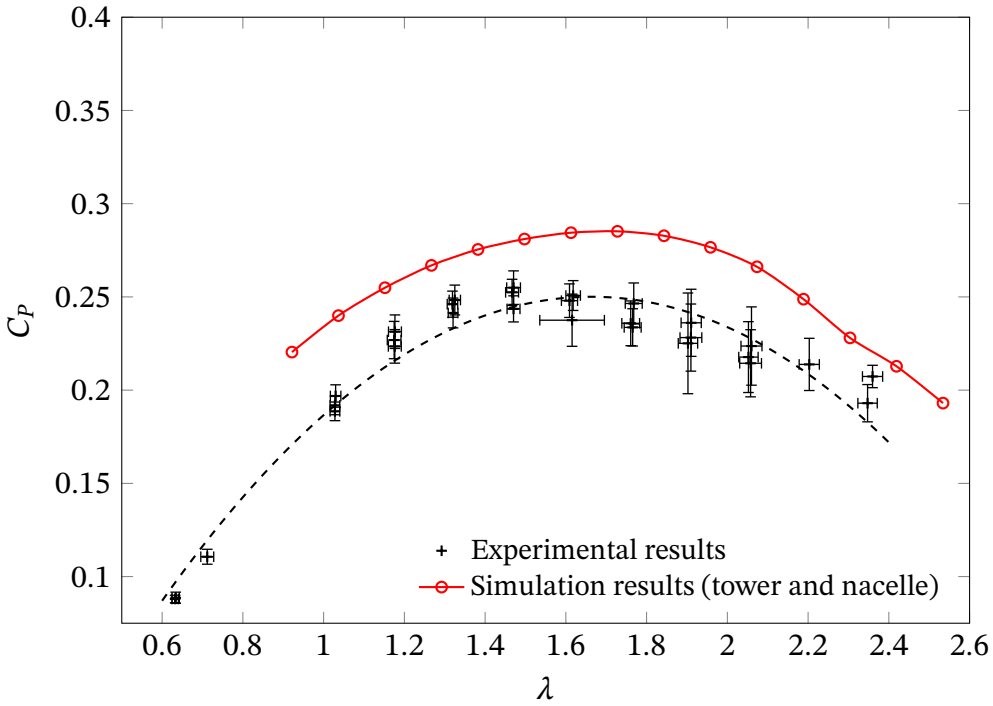

Although some differences between the two curves remain, the values are now within a much more acceptable range, considering the inherent variations between computational and experimental results, as previously discussed.

Besides the effects caused by the tower and nacelle, friction from the wind tunnel's interior surfaces can cause blockage effects, alter velocity profiles, and increase turbulence, thereby affecting the model's performance. The CFD simulations, on the other hand, assume unconfined flow and neglect these effects on the calculated C_P values. Future simulations might also feature the wind tunnel interior surfaces to account for the friction effects generated by the wind tunnel walls. According to Klein *et al.* (2018), simulations with confining walls showed a 25% variation in output power and a 50% variation in thrust compared to those without, underscoring the influence of boundary conditions on the accuracy of the results. Their study achieved good agreement for on-blade velocity and angle of attack, although deviations were observed for flow fields and bending moments. Additionally, due to the wind tunnel's short length, the impact of turbulence on vortex breakdown may be less pronounced than in far-field or longer wind tunnel scenarios (Klein *et al.*, 2018).

The comparison between the CFD simulations and experimental results highlights the impact of wind tunnel confinement effects and aerodynamic interactions on turbine performance. Discrepancies between numerical and experimental results can be associated with flow confinement, residual turbulence, and scale effects inherent to wind tunnel

testing, as described by Wiśniewski *et al.* (2021). Their work suggests that experimental measurements of aerodynamic loads and power coefficients may underestimate turbine performance due to additional drag and wake interactions from the test environment. Moreover, numerical models tend to underestimate the bending moments when compared to experimental results, reinforcing the importance of carefully modeling the test conditions. Incorporating detailed wind tunnel effects in CFD simulations can improve the agreement between numerical and experimental data, particularly in cases where the experimental setup introduces flow constraints and unsteady aerodynamic phenomena (Wiśniewski *et al.*, 2021). The above-mentioned considerations are relevant for the present work, given that the observed variations between the CFD simulations and wind tunnel experiments are likely caused by similar factors, such as the absence of the wind tunnel walls in the numerical model and the differences in turbulence intensity throughout the domain.

Although the turbine model including rotor, nacelle, and tower produced results in better agreement with experimental data regarding the power coefficient, all analyses performed in this work, such as dimensionless wall distance, pressure fields, turbulence intensity, flow separation, and pressure and velocity recovery lengths, were carried out using the rotor-only model. This choice is justified by the fact that the isolated rotor had been defined as the reference geometry, allowing the investigation of a range of geometrical variations, namely the different sweep angles applied to the turbine blades. Such simplification enabled the execution of several simulations, under both steady-state and transient regimes, with greater computational feasibility and a clearer focus on the parametric analysis.

The inclusion of the tower and nacelle, while essential to achieve higher-precision validation, introduces additional flow complexities and considerably increases computational costs. These complexities make it more difficult to isolate the specific influence of blade sweep angles on the flow behavior. Thus, although the complete model is relevant for accurate estimates of absolute performance, this is not the primary objective of the present work, which is focused on conducting a comparative analysis of different geometries and their impact on turbine efficiency and wake characteristics.

Therefore, the complete model (rotor, tower, and nacelle) was employed solely for validation purposes, confirming that the simulations with the isolated rotor, though idealized, yield physically consistent and coherent trends.

3.3 Power coefficient versus tip-speed ratio

Following the mesh sensitivity analysis and validation against experimental data, the same mesh configuration was employed for all swept-blade models. For each configuration, the power coefficient C_P was computed as a function of the tip-speed ratio λ.

Contrary to the expectations from Gemaque, Vaz, and Saavedra (2022), all swept-blade

configurations exhibited reduced performance compared to the straight-bladed reference turbine. This discrepancy may stem from limitations in the BEM method, which does not fully capture viscous effects, three-dimensional flow characteristics, and flow separation, all of which are inherently resolved in CFD simulations.

3.3.1 Backward-swept blades

The straight-blade turbine exhibited optimal C_P values within the range $\lambda = 1.5$ to $\lambda = 2.3$ (where $C_P \geq 0.95 C_{P_{max}}$), consistent with the results for all backward-swept blade models, despite the observed reductions in peak performance.

Figure 3.5 presents the C_P curves as a function of λ for the straight and swept-blade turbines.

Figure 3.5 – C_P versus λ - Backward sweep angles

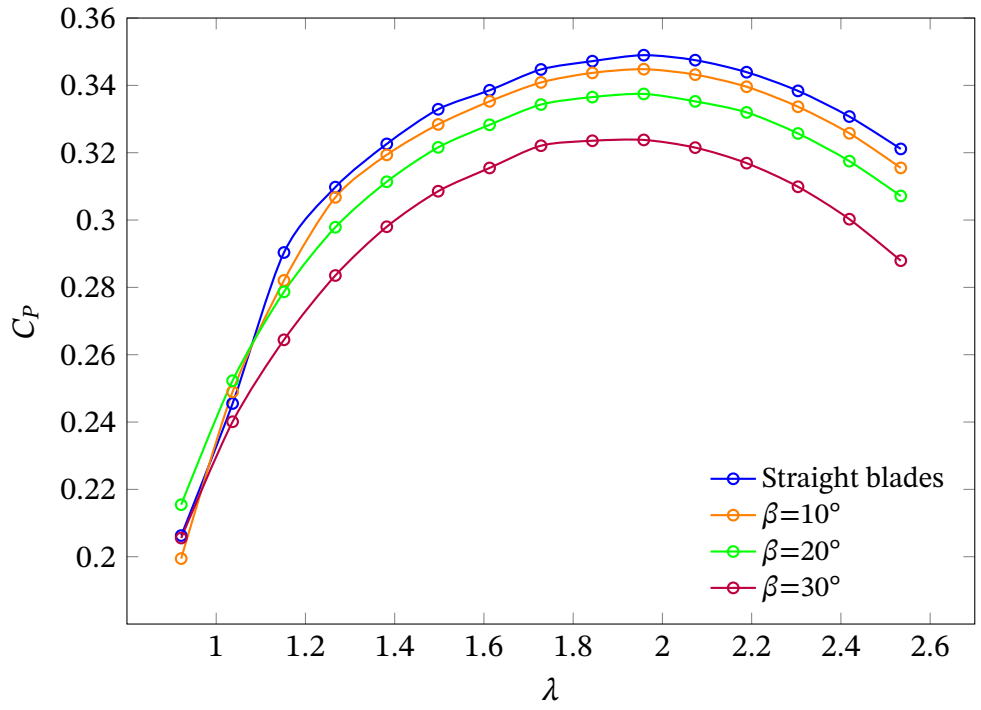

As shown in figure 3.5, all configurations exhibit stall onset near $\lambda \approx 1.04$, indicating consistent stall behavior across geometries. This observation aligns with the literature, which notes that low λ values lead to higher effective angles of attack near the blade root, increasing the probability of flow separation.

According to BEM theory, for $\lambda > 1.5$, the axial induction factor shows greater sensitivity to the flow angle and the loads in the spanwise direction. Under these conditions, the relative velocity on the blades decreases, and the ratio between tangential and axial induction factors influences the onset of stall. When $\lambda > 1$, the induction field becomes spanwise non-uniform, promoting flow separation near the root regardless of blade sweep.

Given that all models share the same airfoil (NACA 4415), and identical inlet flow and angular velocity, it is expected that the stall occurs at similar λ values. The sweep angle alters blade geometry but does not significantly affect the effective angle of attack at which stall initiates, which is primarily governed by the airfoil's aerodynamic characteristics.

3.3.2 Forward-swept blades

The optimal C_P values for the forward-swept blades occur between $\lambda = 1.6$ and $\lambda = 2.4$, indicating a slight shift in the curve compared to the straight-bladed turbine. Nevertheless, the optimal tip-speed ratio range for maximum power output remains approximately unchanged, despite the reduction in peak values.

This slight displacement may result from changes in the flow angle induced by the forward sweep, which in turn alters the load distribution along the blade. From the CFD-based performance analysis standpoint, this effect can be considered negligible. However, in practical applications, the shift in the optimal operating range may require adjustments to the generator control strategy.

Figure 3.6 shows the C_P values as a function of the tip-speed ratio λ for the forward-swept blade models, compared to the conventional configuration.

Figure 3.6 – C_P versus λ - Forward sweep angles

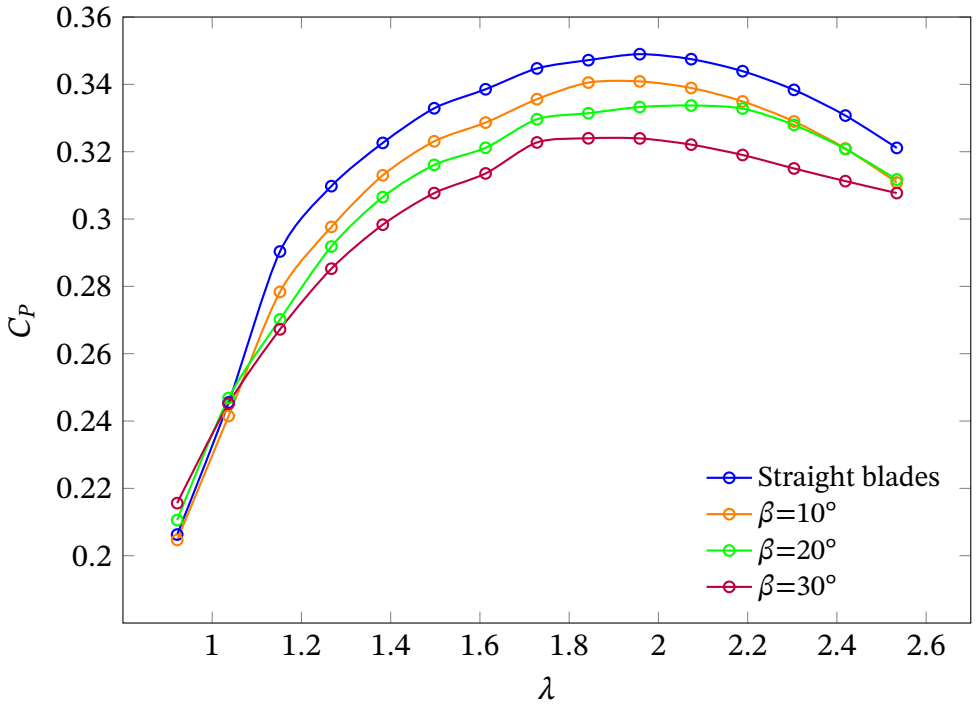

The overall aerodynamic behavior observed in the forward-swept blade configurations shares similar trends with the backward-swept cases. In particular, the stall onset occurs at nearly the same tip-speed ratio ($\lambda \approx 1.04$), and the reduction in peak power coefficient

with increasing sweep angle follows the same pattern. Given the identical airfoil profile and boundary conditions, the physical reasoning discussed in the previous subsection about the characteristics of the stall and the influence of the sweeping influence on the load of the blade can be extended to the present configurations.

The curves show a disturbance in the C_P behavior around $\lambda \approx 1.6$ for all configurations, which may be attributed to local aerodynamic instabilities. Forward sweep angles can intensify loading near the blade tip, potentially causing abrupt changes in boundary layer behavior under certain operating conditions. According to Gemaque, Vaz, and Saavedra (2022), the sweep effect increases circulation in the mid-span and tip regions, which may enhance cavitation and, consequently, the risk of aerodynamic instabilities. Additionally, blade curvature can induce three-dimensional flow fluctuations and disturbances, altering streamline curvature and redistributing momentum across the blade surface.

Since the complete CFD simulations (including pressure fields, velocity distributions, turbulence kinetic energy, etc.) were performed only at the tip-speed ratio corresponding to the peak C_P, and the remaining points on the curve were obtained through parametric simulations with C_P as the sole output, further simulations are recommended near $\lambda \approx 1.6$ to enable a more detailed investigation of the observed disturbances.

3.3.3 Relationship between torque and blade linear length

The performance analysis of the swept-blade geometries was complemented by an additional evaluation relating the total rotor torque to the linear length of each blade configuration. This assessment aimed to quantify how the geometric modifications induced by the sweep affected the torque generated on the rotor axis under the operating conditions corresponding to the maximum power coefficient. Establishing this correlation provides a clear interpretation of the mechanical implications associated with backward- and forward-sweep configurations and contributes to the definition of a compact metric for direct comparison among the geometries studied (0°, 10°, 20°, and 30° in both sweep orientations).

Since applying sweep angles inherently increases the distance from hub to tip, thus increasing the blade's linear length, it is essential to determine whether the observed torque variation is driven purely by aerodynamic effects or partially attributed to geometric extension. To that end, the linear length of the blades was calculated for all configurations and plotted against the torque values corresponding to their respective performance peaks.

Figure 3.7 illustrates the relationship between rotor torque at peak power output and the linear length of the blades. Both curves originate at the same point, corresponding to the conventional straight-bladed geometry, whose linear length equals the blade radius, and subsequently grow as the sweep angle increases. Each curve therefore contains four entries, associated with sweep angles of 0°, 10°, 20°, and 30° at their respective peak operating conditions.

Figure 3.7 – Torque versus Linear blade-length

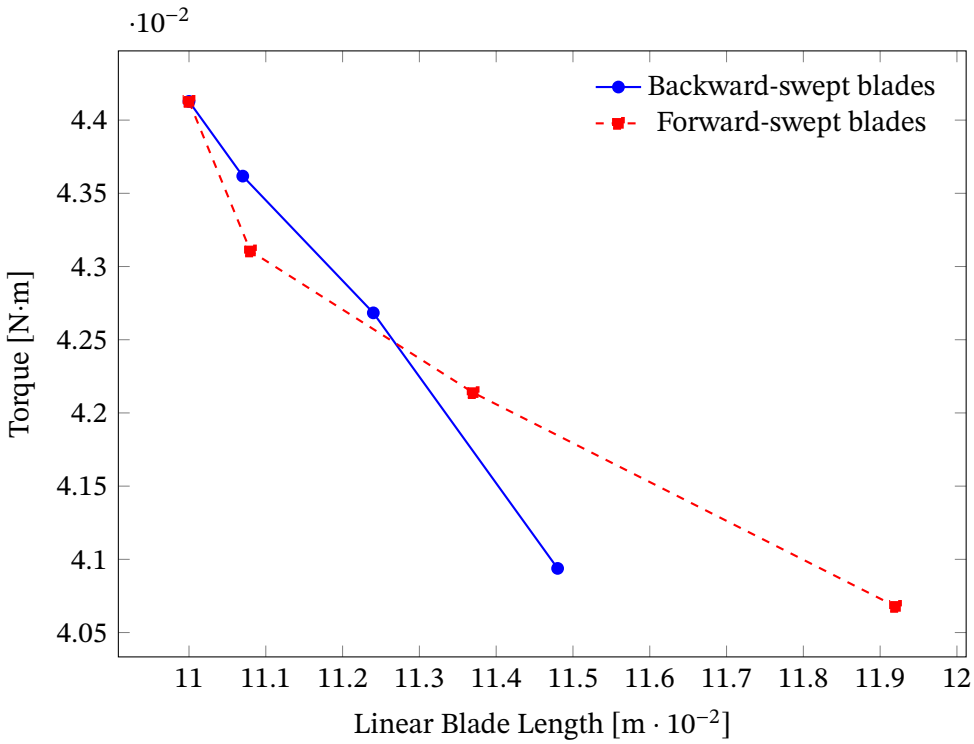

Despite the increase in linear blade length introduced by the application of sweep angles, which could, in principle, provide partial compensation through a larger moment arm and an expanded surface for momentum exchange, the results show a consistent reduction in peak torque for all swept configurations. For the largest sweep angle analyzed (30°), the torque decreased by approximately 7–8%, regardless of sweep orientation. This behavior is fully consistent with the performance degradation observed in the C_P curves presented in subsection 3.3.1 and subsection 3.3.2, where all swept-blade configurations underperformed relative to the conventional rotor.

Thus, the CFD results indicate that the aerodynamic penalties introduced by blade sweep outweigh any geometric advantage that might be expected from the increased blade length. The alterations in local flow physics induced by sweep, rather than the geometric elongation of the blades, proved to be the dominant mechanism driving the reduction in torque and, consequently, in overall turbine performance.

3.3.4 Integral control-volume evaluation of the power coefficient

The power coefficient calculated in subsection 3.3.2 and subsection 3.3.1 was obtained solely from the torque acting on the rotor axis, as computed in Ansys CFX, according to equation (3.1):

$$C_P = \frac{T\omega}{\frac{1}{2}\rho A V^3} \tag{3.1}$$

where T represents the rotor torque and ω denotes the angular velocity of the blades.

To independently verify the power coefficient values obtained from the CFD simulations, a control-volume integral approach was employed based on the pressure drop across the rotor for each turbine configuration analyzed in this work. This methodology is useful for detecting potential numerical instabilities in flows characterized by strong recirculation, steep pressure gradients, and mesh deformation. Moreover, while torque-based calculations account only for the loads acting directly on the blades, the integral method provides a global assessment of the aerodynamic behavior of the entire rotor, capturing effects that do not necessarily translate into torque but still contribute to power extraction.

For this purpose, the pressure drop across the rotor was determined using the rotating domain as a control volume surrounding the rotor. The area-averaged pressure was computed at planes located immediately upstream and downstream of the rotor, as illustrated in figure 3.8.

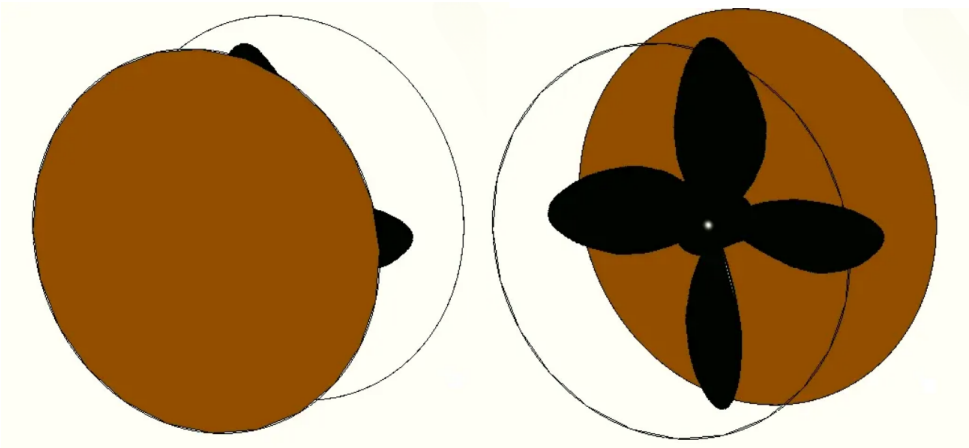

Figure 3.8 – Illustration of the control volume around the rotor, highlighting the upstream face (left) and downstream face (right) used to compute the area-averaged pressure.

Next, the pressure difference between the inlet and outlet faces of the control volume was computed and multiplied by the area-integrated flow rate entering the rotating domain to estimate the power extracted by the rotor. The procedure is summarized in equation (3.2), equation (3.3), and equation (3.4):

$$\Delta p = p_{up} - p_{down} \quad , \tag{3.2}$$

$$Q_{in} = \iint_S \vec{V} \cdot \vec{n}\, dA \quad \text{, and} \tag{3.3}$$

$$P = \Delta p \cdot Q_{in} \tag{3.4}$$

where p_{up} and p_{down} represent the area-averaged pressures upstream and downstream of the rotor, respectively; Q_{in} is the volumetric flow rate entering the control volume; and P denotes the power output computed via the integral method.

Table 3.1 summarizes the peak C_P values obtained using this integral approach and compares them with those calculated from the torque on the rotor, as presented earlier.

Table 3.1 – Comparison of peak C_P values for each turbine configuration obtained using the integral analysis and torque-based method.

Case	C_P **(integral analysis)**	C_P **(torque)**	**Variation**
Straight	0.359623	0.348785	3.11%
10° backward-swept	0.348729	0.344751	1.15%
20° backward-swept	0.336969	0.337369	-0.12%
30° backward-swept	0.326116	0.323574	0.79%
10° forward-swept	0.372878	0.340711	9.44%
20° forward-swept	0.387682	0.333063	16.40%
30° forward-swept	0.415499	0.321522	29.23%

It can be seen from the table that, for the conventional straight-bladed turbine and for all backward-swept configurations, the C_P values obtained using the integral method exhibit very small discrepancies when compared to the torque-based results. The forward-swept blades, in contrast, not only showed significantly larger discrepancies but also presented a distinct trend not observed previously: the power coefficient increased with greater forward sweep angles.

This unexpected behavior is likely associated with radial flow leakage induced by the forward-swept geometry, linked to the modified induction characteristics of these blades. Outward flow along the blade span may alter the pressure distribution across the control volume, artificially increasing the pressure drop used in the integral calculation.

To further investigate this effect, the C_P values for the forward-swept configurations were recomputed using the flow rate downstream of the rotor, calculated as:

$$Q_{out} = \iint_S \vec{V} \cdot \vec{n}\, dA \quad \text{, and} \tag{3.5}$$

where Q_{out} represents the volumetric flow rate leaving the control volume through the downstream face.

The revised results are presented in table 3.2 below.

Table 3.2 – Comparison of peak C_P values for forward-swept blade configurations obtained via downstream-flow integral analysis and via torque on the rotor.

Case	C_P (integral analysis)	C_P (torque)	Variation
10° forward-swept	0.298384	0.340711	-12.42%
20° forward-swept	0.310406	0.333063	-6.80%
30° forward-swept	0.324716	0.321522	0.99%

The updated C_P values obtained using the integral control-volume approach for the forward-swept configurations showed better agreement with the torque-based results, which depend solely on the forces acting on the blades. This reinforces the interpretation that radial flow leakage increases when forward sweep angles are applied to the turbine blades.

Therefore, the radial flow rate crossing the lateral face of the rotating domain (i.e., the lateral boundary of the control volume shown in figure 3.9) was evaluated for each turbine configuration.

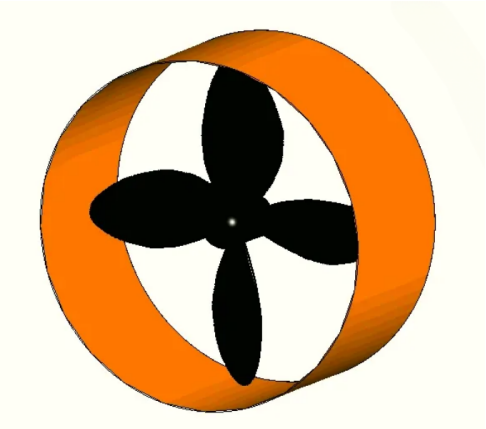

Figure 3.9 – Lateral face of the control volume, where the radial flow leakage was computed for each turbine configuration.

To quantify the radial flow leakage, the volumetric flow rate leaving the control volume was obtained by integrating the outward normal velocity across the lateral surface of the rotating domain during post-processing. This calculation measures only the fluid that escapes radially from the control volume, isolating the portion of the flow that does not contribute to the axial momentum exchange with the rotor.

The results revealed that backward-swept blades reduced radial leakage, whereas forward-swept blades enhanced it. Moreover, the larger the sweep angle, the greater the discrepancy in radial flow when compared to the straight-bladed reference. Figure 3.10 illustrates this behavior for all configurations analyzed. For clarity, negative sweep angles correspond to backward-swept blades in the following graphs.

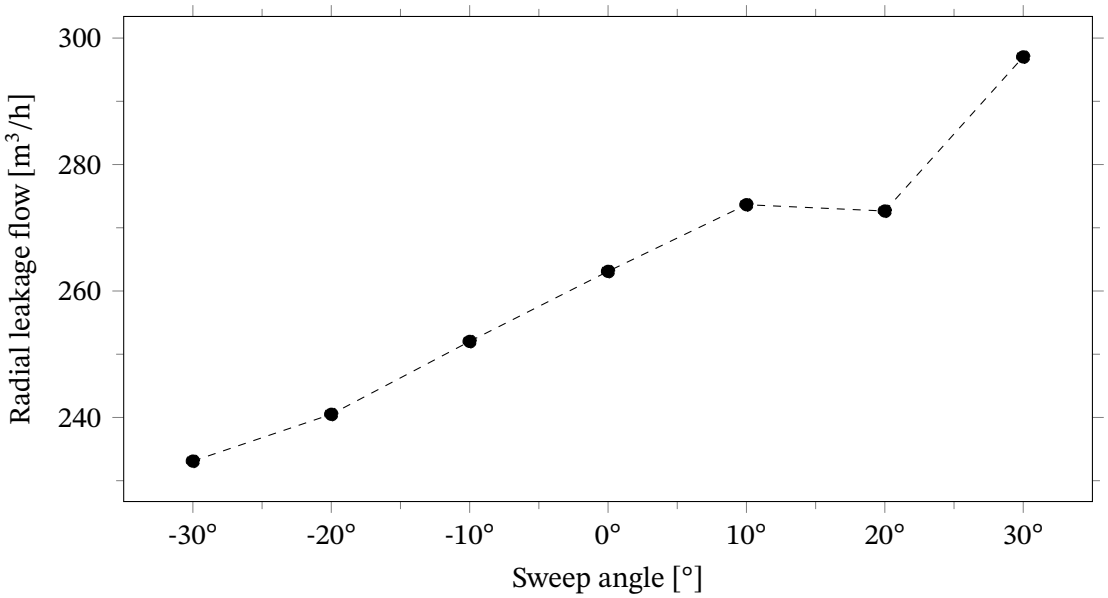

Figure 3.10 – Variation of radial leakage flow through the lateral face of the control volume for each sweep configuration analyzed. Negative sweep angles correspond to the backward-swept configuration; positive angles correspond to the forward-swept one.

The radial outflow escaping the control volume reduces the fraction of fluid effectively participating in the energy conversion process. Classical BEM theory assumes purely axial flow and disregards radial velocity components and three-dimensional effects. However, radial motion alters the relative flow velocity and the momentum balance, thereby influencing the axial induction factor a.

For the forward-sweep configurations, the increased radial leakage resulted in stronger radial velocity components, which tends to underestimate the axial induction factor a and makes the tangential induction factor $a\prime$ inconsistent with the actual vorticity distribution along the blade span. In contrast, backward-swept blades reduced the amount of flow escaping radially, leading to improved flow stability and a smoother, more coherent wake downstream of the rotor.

3.3.5 Comparison with analytical results

Using the methodology proposed by Gemaque, Vaz, and Saavedra (2022), the theoretical C_P values and induction factors for various sweep angles were calculated, later comparing these results with those of the conventional turbine. The blade geometry was optimized by maximizing the product $a'(1-a)$, following:

$$\frac{d}{da}\left[a'(1-a)\right] = \left[(1-a)\frac{da'}{da} - a'\right] = 0 \tag{3.6}$$

This simplifies to an expression also valid for straight blades, as used by Vaz, Vaz, and Silva (2018):

$$(1-a)\frac{da'}{da} = a' \tag{3.7}$$

Then, for λ >1:

$$x_i^2 a'(1+a') = a(1-a) \tag{3.8}$$

where $x_i = \frac{\Omega r_i cos\beta_i}{U_0}$. Equation equation (3.8) is derived from the angle φ in the optimization process as follows:

$$tan\varphi = \frac{a'\Omega r_i cos\beta_i}{aU_0} \tag{3.9}$$

The general expression for $tan\varphi$ is:

$$\tan\varphi = \frac{(1-a)U_0}{(1+a')\,\Omega r_i \cos\beta_i} \tag{3.10}$$

Differentiating equation (3.10) and equation (3.8) with respect to a yields:

$$\tan\varphi = \frac{(1-a)U_0}{(1+a')\,\Omega r_i \cos\beta_i} \tag{3.11}$$

As demonstrated by Gemaque, Vaz, and Saavedra (2022), combining equation (3.7), equation (3.11) and equation (3.8) results in:

$$a' = \frac{1-3a}{4a-1} \tag{3.12}$$

The optimal relationship between x_i and a is calculated by substituting equation (3.12) in equation (3.8), which results in:

$$16a^3 - 24a^2 + [9 - 3x_i^2]a + x_i^2 - 1 = 0 \tag{3.13}$$

The blade optimization procedure can be expressed as a function of the induction factors using equation (3.13). Therefore, the optimal chord and twist angles at each blade section are calculated using the following expressions:

$$c = \frac{8\pi r_i F \sin\varphi\cos\varphi}{BC_n}\frac{a}{1+a} \tag{3.14}$$

and

$$\theta = \varphi - \alpha \tag{3.15}$$

Thus, the analytically obtained peak C_P values, along with their corresponding tip-speed ratios, were computed and are summarized in table 3.3.

Table 3.3 – Maximum C_P obtained analytically for the geometries analyzed.

Case	C_{Pmax}	λ **at** C_{Pmax}
Straight	0.3483	1.9583
10° backward-swept	0.35193	2.0735
20° backward-swept	0.35166	2.1886
30° backward-swept	0.3464	2.3038
10° forward-swept	0.33959	1.9583
20° forward-swept	0.32899	1.8431
30° forward-swept	0.31477	1.8431

It can be observed that the analytically calculated peak C_P values showed reasonable agreement with the CFD results, with discrepancies of approximately 7% in the worst case. This proximity indicates that the modified BEM methodology provides reliable estimates for preliminary performance assessments of turbines equipped with swept blades.

Nevertheless, notable differences were observed in the overall shape of the curves. The reduction tendency of the peak C_P for the backward-swept blades was not observed analytically, despite the absolute values calculated being similar. As previously discussed, in the CFD simulations all C_P curves exhibited peak values within a similar λ range, with nearly coincident maxima across cases. In contrast, the analytical results revealed a systematic shift of the peak values:

Nevertheless, notable differences were identified in the overall shape of the curves. The trend of decreasing peak C_P for backward-swept blades, clearly observed in the CFD simulations, was not reproduced analytically, even though the absolute peak values were similar in magnitude. As previously discussed, in the CFD results all C_P curves exhibited peak values within a narrow and consistent range of λ, with maxima that were nearly coincident across configurations. In contrast, the analytical results showed a systematic displacement of the peak locations:

- For backward-swept blades, the maximum C_P occurred at higher λ values compared to the straight-bladed model.
- For forward-swept blades, the peak C_P occurred at lower λ values compared to the conventional turbine.

  This effect is illustrated in figure 3.11.

Figure 3.11 – C_P versus λ curves, obtained analytically.

(a) Backward-swept blades

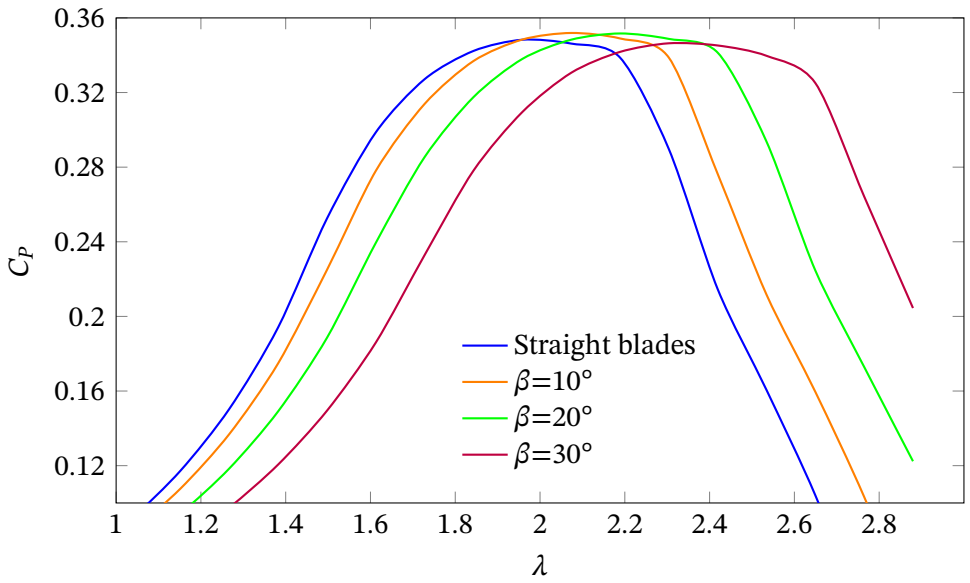

(b) Forward-swept blades

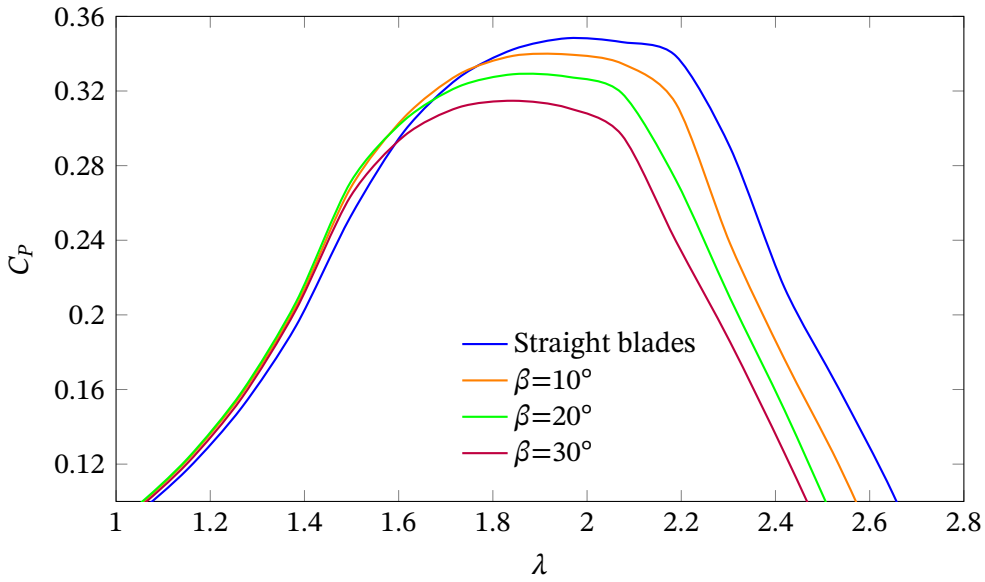

The displacement of the peaks in the curves obtained analytically may be related to how the radial transformation function and chord distribution modify the balance between axial and tangential forces along the blade span, ultimately affecting the optimal operating point predicted by the modified BEM methodology. These discrepancies can be attributed to several factors:

- Geometry modeling differences: BEM assumes thin blades with a mean two-dimensional profile, while CFD includes the full 3D geometry, thickness, and root/tip effects, af-

fecting velocity and pressure distributions.

- Three-dimensional effects: secondary flows and tip vortices in CFD are not captured by BEM.
- Boundary conditions: BEM assumes 1D flow, whereas the CFD simulations include unconfined 3D flow and lateral losses.
- Turbulence modeling: the $k - \omega SST$ model used in CFD influences power output, which is not captured in BEM.
- Viscosity: BEM does not directly include viscous effects, relying on airfoil data for lift and drag coefficients.
- BEM simplifications: axial and uniform flow assumptions contrast with deviations seen in CFD, leading to differences in C_P.
- Additional losses: CFD accounts for recirculation, tip losses, and other 3D effects, while BEM only includes Prandtl's tip-loss factor, which does not fully capture sweep effects, as stated by Gemaque, Vaz, and Saavedra (2022).

Overall, the comparison between CFD and analytical predictions showed good agreement in terms of the absolute peak values, even though the consistent reduction in C_P observed for the backward-swept configurations in the CFD results was not reproduced as clearly by the analytical model. At the same time, the discrepancies highlight the inherent limitations of BEM in capturing the full complexity of three-dimensional flow phenomena. Nonetheless, the analytical results were deemed satisfactory and sufficient to support the CFD findings, reinforcing the general trends identified throughout the study.

3.4 Pressure distribution

Having obtained the C_P curves as a function of the tip-speed ratio λ, the pressure distribution on the turbine surfaces was analyzed to further investigate the aerodynamic performance of the models and better understand the sweep effects on turbine efficiency and flow behavior.

Initially, the pressure side of the turbine models was examined to assess changes in aerodynamic loading and their relationship to torque generation for each configuration. Subsequently, the suction side was analyzed to identify regions of recirculation or lift force loss, which can indicate boundary layer separation.

For clarity of presentation, only the most representative or discrepant cases (namely, the conventional turbine and the 30° swept-blade configurations) are included in the main body of the present work. The complete set of results for all geometries analyzed, including intermediate sweep angles, is provided in the appendix A for reference.

3.4.1 Backward-swept blades

Below, figure 3.12 presents the pressure field contours on the surfaces of the straight-bladed turbine (figure 3.12a) and the 30° backward-swept model (figure 3.12b).

Figure 3.12 – Comparison of the pressure distribution on the conventional and 30° backward-swept models' surfaces (pressure side)

(a) Conventional turbine (b) 30° backward-swept model

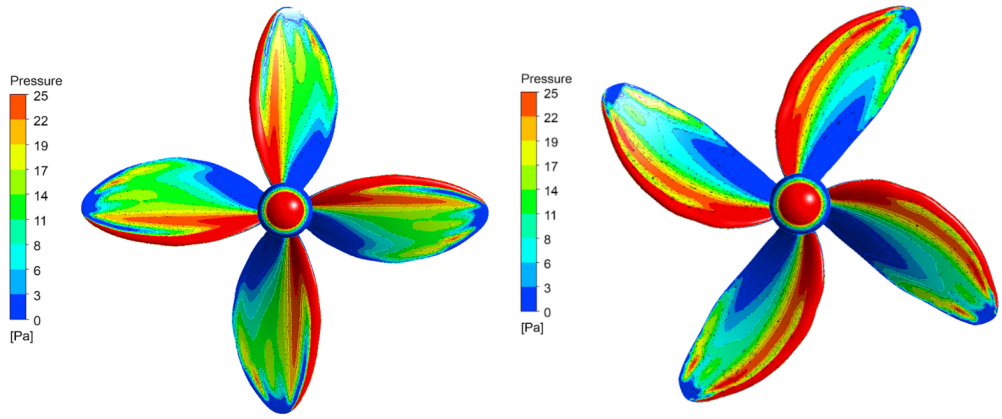

The figures indicate that the pressure on the pressure side of the blades increases with the backward-sweep angle. This suggests a rise in the normal force acting on the blade, potentially associated with enhanced lift or increased drag forces. While increased lift would typically improve the power coefficient, the backward-swept model exhibits a lower calculated C_P compared to the conventional turbine. This indicates that the higher pressure may be accompanied by greater flow instability near the blade tips, limiting torque generation and causing increased recirculation.

Additionally, a localized high-pressure region was observed near the trailing edge close to the blade tip, more pronounced in the backward-swept model. This zone likely results from a combination of factors:

- Adverse pressure gradient
- Local flow interaction with the blade geometry
- Potential overshooting issues

Initially, this effect was suspected to be a numerical artifact (overshooting) from steep gradient regions causing artificial peaks in the numerical solution. To verify the reliability of the simulation, residuals of the conservation equations were monitored throughout the simulations. At convergence, the root mean square residuals (RMS) reached approximately 1×10^{-4} or lower for the momentum (U-Mom, V-Mom, W-Mom), mass (P-Mass), and turbulence ($k - \omega SST$) equations, as detailed in table 3.4 and table 3.5. Maximum residuals remained below 2×10^{-2}, and the linear solution was deemed "OK" by the solver, confirming

numerical stability and low mean error for all equations. This consistency across other models further suggests that the observed high-pressure zone is a physical phenomenon, not a numerical artifact.

These results indicate the presence of a recirculation zone or local flow separation in these regions, which can contribute to aerodynamic inefficiencies. While higher pressure on the pressure side of the blades can enhance lift, the high-pressure zone near the blade tip on the suction side suggests a loss of the favorable pressure gradient necessary for sustained lift generation.

Equation	Rate	RMS Res	Max Res	Linear Solution
U-Mom	0.99	5.7E-05	9.0E-03	8.5E-04 OK
V-Mom	0.99	1.1E-04	2.1E-03	6.5E-04 OK
W-Mom	0.99	5.4E-05	8.8E-03	7.9E-04 OK
P-Mass	0.95	1.0E-06	3.7E-04	9.1E-02 OK
K-TurbKE	1.00	5.0E-04	6.9E-02	1.6E-06 OK
O-TurbFreq	0.99	3.0E-05	2.5E-03	1.3E-05 OK

Table 3.4 – Summary of Equation Residuals and Solutions for the straight-bladed turbine

Equation	Rate	RMS Res	Max Res	Linear Solution
U-Mom	0.99	1.4E-04	1.5E-02	6.9E-04 OK
V-Mom	0.99	2.6E-04	3.1E-02	7.7E-04 OK
W-Mom	0.99	1.5E-04	1.5E-02	7.7E-04 OK
P-Mass	0.99	3.0E-06	6.7E-04	8.6E-02 OK
K-TurbKE	0.99	1.7E-03	2.4E-01	8.2E-08 OK
O-TurbFreq	0.99	5.5E-05	3.1E-03	6.2E-05 OK

Table 3.5 – Summary of Equation Residuals and Solutions for the 30° backward-swept turbine

Thus, the intensification of pressure on the pressure side indicates that the backward-sweep angles alter the load distribution on the blade surfaces, potentially reducing tip loads while increasing overall drag forces. The localized high-pressure region near the blade tip on the suction side is particularly concerning, as it is associated with local aerodynamic efficiency losses, either due to flow separation or recirculation phenomena not captured by the BEM but resolved in CFD simulations.

Regarding the suction side pressure field, the analysis aimed to provide insights into the behavior of lift forces for both swept and conventional models, as well as the recirculation zones in the downstream flow. Figure 3.13 shows the pressure contours on the suction side of the conventional turbine (figure 3.13a) and the 30° backward-swept model (figure 3.13b).

Figure 3.13 – Comparison of the pressure distribution on the conventional and 30° backward-swept models' surfaces (suction side)

(a) Conventional turbine (b) 30° backward-swept model

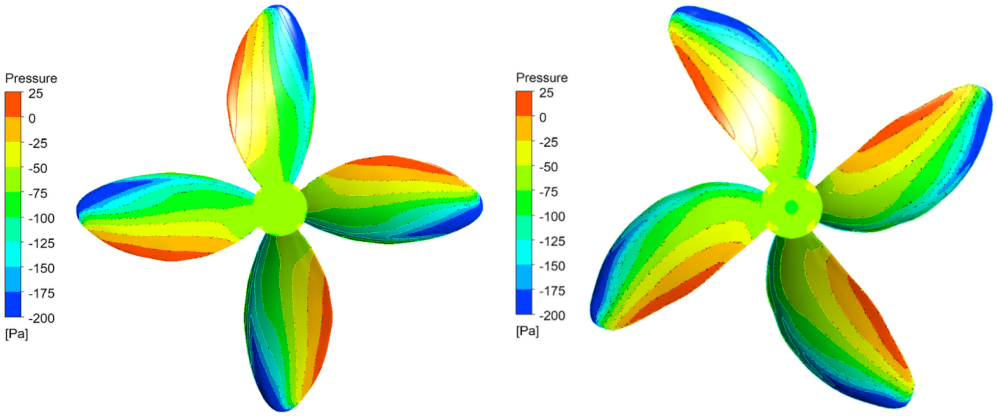

Although the overall behavior of the pressure field is similar in both models, the backward-swept blade configuration exhibits a smoother transition from blue to green and yellow tones, with slightly less intense negative pressure regions. This suggests that lower lift forces act on the suction side of the backward-swept blades, which may help to explain the lower C_P values observed for these configurations.

3.4.2 Forward-swept blades

The same analysis procedure was used to compare the pressure distributions of the conventional turbine and the forward-swept models. Figure 3.14 shows the pressure field contours on the pressure side of the conventional turbine (figure 3.14a) and the 30° forward-swept model (figure 3.14b).

Figure 3.14 – Comparison of the pressure distribution on the conventional and 30° forward-swept models' surfaces (pressure side)

(a) Conventional turbine (b) 30° forward-swept model

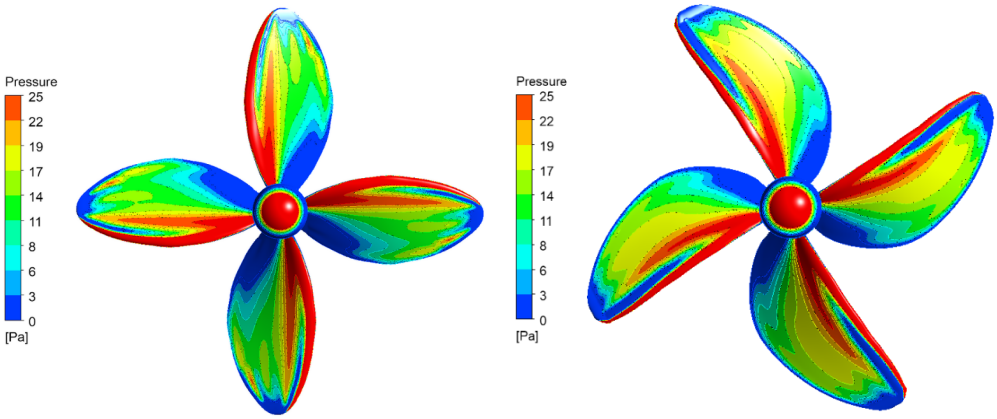

It can be observed that the 30° forward-swept model displays a more pronounced yellow region in the mid-span area, indicating higher aerodynamic loads, particularly drag, acting on the blades. In contrast, the conventional model shows a more uniform transition from high to low pressure, suggesting a more balanced aerodynamic loading and, consequently, better support for torque generation.

Moreover, the pressure field variation along the leading edge of the 30° swept blades is more pronounced compared to the conventional model. This causes rapid deceleration of the flow after the leading edge, followed by a transition to low pressure and then a recovery to higher pressures near the intermediate zone between the leading and trailing edges. The larger dark blue region observed on the swept blade surfaces suggests the presence of flow instabilities, such as partial flow separation or local recirculation. These phenomena reduce flow momentum, limiting its ability to remain attached to the blade surface, and ultimately create localized zones of energy loss, reducing the lift forces and torque generation by the blades.

On the suction side of the models, although the pressure fields appear similar for both cases, a slight change in the pressure gradient is observed in the 30° forward-swept blade model, particularly near the blade root. As shown in figure 3.15, the swept model (figure 3.15a) exhibits a smoother transition in pressure values, whereas the conventional turbine (figure 3.15b) displays a more defined distribution. Near the blade root, the yellow band is thicker in the swept model, and near the tip, the dark blue region is slightly smaller, indicating a less intense negative pressure distribution and a potential reduction in the lift forces acting on the suction side. Consequently, it can be inferred that the forward-swept model has a reduced capacity to extract energy from the flow.

Figure 3.15 – Comparison of the pressure distribution on the conventional and 30° forward-swept models' surfaces (suction side)

(a) Conventional turbine (b) 30° forward-swept model

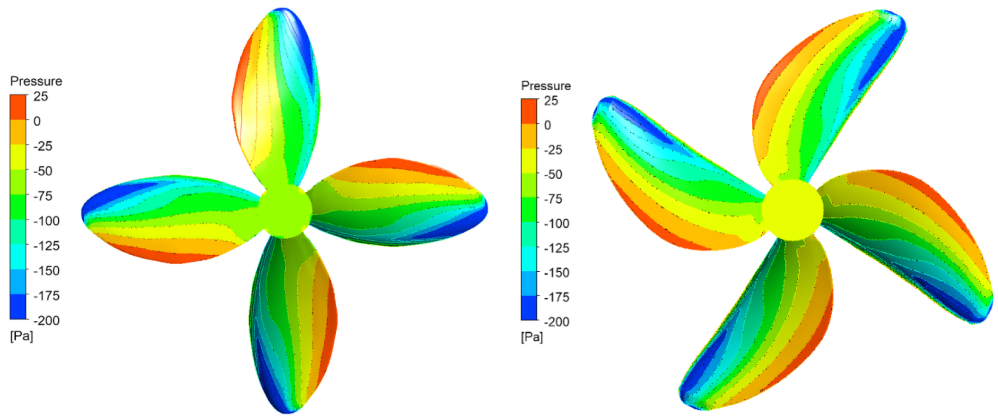

3.5 Wake turbulence analysis

The turbulence intensity downstream of the rotor was analyzed to assess the influence of the sweep angles on the wake and to gain better insight into how energy conversion and dissipation occur for each model. A qualitative analysis was conducted by plotting the turbulence intensity on the XY plane, parallel to the flow direction, along with the minimum and maximum values for each case. The analysis of turbulence intensity provides valuable insights into the aerodynamic behavior of the different configurations and allows for correlation with turbine performance.

For clarity of presentation, only the most representative or discrepant cases (namely, the conventional turbine and the 30° swept-blade configurations) are included in the main body of the present work. The complete set of results for all geometries analyzed, including intermediate sweep angles, is provided in the appendix B for reference.

Figure 3.16 illustrates the turbulence intensity fields downstream of the 30° backward-swept blade turbine (figure 3.16a), the conventional turbine (figure 3.16b), and the 30° forward-swept blade turbine (figure 3.16c).

Figure 3.16 – Turbulence intensity fields downstream of the rotors

(a) 30° backward-swept turbine

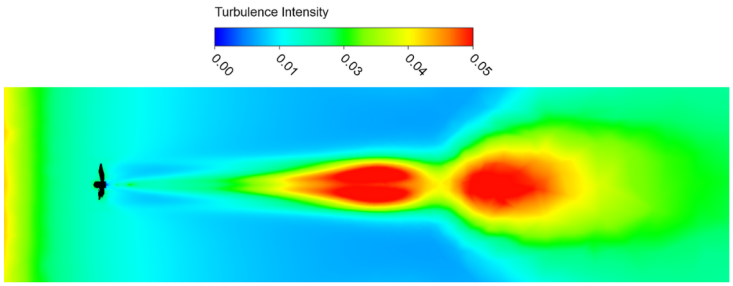

(b) Conventional turbine

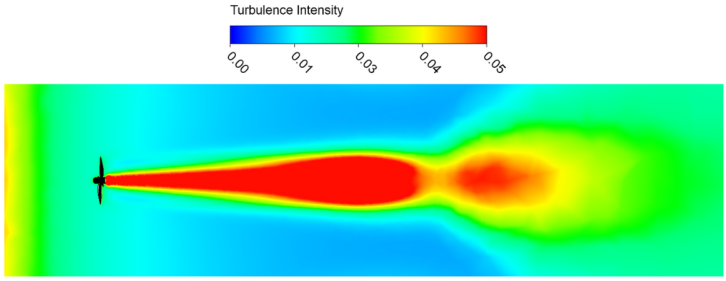

(c) 30° forward-swept turbine

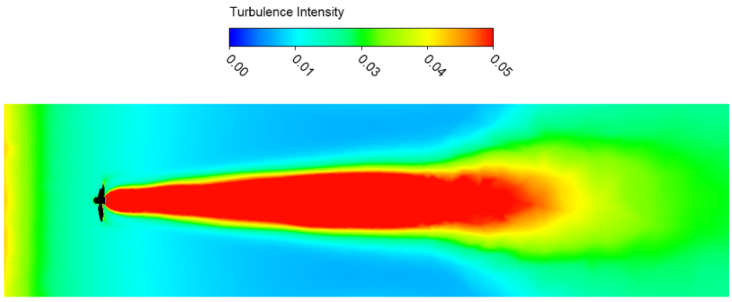

The images reveal that the backward-swept model exhibits lower turbulence intensity compared to the conventional turbine, particularly in the near wake. This reduction is typically associated with improved energy conversion and reduced energy dissipation in turbulent vortices. However, while the backward-swept wake appears cleaner, turbulence intensity cannot be directly correlated with the power coefficient, as confirmed by the lower C_P values for the backward-swept model relative to the conventional case. The alteration of the pressure field on the turbine surface is more significant in determining the energy extracted by the rotor, even when turbulence intensity is lower in some configurations. Overall, reduced turbulence intensity suggests less energy dissipation in the wake and a more stable flow, minimizing velocity and pressure fluctuations, as well as vibrations.

In contrast, the forward-swept model exhibits considerably higher turbulence intensity throughout the entire wake compared to the conventional turbine. This indicates that the residual energy is likely greater for the forward-swept model. The dark red region

downstream of the rotor is both thicker and longer, suggesting that the forward-sweep angles cause greater boundary layer disturbance and a less stable flow. While moderate turbulence intensity can sometimes enhance pressure recovery and improve the power coefficient, the lower C_P observed for the forward-swept blades suggests that the increased energy dissipation outweighed any potential benefits from energy recovery.

The images also suggest that three-dimensional effects occur in the swept-blade configurations, leading to radial flow components (cross-flow). In the backward-swept models, this cross-flow appears to move outward from the rotor, removing momentum from the rotation and reducing the torque contribution. Conversely, in the forward-swept models, the fluid flows toward the rotor, increasing the load on the hub and blade root and resulting in higher near-wake turbulence intensity, inducing recirculation and flow instabilities that reduce efficiency.

For a quantitative assessment, the peak turbulence intensity values were calculated for the wake of each configuration. It is important to note that turbulence intensity was calculated relative to a fixed reference velocity, corresponding to the inlet fluid velocity. Tables 3.6 and table 3.7 present the peak turbulence intensity values for the backward-swept and forward-swept models, respectively.

Table 3.6 – Maximum turbulence intensity for different backward-sweep angles.

Case	Maximum turbulence intensity
Straight	19.94%
10° backward sweep	15.68%
20° backward sweep	13.53%
30° backward sweep	13.75%

Table 3.7 – Maximum turbulence intensity for different forward-sweep angles.

Case	Maximum turbulence intensity
Straight	19.94%
10° forward sweep	14.23%
20° forward sweep	11.25%
30° forward sweep	11.71%

It can be concluded that, for all sweep angles — both backward and forward — the peak turbulence intensity in the wake was lower compared to the conventional turbine. However, the maximum C_P values for all swept models were also lower. This suggests that the changes in aerodynamic loading on the swept models had a more significant impact on energy extraction than the reduction in peak turbulence intensity. Lower turbulence intensity is associated with less intense fluctuations and instabilities in the wake, indicating

smoother vortex formation in the wake of the swept models.

To complement the turbulence analysis, the turbulent kinetic energy (TKE) was also plotted on the same XY plane parallel to the flow. This parameter provides a more comprehensive understanding of how energy is dissipated in turbulent fluctuations rather than being converted to torque by the turbine. Figure 3.17 illustrates the turbulent kinetic energy downstream of the 30° backward-swept turbine (figure 3.17a), conventional turbine (figure 3.17b), and 30° forward-swept turbine (figure 3.17c).

Figure 3.17 – Turbulent kinetic energy fields downstream of the rotors

(a) 30° backward-swept turbine

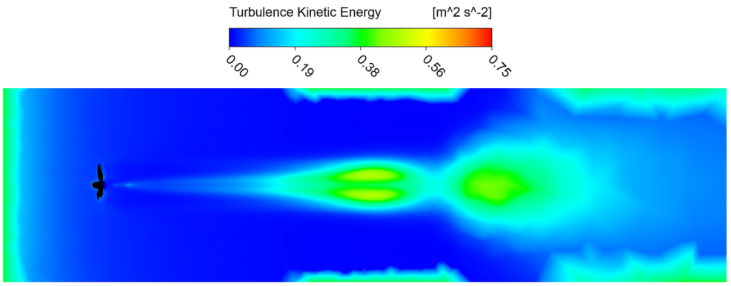

(b) Conventional turbine

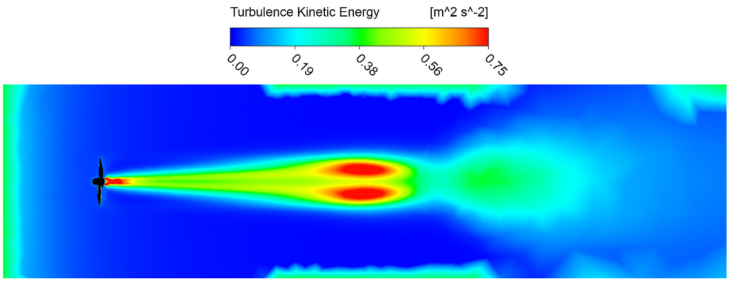

(c) 30° forward-swept turbine

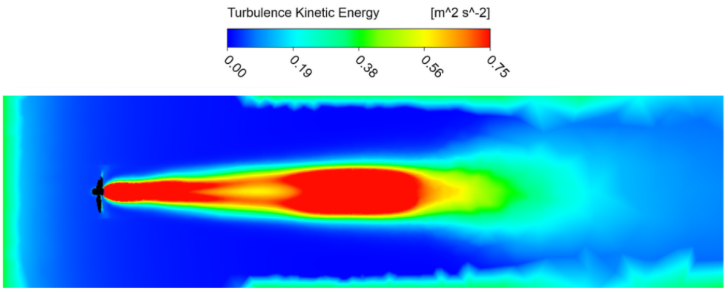

The magnitude of TKE is significantly lower for the 30° backward-swept blade model compared to the conventional turbine, particularly in the near wake. This indicates that less energy from the flow is converted into turbulent fluctuations. Although the backward-swept models demonstrated lower C_P values, they also exhibited reduced energy dissipation and a more stable wake structure. These characteristics are generally favorable for downstream flow interactions and may lead to improved hydrodynamic performance under certain

conditions.

Conversely, the 30° forward-swept model resulted in stronger TKE throughout the entire wake. The region of high turbulent kinetic energy is not only thicker but also extends further downstream, reflecting higher energy dissipation and aerodynamic losses. This correlates with the lower global energy extraction observed in the forward-swept models, as confirmed by their lower C_P values.

The peak turbulent kinetic energy values for the backward-swept and forward-swept models are presented in table 3.8 and table 3.9, respectively.

Table 3.8 – Maximum turbulent kinetic energy for different backward-sweep angles.

Case	**Maximum TKE** $[m^2/s^2]$
Straight	5.96
10° backward sweep	3.69
20° backward sweep	2.75
30° backward sweep	2.84

Table 3.9 – Maximum turbulent kinetic energy for different forward-sweep angles.

Case	**Maximum TKE** $[m^2/s^2]$
Straight	5.96
10° forward sweep	3.04
20° forward sweep	1.90
30° forward sweep	2.06

The conventional model generated the highest peak of turbulent kinetic energy downstream of the rotor compared to all other configurations analyzed. Additionally, the maximum turbulent kinetic energy value decreased with increasing sweep angle, whether backward or forward. Based on the analysis of the C_P values and pressure fields, it can be inferred that the sweep angles modify the aerodynamic load distribution along the blades, which potentially reduces pressure gradients and the contribution of drag forces to the turbine wakes.

The peak turbulent kinetic energy values systematically decrease from the straight blade case to both backward- and forward-swept configurations. However, at 30° of sweep the maximum turbulent kinetic energy slightly increases compared to 20°, for both forward and backward sweep. This non-linear behavior may be associated with the intensification of three-dimensional flow effects, reattachment zones, and localized recirculation as the blade geometry significantly deviates from the straight blade configuration. Such effects result in a mild resurgence of turbulence intensity, highlighting the complex interplay between sweep angle, flow separation, and wake development.

Overall, the combined analysis of turbulence intensity and turbulent kinetic energy in the wake confirms that swept blade geometries - both backward and forward - systematically reduce the peak levels of turbulent energy dissipation compared to the straight blade configuration. However, the aerodynamic performance measured by the power coefficient did not improve, suggesting that the redistribution of aerodynamic loads on the swept blades, particularly at higher sweep angles, more significantly affects the efficiency of energy extraction. The analysis suggests a complex interaction between three-dimensional flow effects and recirculation, which does not simply translate to better energy conversion. These results highlight the importance of considering not only the global wake stability (via lower turbulence levels) but also the local pressure field and loading patterns along the blade span, which ultimately govern the torque and power output of the turbine.

3.6 Flow separation analysis

An important aspect of turbine performance is flow separation and boundary layer detachment, as these phenomena are directly related to lift loss and energy conversion efficiency. According to Batchelor (2000), flow separation affects the pressure distribution over the attached portion of the boundary layer. Additionally, White *et al.* (2011) explains that separation occurs due to excessive momentum loss near the wall within a boundary layer attempting to move downstream against an adverse pressure gradient. In contrast, in regions with favorable pressure gradients, separation does not occur, allowing the flow to remain attached and enabling the conversion of kinetic energy into the rotor's rotation, which is directly linked to the power coefficient. The sweep angles analyzed can potentially modify how flow separation develops in these configurations. Moreover, flow separation is associated with vortex formation downstream of the rotor, helping to assess the wake effects induced by the sweep angles.

Aiming to investigate flow separation in the models developed in this work, velocity streamlines and wall shear vectors were plotted on the surfaces of all turbine models. It is noted in Batchelor (2000) that boundary layer separation occurs when there is a sudden decrease in flow velocity. Furthermore, Schlichting and Gersten (2016) states that separation begins in regions where the skin-friction coefficient reaches zero, indicating vanishing wall shear stress. The increase in the adverse pressure gradient overcomes the flow velocity, preventing fluid from moving downstream and causing boundary layer separation.

Mathematically, these effects can be expressed as:

$$\left(\frac{\partial u}{\partial y}\right)_{y=0} = 0 \tag{3.16}$$

and

$$\tau_w = \mu \left(\frac{\partial u}{\partial y} \right)_w = 0 \tag{3.17}$$

where w denotes the wall, or in this context, the turbines' surfaces (y=0).

On the pressure side of the models, velocity streamlines were analyzed in order to understand how the flow approaches the blades and how energy is conveyed along the blade profile. On the suction side, velocity streamlines reveal regions of zero velocity, indicating separation. Similarly, wall shear vectors on the pressure side indicate how the flow interacts with the blades and relate to aerodynamic loads: high values correspond to well-attached flow that effectively leverages pressure gradients for torque generation. On the suction side, zero wall shear stress denotes boundary layer separation and recirculation zones.

For clarity of presentation, only the most representative or discrepant cases (namely, the conventional turbine and the 30° swept-blade configurations) are included in the main body of the present work. The complete set of results for all geometries analyzed, including intermediate sweep angles, is provided in appendix C and appendix D for reference.

3.6.1 Backward-swept blades

3.6.1.1 Projected surface streamlines on the rotor blades

Figure 3.18 shows the surface velocity streamlines projected on the pressure side of the conventional turbine (figure 3.18a) and the 30° backward-swept model (figure 3.18b).

Figure 3.18 – Velocity streamlines projected on the turbines' surfaces (pressure side)

(a) Conventional turbine (b) 30° backward-swept model

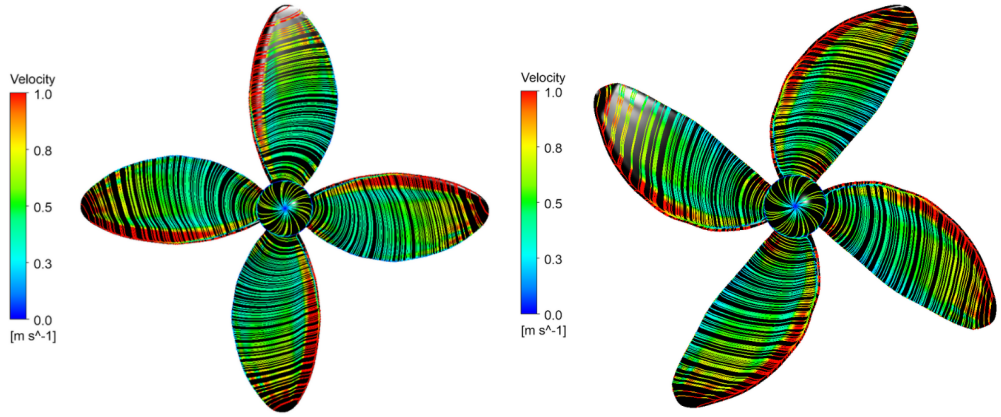

The images reveal that the flow reaches the blades of both models similarly, indicating that energy is conducted through the profiles in much the same way, despite the sweep angle. This suggests that the adherence zones and the overall flow pattern on the pressure side remain largely unchanged by the sweep angle. However, at the trailing edge of the swept model, the velocity drops to lower values (indicated by the cyan color, in contrast to the green

in the conventional model). This behavior likely results from a slight increase in the adverse pressure gradient, which may reduce the flow's capacity to maintain its kinetic energy and contribute to the lower C_P values observed for the backward-swept models.

On the suction side, the swept model exhibits fewer dark blue regions, corresponding to zero-velocity zones and, consequently, less flow separation. This effect can be observed in figure 3.19, where figure 3.19a represents the straight-bladed model and figure 3.19b illustrates the 30° backward-swept one. In addition, the pattern and direction of the streamlines appear more organized, with fewer deflections and curves indicating recirculation. These observations are consistent with the turbulence analysis for the backward-swept models, which showed a considerable reduction in both turbulence intensity and turbulent kinetic energy in the wake.

Figure 3.19 – Analysis of the velocity streamlines projected on the turbines' surfaces (suction side)

(a) Conventional turbine (b) 30° backward-swept model

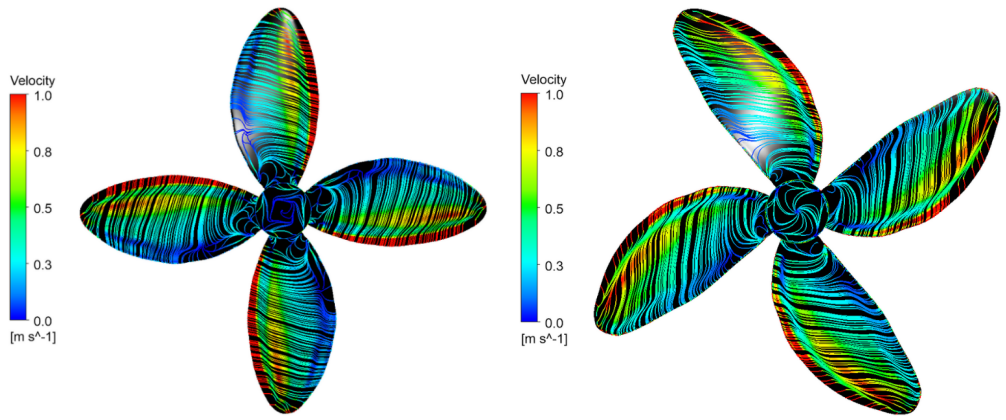

In spite of the lower C_P values for the backward-swept models, the significant reduction in boundary layer separation offers notable advantages, including lower energy dissipation into turbulent vortices, reduced drag, decreased vibration and load fluctuations. These aspects contribute to greater operational stability and enhanced durability in real-life applications.

3.6.1.2 Wall shear vectors

Figure 3.20 shows the wall shear vectors on the pressure side of the conventional turbine (figure 3.20a) and the 30° backward-swept model (figure 3.20b).

Figure 3.20 – Wall shear vectors on the turbines' surfaces (pressure side)

(a) Conventional turbine (b) 30° backward-swept model

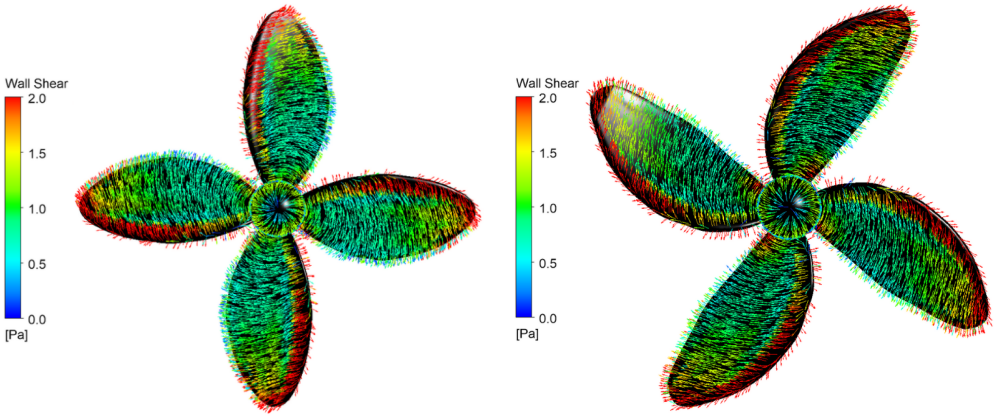

The magnitude and pattern of the wall shear vectors are generally similar for both cases, confirming that the flow incidence on the blades remains consistent for the conventional and backward-swept models. This suggests that the sweep angle did not significantly affect the skin friction on the pressure side of the blades.

However, on the suction side, as shown in figure 3.21, the 30° backward-swept model (figure 3.21b) exhibited fewer zero-friction regions compared to the conventional model (figure 3.21a). These zero-friction zones are associated with boundary layer separation and recirculation. The smaller recirculation zones observed for the backward-swept model corroborate the findings from the velocity streamline analysis and confirm the trends identified in the turbulence analysis of the wakes.

Figure 3.21 – Wall shear vectors on the turbines' surfaces (suction side)

(a) Conventional turbine (b) 30° backward-swept model

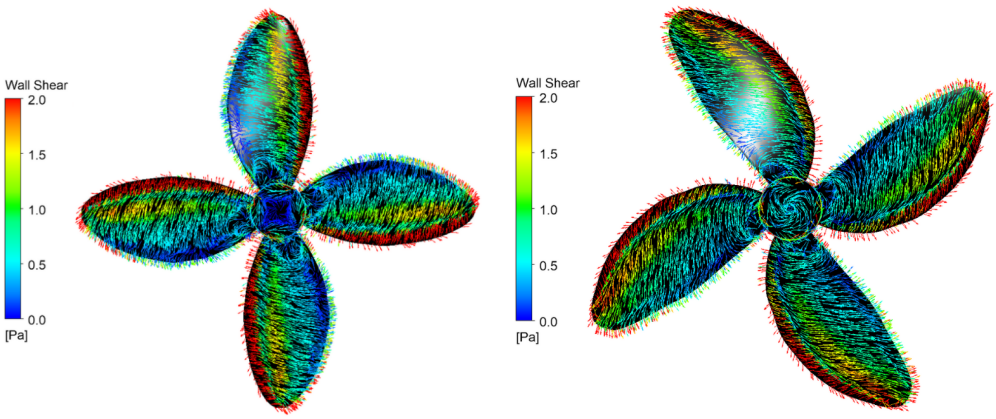

3.6.2 Forward-swept blades

3.6.2.1 Projected surface streamlines on the rotor blades

The same analysis procedure was adopted to investigate the effects of forward-sweep angles. Figure 3.22 shows the velocity streamlines on the pressure side of the conventional turbine (figure 3.22a) and the 30° forward-swept model (figure 3.22b).

Figure 3.22 – Velocity streamlines projected on the turbines' surfaces (pressure side)

(a) Conventional turbine (b) 30° forward-swept model

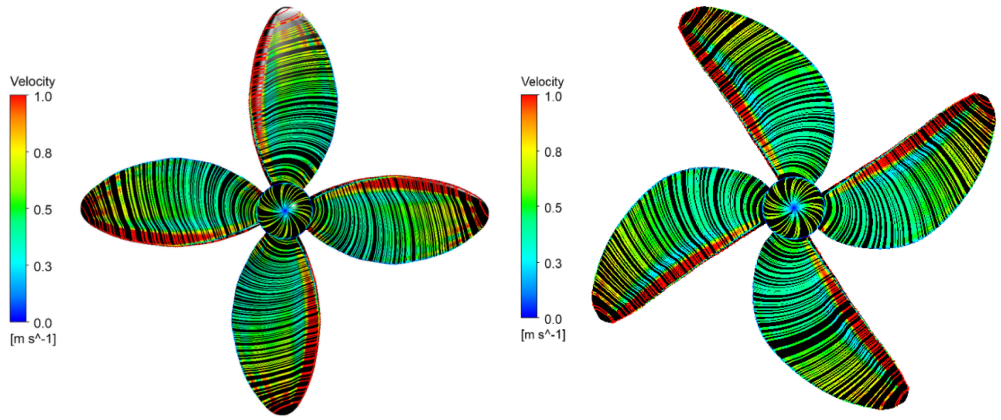

The magnitude and pattern of the streamlines on the pressure side indicate similar flow behavior in both the conventional and forward-swept models, suggesting that forward-sweep angles do not significantly impact the fluid velocity distribution on this side. Thus, the observed reduction in power coefficient for the swept models appears more sensitive to variations in pressure fields and aerodynamic loads.

Regarding the suction side of the models, illustrated in figure 3.23, the straight-bladed turbine (figure 3.23a) exhibits fewer dark blue regions (associated with flow separation) compared to the 30° forward-swept model (figure 3.23b). Furthermore, the streamlines in the forward-swept model display more abrupt curvature and deformation in some regions, further indicating the likelihood of flow separation.

Figure 3.23 – Velocity streamlines on the turbines' surfaces (pressure side)

(a) Conventional turbine (b) 30° forward-swept model

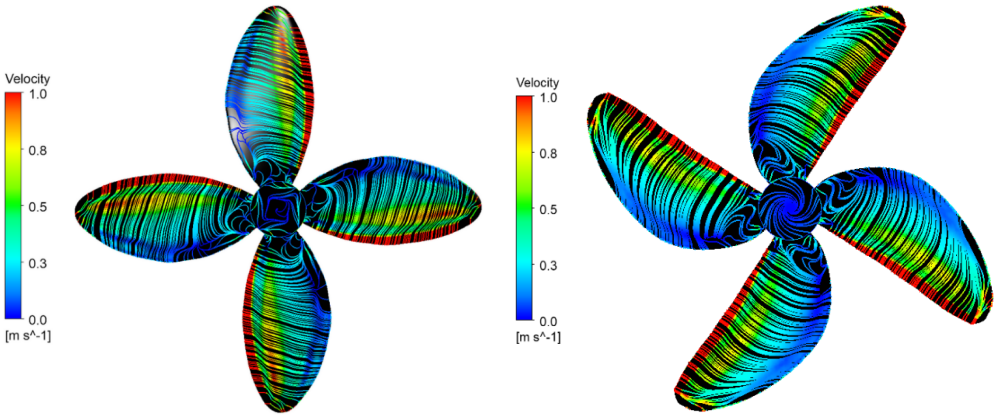

These observations suggest that the forward-sweep angle compromises the ability of the flow to remain attached to the blade surfaces, negatively impacting aerodynamic performance. The increased boundary layer separation aligns with the lower energy extraction observed in the forward-swept models, as well as with the higher turbulence intensity and turbulent kinetic energy in their wakes.

3.6.2.2 Wall shear vectors

Figure 3.24 presents the wall shear vectors on the pressure side of the conventional turbine (figure 3.24a) and the 30° forward-swept model (figure 3.24b). The patterns and magnitudes of the wall shear vectors appear similar for both configurations, consistent with the observations from previous analyses. This indicates that the forward-sweep angles did not significantly affect the skin friction on the pressure side of the blades, despite the reduction in C_P observed across all tip-speed ratio values analyzed. Therefore, the lower energy extraction in the forward-swept models is likely governed by differences in the pressure fields and aerodynamic loads, rather than by wall shear distribution on the pressure side of the models.

Figure 3.24 – Analysis of the wall shear vectors on the turbines' surfaces (pressure side)

(a) Conventional turbine (b) 30° backward-swept model

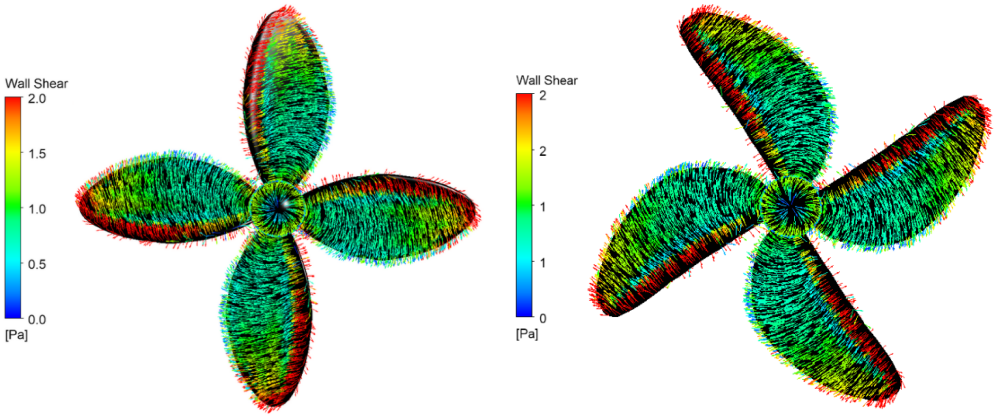

In contrast, as seen in figure 3.25, on the suction side of the turbines, the forward-swept model (figure 3.25a) exhibits a significantly larger zero-friction region in comparison with the conventional turbine (figure 3.25b), indicating increased boundary layer separation. This contributes to the lower C_P values obtained for the forward-swept configurations across the different λ values analyzed in the CFD simulations. Boundary layer separation reduces lift generation, compromising turbine efficiency and increasing the turbulence intensity and turbulent kinetic energy downstream of the rotor, as discussed in the previous section.

Figure 3.25 – Analysis of the wall shear vectors on the turbines' surfaces (suction side)

(a) Conventional turbine (b) 30° backward-swept model

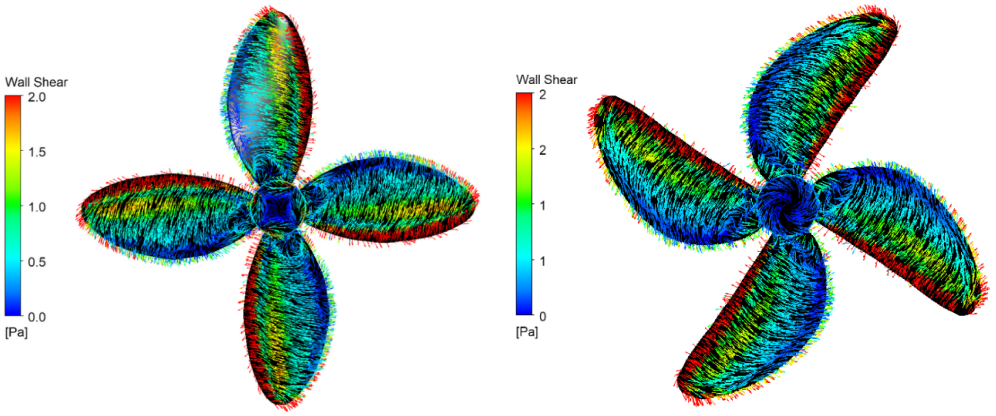

3.7 Pressure and velocity recovery lengths

To complement the analysis of the impact of swept angles on hydrokinetic turbine efficiency, the pressure and velocity recovery lengths were examined to determine the downstream distance at which the flow returns to its undisturbed state, in terms of pressure

and velocity magnitudes.

This assessment is particularly relevant in the context of turbine arrangements, such as in hydrokinetic turbine farms, as the recovery of flow energy downstream directly influences the performance of subsequent turbines. Turbines that promote faster energy recovery can enhance the overall farm efficiency, increase annual energy production, and enable higher turbine density within a given area.

To this end, a probe was positioned in the CFD simulation domain at a downstream distance of 10 rotor diameters (10D) for each configuration. The pressure and velocity at this location were then compared to the magnitudes of the undisturbed flow, providing a recovery percentage for each case.

Nevertheless, the analysis revealed that the recovery lengths for both pressure and velocity were minimal across all configurations, regardless of the sweep angle and its orientation (backward or forward). Tables 3.10 and 3.11 summarize the velocity and pressure recovery percentages at 10 diameters for the backward and forward-swept models, respectively.

Table 3.10 – Velocity and pressure recovery at 10D for different backward-sweep angles

Case	**Velocity recovery at 10D [%]**	**Pressure recovery at 10D [%]**
Straight	88.67	76.93
10° backward sweep	89.27	78.25
20° backward sweep	88.39	76.54
30° backward sweep	88.76	78.29

Table 3.11 – Velocity and pressure recovery at 10D for different forward-sweep angles

Case	**Velocity recovery at 10D [%]**	**Pressure recovery at 10D [%]**
Straight	88.67	76.93
10° forward sweep	89.44	78.29
20° forward sweep	88.45	76.55
30° forward sweep	89.81	78.91

These analyses reflect the overall balance between the flow and its environment, in spite of the variations observed across models in terms of turbulence and boundary layer separation. Over the 10-diameter distance, the wake is influenced by diffusion, dissipation, and natural recovery, smoothing out the localized alterations caused by the sweep angles.

It can be inferred that while the sweep angles significantly affect the near and intermediate wake regions, they have limited influence on the final recovery lengths of velocity and pressure.

Although the numerical values of the final recovery lengths do not vary significantly among the configurations, the progression of recovery suggests that the sweep angles alter

the reorganization path of the flow in a non-linear manner. Specifically, for both pressure and velocity recovery, regardless of the sweep orientation (backward or forward), a pattern emerges: at 10°, recovery is slightly delayed; at 20°, it is slightly accelerated; and at 30°, it is delayed to a somewhat greater extent. This pattern indicates that the sweep angles have a more substantial effect on the shape and quality of the recovery process, rather than on its final numerical value. Further investigation is recommended to explore wake lengths, dynamic loads, and interactions with downstream turbines to better understand the practical advantages and limitations of each configuration.

3.8 Flow deficit

According to Hansen (2008), the solidity of a turbine is defined as the ratio of the area occupied by the blades to the area swept by the rotor as follows:

$$\sigma = \frac{B \cdot c}{2\pi r}, \tag{3.18}$$

where B denotes the number of blades, c represents the local chord and r is the local radius.

Solidity directly influences the range of flow velocities at which the turbine can effectively extract energy. Turbines with high solidity tend to perform better at low flow velocities. However, high solidity also correlates with increased drag forces and lower C_P at higher angular velocities and tip-speed ratios. In contrast, low-solidity models operate more efficiently at higher speeds due to their reduced drag and greater lift generation capacity.

To further investigate this relationship, the flow deficit was evaluated in the CFD simulations to correlate with the solidity of each turbine configuration. The flow rate was measured at the inlet and outlet of the rotating domain, and the deficit ratio was calculated as:

$$\text{Flow deficit} = \frac{Q_{in} - Q_{out}}{Q_{in}}, \tag{3.19}$$

where Q_{in} and Q_{out} represent the flow rates at the inlet and outlet of the rotating domain, respectively.

This flow deficit quantifies the portion of the incident flow absorbed or redirected by each rotor configuration, offering insights into how the rotor interacts with the incoming flow. While the power coefficient indicates the energy extracted from the flow, the flow deficit reveals how much of the flow is modified by the rotor.

Although the final recovery lengths of pressure and velocity at $10D$ downstream were similar across configurations, the flow deficit analysis highlights how blade sweep angles affect the flow blockage effect of the turbine. A lower flow deficit may indicate a

more streamlined interaction with the flow, reducing energy losses to turbulence and wake fluctuations, and potentially benefiting downstream turbine performance in arrays.

The results are summarized in table 3.13 and table 3.12, for the backward and forward-swept models, respectively.

Table 3.12 – Flow deficit for different backward-sweep angles.

Case	Flow deficit
Straight	0.1907
10° backward sweep	0.1825
20° backward sweep	0.1733
30° backward sweep	0.1671

Table 3.13 – Flow deficit for different forward-sweep angles.

Case	Flow deficit
Straight	0.1907
10° forward sweep	0.1983
20° forward sweep	0.1973
30° forward sweep	0.2155

The results indicate that backward-swept models reduce the flow deficit as the sweep angle increases, whereas forward-swept models exhibit the opposite behavior: larger sweep angles lead to greater flow deficits. For the backward-swept models, this suggests that despite lower power coefficients, these configurations interact with the flow more smoothly, consistent with the previous turbulence and flow separation analyses. In contrast, forward-swept models introduce more blockage and disturbances to the flow, leading to a more disruptive effect compared to both the conventional and backward-swept configurations. This adversely affects energy conversion and can impact the performance of downstream turbines in an array.

3.9 Transient simulations

In addition to the steady-state simulations performed for all turbine geometries, transient simulations were carried out for three representative cases: the conventional straight-bladed turbine, and the swept-blade turbines with 30° curvature (in both backward and forward configurations), which exhibited the most significant deviations in performance. These unsteady simulations aimed to validate the steady-state results and provide deeper insight into the dynamics of the interaction between the turbine and the flow.

While the steady-state approach using the Frozen Rotor model offers a computationally efficient estimate of the average aerodynamic performance, it inherently neglects temporal variations in the flow field. Transient simulations, in contrast, allow for the resolution of blade-passing effects, unsteady wake structures, and potential flow instabilities that cannot be captured under steady assumptions.

The simulations were conducted at an angular velocity of 178.02 rad/s, which corresponded to the peak power coefficient observed under steady-state conditions for the selected cases. Additionally, each transient simulation covered approximately 10 full turbine revolutions, totaling 0.35 seconds of simulated time with a timestep of 0.002 seconds.

In order to ensure accurate modeling of the fluid-structure interaction between the rotating blades and the flow, the Transient Rotor-Stator coupling method was employed within Ansys CFX. This approach maintains the relative motion between the stationary and rotating domains over time, which is essential for a realistic representation of flow fluctuations, vortex formation, and transient variations in torque and pressure.

The transient simulations enabled the evaluation of time-dependent quantities, such as power coefficient fluctuations and wake development. The analysis allowed for the verification of the consistency of the steady-state results and the identification of transient effects that may influence overall performance.

It was observed that the variables and quantities evaluated under steady-state conditions exhibited analogous behavior in the transient simulations, with comparable values for parameters such as pressure fields, velocity, and wall shear stress. Regarding the power coefficient, the swept-blade models showed a similar reduction in efficiency compared to the straight-bladed turbine. The results obtained are summarized in Table 3.14.

Table 3.14 – Power coefficient obtained from transient simulations for the straight-bladed turbine, 30° backward-swept, and 30° forward-swept models.

Time [s]	**Straight blades**	**30° backward-sweep**	**30° forward-sweep**
0.1	0.355312	0.323514	0.333776
0.2	0.355162	0.323152	0.328715
0.3	0.355555	0.32333	0.327173
0.35	0.355277	0.323415	0.326708

In the transient simulations, both the forward- and backward-sweep configurations resulted in a power coefficient between 0.32 and 0.33, whereas the conventional model achieved a C_P of 0.35. Although the steady-state simulations had indicated a more pronounced reduction in power capture for the forward-sweep configuration and a slightly smaller reduction for the backward-swept blades, the values obtained from all transient simulations remained numerically close to one another.

Therefore, it was considered that the most relevant findings from the swept-blade

geometries are associated with wake structure, turbulence characteristics, and the pressure and velocity drop across the rotor—as well as the recovery of these quantities downstream. Accordingly, the present chapter focuses on discussing these wake-related effects for the selected cases.

3.9.1 Mesh and dimensionless wall distance

To verify the suitability of the near-wall mesh for capturing the boundary layer behavior in transient simulations, contour plots of the dimensionless wall distance y^+ were generated for the three turbine configurations. The results shown correspond to the final timestep of each simulation (0.35 s), as the y^+ values remained stable throughout the transient analysis, disregarding the first few iterations, when the simulations were not yet stable.

Figure 3.26 presents the y^+ distributions from the frontal view, while figure 3.27 shows the rear view, highlighting the blade surfaces. In all cases, the boundary layer remained within the viscous sublayer, which confirms the adequacy of the mesh for resolving wall-bounded flow features. For the conventional turbine, the maximum y^+ observed was approximately 1.79, with an average value of 0.56 across timesteps. The average y^+ remained consistent through all cases. The forward-swept configuration yielded a slightly higher peak of 3.29, while the backward-swept geometry reached a local maximum of 15.52, although this was limited to very localized regions near the blade root and trailing edge.

Figure 3.26 – Dimensionless wall distance obtained from the transient simulations (pressure side of the turbines)

(a) 30° backward-swept model (b) Conventional turbine (c) 30° forward-swept model

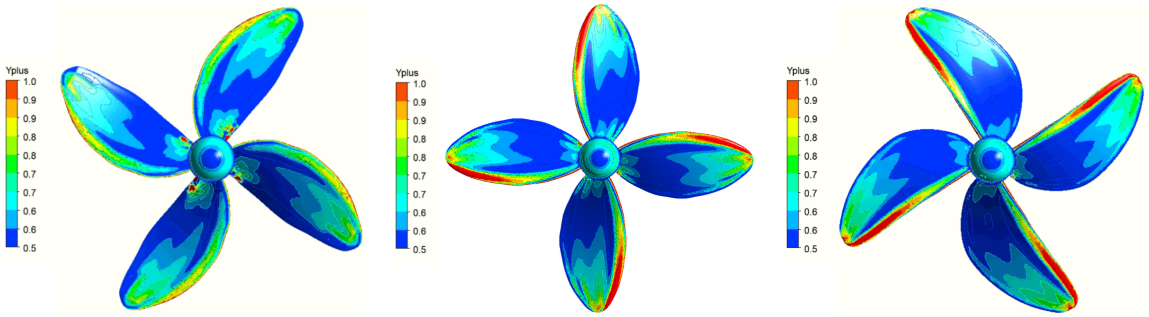

Figure 3.27 – Dimensionless wall distance obtained from the transient simulations (suction side of the turbines)

(a) 30° backward-swept model (b) Conventional turbine (c) 30° forward-swept model

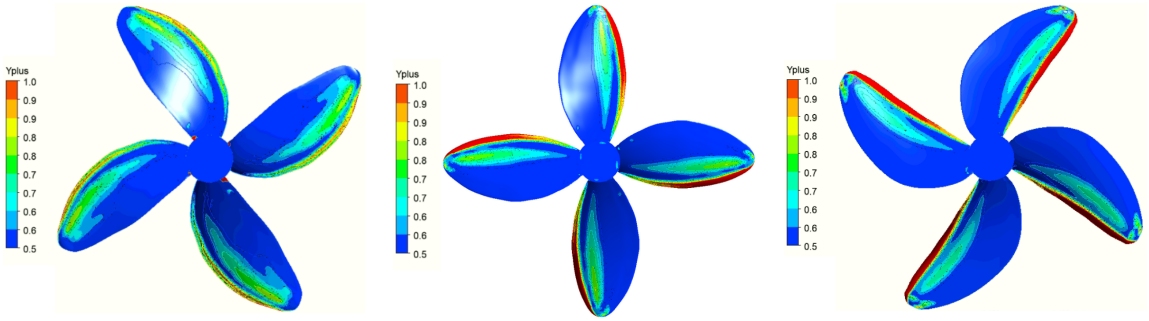

No significant differences were observed between the steady-state and transient simulations regarding the dimensionless wall distance values, reinforcing the consistency and robustness of the near-wall mesh design across different operating conditions. The turbine walls were modeled using standard no-slip boundary conditions with the default near-wall treatment provided by Ansys CFX.

3.9.2 Wake structure and turbulence effects

Given the steady-state analysis performed on the swept-blade models, where no significant improvements were observed in the power coefficient, the most noteworthy phenomena were instead related to the wake behavior. One of the most significant effects was observed in the turbulence downstream of the rotors, where the backward-swept blades exhibited improvements in both turbulence intensity and turbulent kinetic energy.

Figure 3.28 illustrates the turbulence intensity on the XY plane for the 30° backward-swept turbine (figure 3.28a), the straight-bladed turbine (figure 3.28b), and the 30° forward-swept turbine (figure 3.28c).

Figure 3.28 – Turbulent intensity fields downstream of the rotors

(a) 30° backward-swept turbine

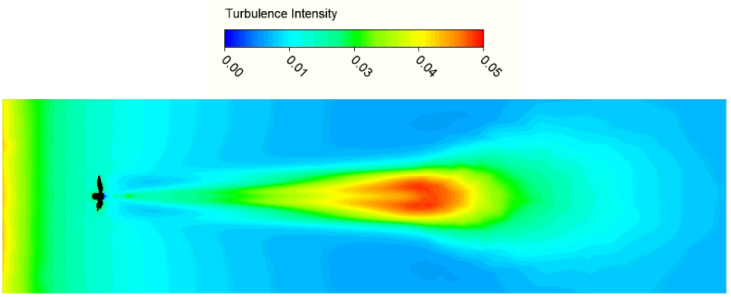

(b) Conventional turbine

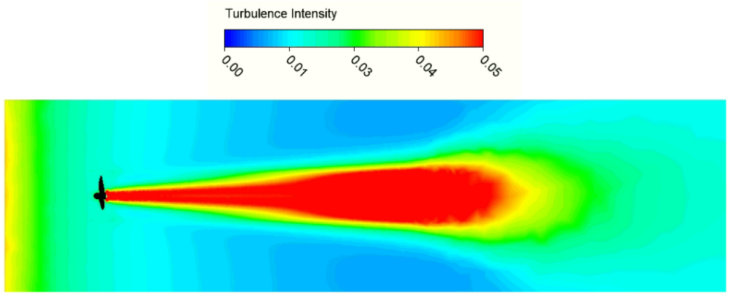

(c) 30° forward-swept turbine

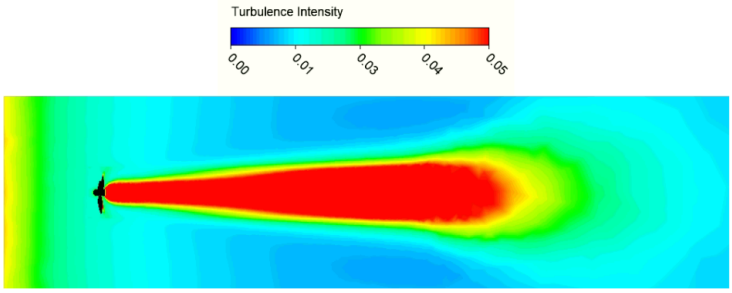

From the figure, it is evident that the high-turbulence regions in the wake are substantially smaller for the backward-swept blade configuration. Both the conventional and forward-swept turbines exhibited broader regions with elevated turbulence intensity, with the forward-swept model displaying the most pronounced effect.

Beyond this qualitative observation, the turbulence intensity fields provide a comprehensive view of wake development downstream each turbine. As seen in figure 3.28, the backward-swept configuration resulted in a narrower and more stable high-turbulence region, which dissipates more rapidly compared to the other models.

This reduced lateral dispersion and intensity of turbulence suggests that the backward-swept geometry promotes a more coherent and less chaotic wake, likely due to smoother flow separation and improved boundary layer control along the blade span. In contrast, the forward-swept configuration not only increased the peak wake thickness but also extended the presence of turbulence further downstream.

From a fluid dynamics perspective, the observed reduction in turbulence intensity downstream of the backward-swept blades indicates a more gradual energy extraction process, leading to lower shear and eddy formation. Such behavior can be interpreted as a more favorable fluid-structure interaction, potentially leading to reduced fluctuating loads on the rotor and lower long-term fatigue.

Moreover, in the context of hydrokinetic turbine array planning, a more stable and narrower wake is advantageous, as it enables tighter spacing between adjacent units without significant performance penalties. This could translate into higher energy density per unit area and more compact turbine farms, which is particularly beneficial in space-constrained environments such as rivers or tidal channels.

Although the peak values of turbulence intensity were slightly higher for both swept configurations (up to 13.79%) compared to the straight-bladed model (12.26%), this increase appears to be localized and does not undermine the overall improvements in wake structure observed in the backward-swept case. Therefore, even if the sweep angle does not enhance the power coefficient under steady-state conditions, it plays a decisive role in downstream flow dynamics and in improving wake characteristics.

Regarding turbulent kinetic energy (TKE), a similar behavior was observed when plotting the variable on the same XY plane, as shown in figure 3.29 below.

Figure 3.29 – Turbulent kinetic energy fields downstream of the rotors

(a) 30° backward-swept turbine

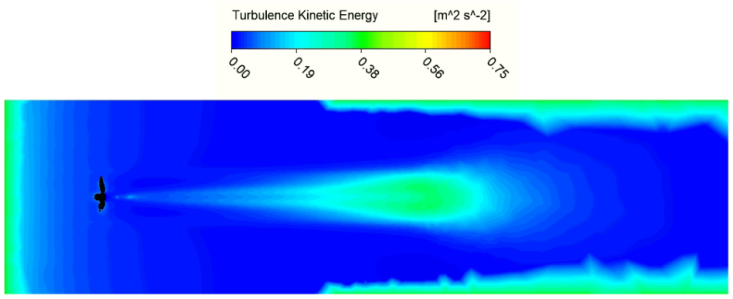

(b) Conventional turbine

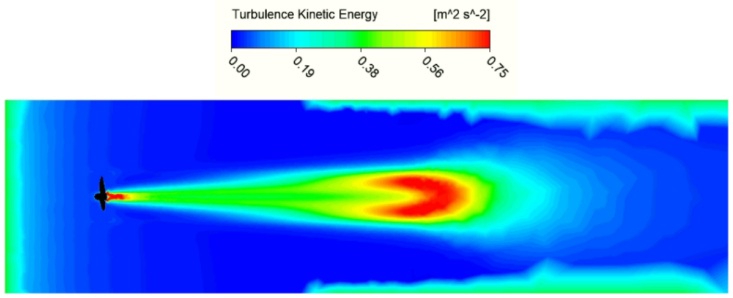

(c) 30° forward-swept turbine

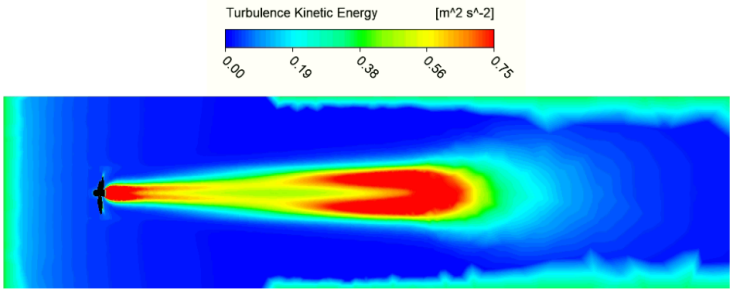

The transient simulations revealed distinct behaviors in the turbulent kinetic energy fields for the three rotor geometries. The 30° backward-swept configuration exhibited a noticeably narrower wake region, both in terms of magnitude and spatial extent of TKE. This trend is consistent with the turbulence intensity results, indicating a more stable and less turbulent wake. In contrast, the conventional and forward-swept turbines generated broader wakes with higher levels of localized turbulence.

However, a divergence between the qualitative and quantitative analyses of TKE was observed when assessing the instant peak values. The highest peak occurred in the conventional turbine case, while both swept-blade configurations presented lower and nearly identical maximum values, regardless of the sweep direction. This indicates that, although swept geometries contribute to a more coherent and less dispersed wake overall, localized turbulence bursts still tend to arise in the conventional configuration, resulting in higher peak TKE.

This finding highlights the distinction between localized maxima and global wake behavior. A single region of intense turbulence, often near the rotor or within a shear layer, can elevate the maximum TKE value without accurately reflecting the overall wake quality. Therefore, it is essential to complement peak value analyses with spatially averaged quantities or energy integrals for a more comprehensive characterization of wake dynamics.

3.9.3 Pressure and velocity recovery lengths

To refine the analysis of pressure and velocity recovery lengths previously evaluated under steady-state conditions (using a probe positioned at $10D$ downstream of the rotor), these quantities were also examined under transient conditions. Three axial lines were defined across the simulation domain, extending from the inlet to the outlet, at three different radial positions: $r = 0$, $r = 0.5R$, and $r = R$. Along these lines, velocity and pressure values were computed and plotted as a function of the distance along the global Y axis, aligned with the flow direction. Figure 3.30 illustrates the configuration used to extract pressure and velocity data.

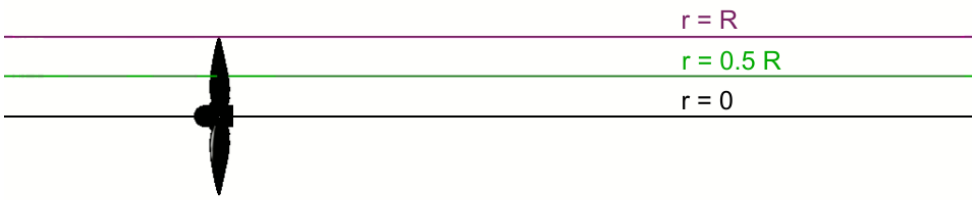

Figure 3.30 – Axial lines defined in the simulation domain for the evaluation of pressure and velocity recovery at three radial positions ($r = 0$, $r = 0.5R$, and $r = R$), extending from the inlet to the outlet of the domain.

To properly evaluate the development of pressure and velocity throughout the simulation domain, the variables were nondimensionalized using the inlet velocity as the velocity scale, the local atmospheric pressure (approximately 1020 hPa) as the reference pressure, and the rotor diameter as the characteristic length. This procedure allows the generalization of the CFD results, facilitates the identification of dominant effects on the flow, and enables

direct comparison with other CFD simulations and/or wind tunnel experiments, regardless of scale.

Regarding the velocity analysis, the axial component Y of the velocity in the stationary frame was computed along the axial lines in its dimensionless form using equation (3.20). The stationary frame variable ensures consistency throughout the domain, as it represents the velocity relative to a fixed reference. Consequently, the velocity profiles obtained correspond to the flow as observed from an external reference frame (analogous to laboratory conditions), which is the conventional approach for assessing recovery lengths.

$$\widetilde{U}_y(x) = \frac{U_y(x)}{U_\infty} \tag{3.20}$$

As seen in Figure 3.31, the 30° backward-swept blade model exhibited consistently higher axial velocities in the near and intermediate wake regions at all radial positions when compared to the straight and forward-swept geometries. This indicates a faster wake recovery for the backward-swept configuration, a favorable feature in terms of energy extraction and downstream flow stability.

Figure 3.31 – Velocity Recovery Length at Different Radial Positions

(a) $r = 0$

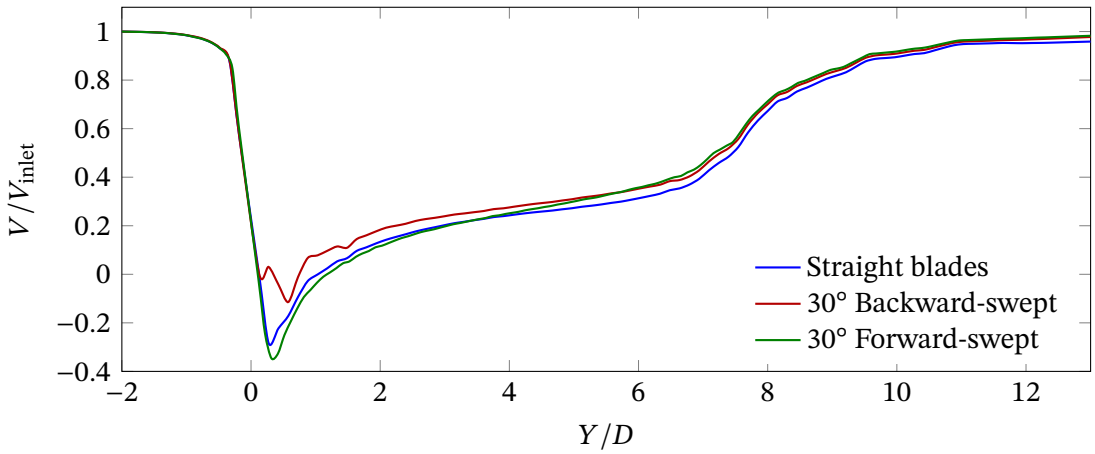

(b) $r = 0.5R$

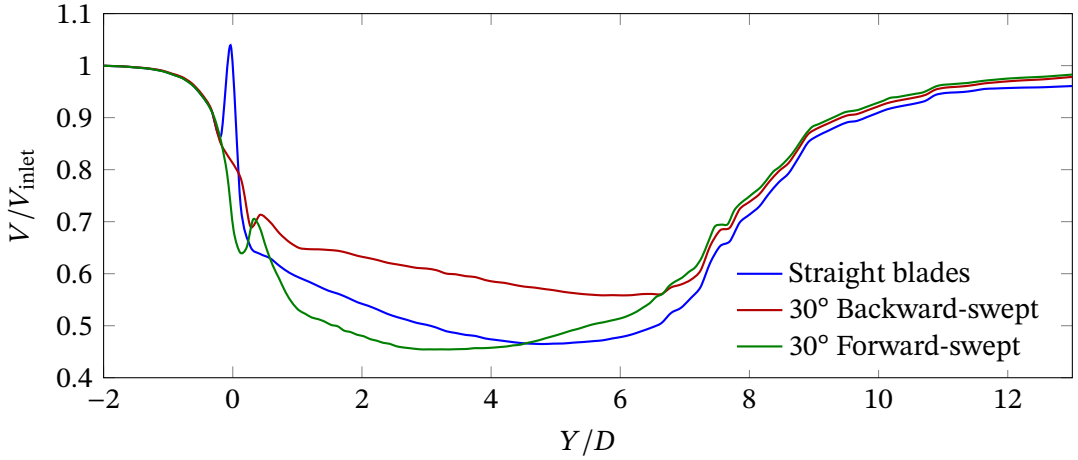

(c) $r = R$

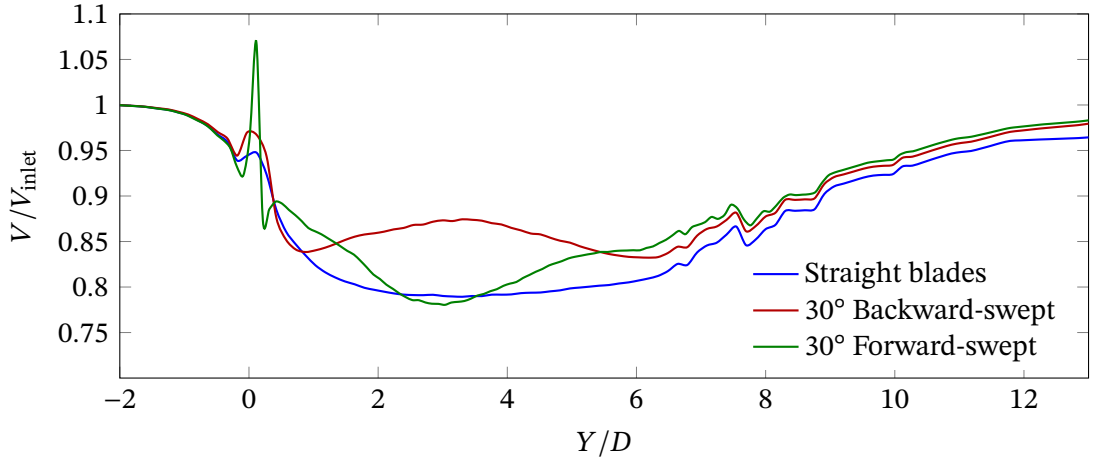

At the rotor axis (i.e. $r = 0$), as illustrated in figure 3.31a, the velocity drops signifi-

cantly just behind the rotor for all geometries, even reaching negative values, an indication of localized flow reversal or strong recirculation, likely associated with tip and hub vortex dynamics. The backward-swept model, in contrast, showed milder flow separation, with velocities remaining mostly within the positive range.

At $r = 0.5R$, depicted in figure 3.31b, the straight-bladed model exhibited a local velocity overshoot (greater than the inlet velocity) immediately upstream of the rotor, which may be attributed to flow acceleration due to blockage effects or flow channeling near the blade tip. A similar phenomenon was observed at $r = R$ for the 30° forward-swept model, as seen in figure 3.31c. Once again, the backward-swept configuration presented a smoother and more gradual velocity decay and recovery.

Across all three geometries, the velocity magnitude returned to values close to the inlet condition beyond $10D$ downstream of the rotor, confirming that wake effects are largely dissipated at this distance in the far wake. Nevertheless, the 30° backward-swept model consistently showed less pronounced flow deceleration at all radial positions analyzed, suggesting reduced energy losses in the wake and improved downstream flow conditions.

When it comes to pressure recovery, the local static pressure of the flow was calculated over the axial lines for the three radial positions and then divided by the atmosprheric pressure in Brasília, DF, to achieve a dimensionless pressure value.

The pressure profiles obtained this way , presented in figure 3.32, showed the expected trends consistent with BEM theory and Bernoulli's principle: as the flow approaches the rotor, pressure increases due to flow deceleration, followed by a sharp drop upon crossing the rotor plane, which represents energy extraction.

Figure 3.32 – Pressure Recovery Length at Different Radial Positions

(a) $r = 0$

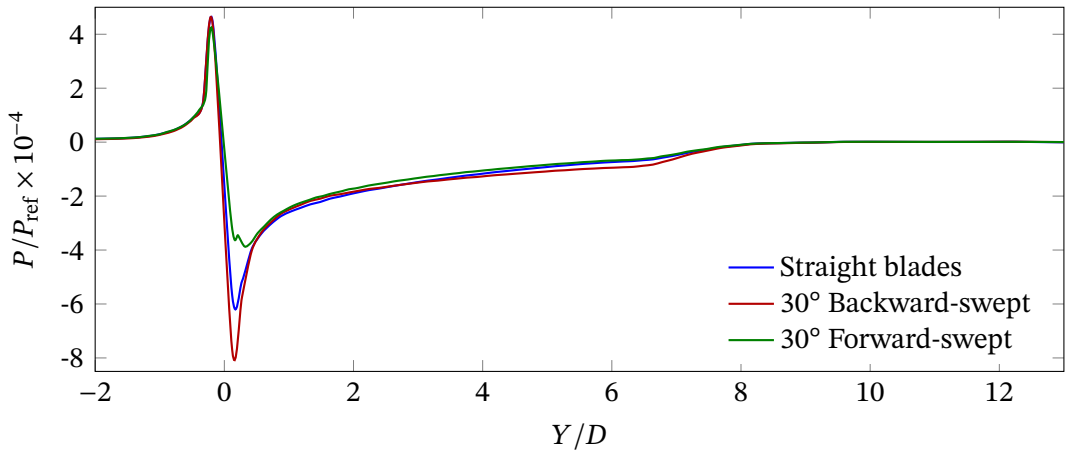

(b) $r = 0.5R$

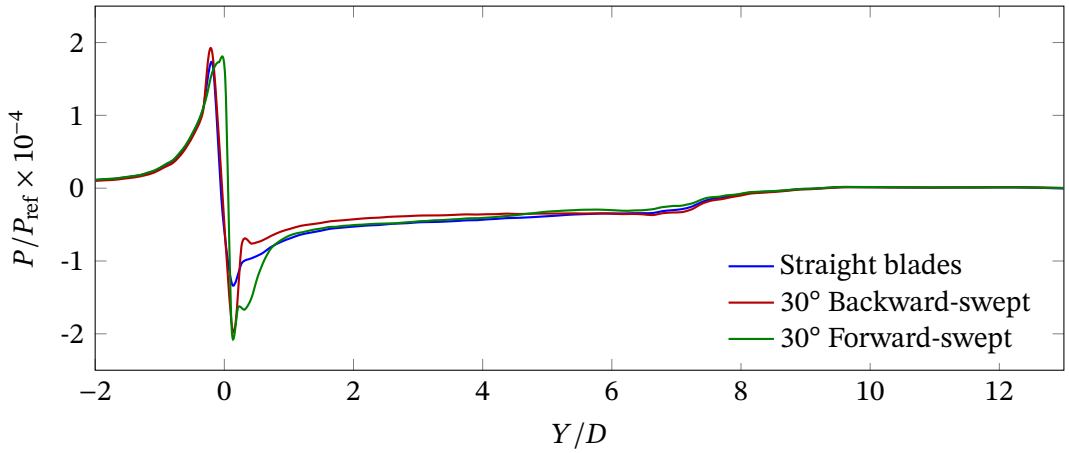

(c) $r = R$

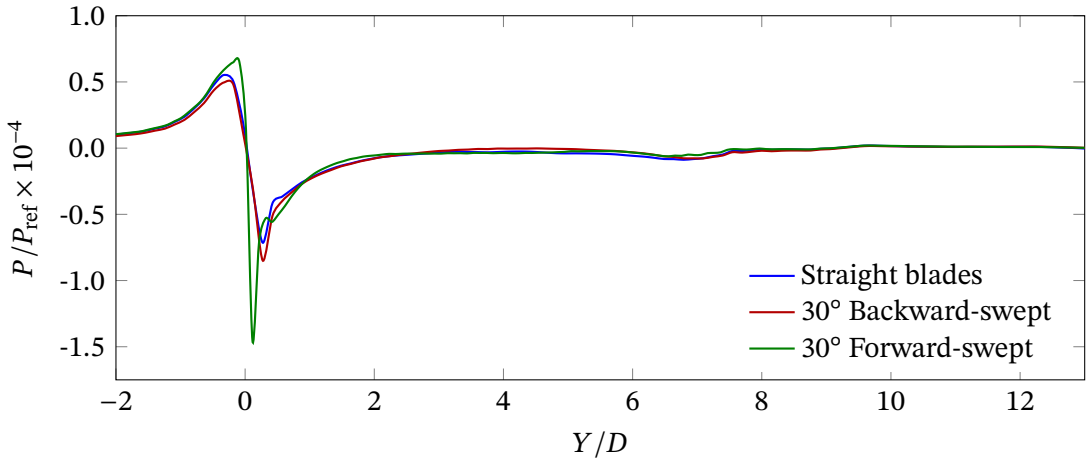

At $r = 0$, the 30 ° backward-swept model showed the largest pressure drop, indicating

a more effective energy conversion near the center of the rotor, as can be seen in figure 3.32a. In contrast, the 30° forward-swept configuration generated the smallest pressure deficit at this location. At the intermediate radial position $r = 0.5R$, illustrated in figure 3.32b, both swept models displayed similar pressure drops, slightly larger than the straight-bladed case. In addition, the 30° backward-swept model demonstrated faster pressure recovery compared with the other geometries. Finally, at $r = R$, the 30° forward-swept blade produced the most pronounced pressure deficit, suggesting that its geometry may cause more aggressive flow turning and extraction near the tip region, as depicted in figure 3.32c.

Despite these local variations, all three geometries exhibited similar recovery rates, reaching a pressure plateau around $Y/D \approx 10$, with minor residual discrepancies beyond this point. This reinforces that the wake stabilizes at roughly the same downstream distance, regardless of sweep angle, although the magnitude and the spatial distribution of the extracted energy vary between configurations.

Furthermore, the total pressure in the stationary frame was assessed, defined as the sum of static and dynamic pressures ($p + \frac{1}{2}\rho U^2$) in a fixed reference frame, with the objective of evaluating energy losses in the flow. Drops in total pressure across rotors and within turbulent wakes are directly associated with irreversible energy losses, such as turbulence generation, viscous dissipation, and wake mixing. Therefore, monitoring its recovery downstream of the rotor provides a valuable metric for evaluating overall aerodynamic performance and the fluid degradation induced by different rotor designs, offering a comprehensive measure of the total mechanical energy in the flow.

As shown in figure 3.33, which shows the dimensionless total pressure evolution over the axial lines at the three different radial positions, all geometries yielded a pronounced drop in total pressure as the flow crosses the rotor and, subsequently, a gradual recovery is observed until the stabilization of the wake is observed at around $Y/D = 12$.

As illustrated in figure 3.33, which presents the dimensionless total pressure evolution along the axial lines at three radial positions, all geometries exhibited a pronounced drop in total pressure as the flow passed through the rotor, followed by a gradual recovery, with wake stabilization occurring at approximately $Y/D \approx 12$.

At $r = 0$, as shown in figure 3.33a, all three configurations exhibited curves with similar overall trends throughout the domain. The main difference lies in the pressure deficit immediately before and just after the rotor, which was considerably more pronounced for the 30° backward-swept blades, followed by the conventional model and, lastly, the 30° forward-swept blades. This suggests more localized energy conversion at this position for the backward-swept configuration.

At $r = 0.5R$, illustrated in figure 3.33b, the pressure deficit across the rotor was smaller for the 30° backward-swept blades. However, in the near and intermediate wake regions ($0 < Y/D < 6$), this configuration consistently maintained higher total pressure levels

Figure 3.33 – Total Pressure Recovery Length at Different Radial Positions

(a) $r = 0$

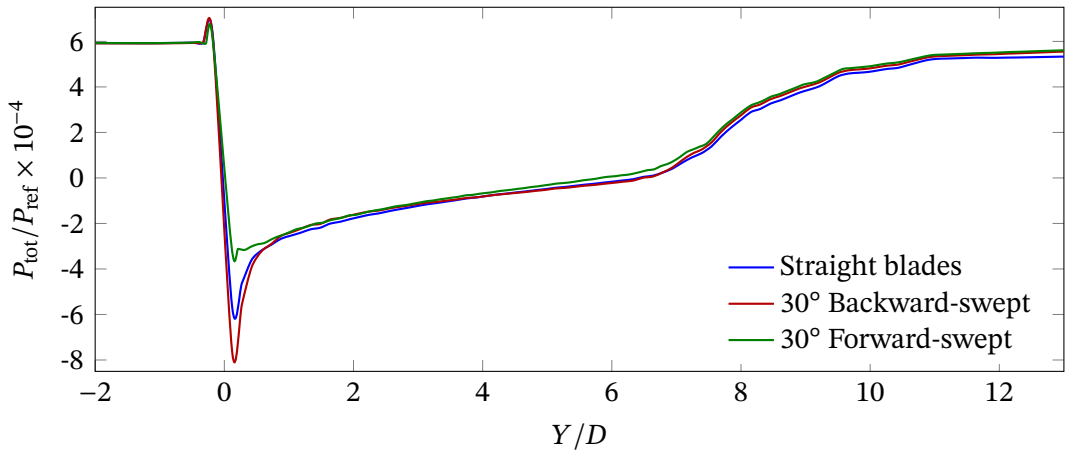

(b) $r = 0.5R$

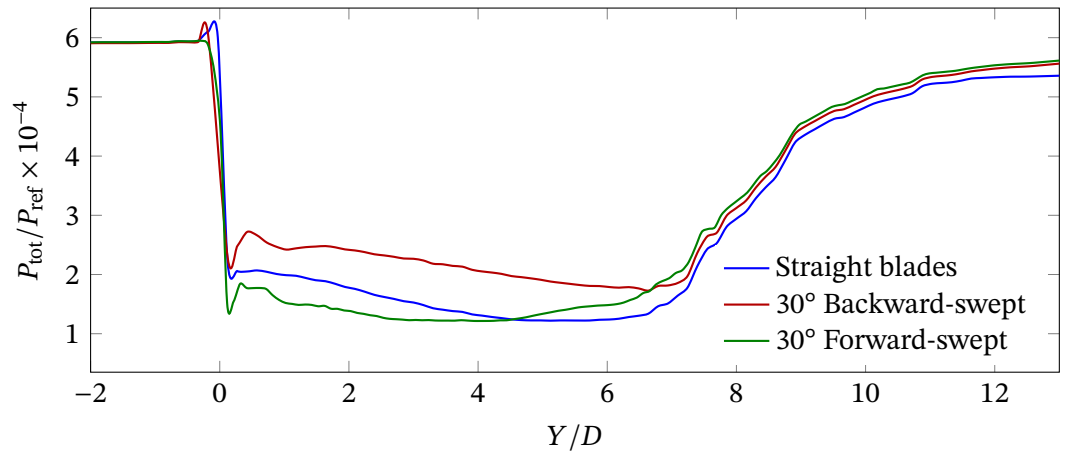

(c) $r = R$

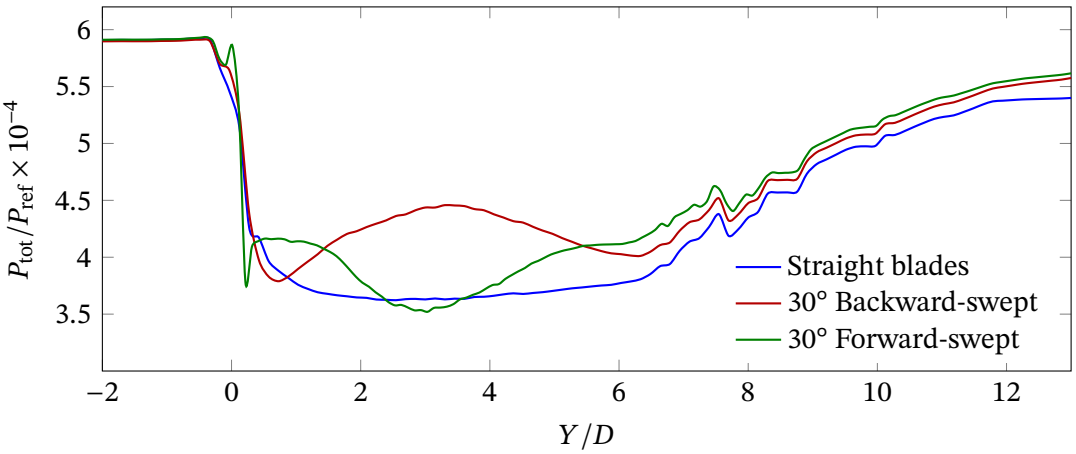

compared to the straight and forward-swept models. A similar effect is observed at $r = R$,

reinforcing the indication that the backward sweep induces lower energy losses in the wake and promotes a more efficient aerodynamic interaction with the flow.

Moreover, the higher total pressure levels observed for the 30° backward-swept blades are consistent with the nondimensional velocity analysis U_y/U_∞, in which this configuration also exhibited higher velocity values within the near and intermediate wake regions. These results provide strong evidence that wake recovery in those regions is more efficient for the backward-swept blades. In the far wake ($Y/D > 8$), however, the influence of blade geometry becomes negligible, suggesting that external flow mixing governs the recovery process.

4 Conclusions

This study investigated the energy efficiency of hydrokinetic turbines equipped with swept blades - considering both forward and backward sweep configurations - through CFD simulations, based on a geometry previously validated in wind tunnel experiments, as proposed by Mendes (2015). A mesh sensitivity analysis was conducted, and the k–ω SST turbulence model was employed. Simulations were performed for both the conventional straight-bladed turbine and the curved-blade models, generated according to the methodology proposed by Gemaque, Vaz, and Saavedra (2022). The specific objectives established for this work were successfully accomplished, as summarized below.

Initially, turbine geometries with sweep angles of 10°, 20°, and 30°, in both forward and backward orientations were modeled. CFD simulations were performed under consistent boundary and flow conditions to evaluate the global performance of each configuration through the power coefficient C_P as a function of the tip-speed ratio λ. The simulation setup consisted of a $10 m/s$ inlet flow (air at standard conditions), zero relative pressure at the outlet and lateral boundaries (unconfined flow), and no-slip condition at the turbine surface.

Each model underwent multiple steady-state simulations, and additional transient simulations were performed for the conventional, 30° backward-swept, and 30° forward-swept turbines at the angular velocity corresponding to their respective peak C_P values. The maximum power coefficient under steady-state conditions decreased from 0.349 for the straight-bladed turbine to 0.324 for the 30° backward-swept model and 0.324 for the 30° forward-swept model, corresponding to an approximate reduction of 7%. In the transient regime, at the same tip-speed ratio, the straight-bladed model reached a C_P of 0.355, while the 30° backward- and forward-swept configurations achieved only 0.323 and 0.327, respectively. The reduction in performance therefore ranged between 8% and 9%.

All swept-blade configurations yielded lower C_P values compared to the straight-bladed reference, contradicting trends predicted by the modified BEM theory. Nevertheless, the backward-swept models exhibited improved flow characteristics, including reduced turbulence intensity and turbulent kinetic energy, diminished boundary layer separation, smoother pressure distributions, and lower flow deficit.

The analysis of radial leakage through the lateral surface of the rotating domain proved essential to understanding the divergence between torque-based and control-volume-based evaluations of C_P. Backward-swept blades consistently reduced radial outflow, preserving an essentially axial induction pattern and yielding excellent agreement between the two calculation methods. In contrast, forward-swept geometries intensified radial transport, reducing the mass flux effectively engaged in energy extraction and artificially increasing the pressure drop used in the integral evaluation.

This behavior is consistent with the induction physics: increased radial motion decreases axial induction a and distorts the wake, while backward sweep enhances flow coherence. Altogether, the radial-flow analysis reinforces the conclusion that backward sweep improves flow stability and reduces 3D losses, whereas forward-sweep amplifies them.

With regard to flow separation, the analysis based on wall shear vectors and velocity streamlines confirmed that backward-swept blades promote more favorable near-wall flow structures, mitigating boundary layer detachment. Conversely, forward-swept configurations showed more intense flow separation and increased wake turbulence. Although sweep angle had limited influence on pressure and velocity recovery lengths at $10D$ downstream, their effect on near-wake dynamics was evident.

The transient simulations revealed more meaningful differences in the wake behavior. The 30° backward-swept configuration showed a significant reduction in turbulence intensity and turbulent kinetic energy in the near and intermediate wake regions, along with improved velocity and pressure recovery. These findings suggest that this geometry may provide advantages in the spacing of the turbines for the arrays, contributing to better downstream flow conditions without significantly compromising individual efficiency. The results reinforce the consistency between steady and unsteady simulations and demonstrate the value of transient analysis for evaluating flow dynamics that are otherwise hidden in steady-state approximations.

The current state of the art shows a notable gap in systematic studies addressing the effects of swept blades in hydrokinetic turbines. Most existing works focus on wind turbines, often employing distinct modeling strategies, sweep definitions, and flow conditions under idealized or wind-specific assumptions. This lack of standardization hinders the comparison of results and constrains the formulation of generalized design guidelines for hydrokinetic applications. By employing a consistent CFD methodology and analyzing both forward and backward sweep configurations on a validated hydrokinetic geometry, this work contributes novel insights within a hydrodynamic context.

Despite the valuable contributions, the present study has certain limitations. Transient simulations were conducted only for selected configurations (those with the largest differences in C_P relative to the reference turbine) and solely at their optimal λ values. The analysis focused primarily on steady-state flow behavior and did not consider structural loading or unsteady flow phenomena.

To address these limitations and build upon the findings, the following directions are recommended for future research:

- Perform transient CFD simulations for all configurations and across a broader range of λ values to capture dynamic effects and flow instabilities;
- Manufacture turbine models for experimental validation in a wind tunnel under

controlled laboratory conditions;

- Evaluate structural responses to aerodynamic loads induced by sweep angles;
- Investigate the effects of blade sweep in turbine arrays, including wake interactions and layout optimization strategies.

Finally, a noteworthy contribution of this work is the systematic mesh convergence study, which demonstrated that accurate and physically meaningful results can be obtained using a computationally efficient mesh configuration. This approach can be replicated in future simulations and may serve as a reference for numerical studies focused on blade optimization in hydrokinetic turbines.

References

ANDREWS, G. E. The geometric series in calculus. **The American mathematical monthly**, Taylor & Francis, v. 105, n. 1, p. 36–40, 1998. Cit. on p. 46.

ANSYS Inc. **ANSYS Meshing User's Guide**. Canonsburg, PA, 2023. Version 2023 R1. Cit. on p. 52.

BATCHELOR, G. K. **An introduction to fluid dynamics**. Cambridge university press, 2000. Cit. on p. 81.

CALVIN, K.; DASGUPTA, D.; KRINNER, G.; MUKHERJI, A. Ipcc climate change synthesis report, "sixth assessment report". Jul. 2023. Cit. on p. 17.

CENGEL, Y.; CIMBALA, J. **Ebook: Fluid mechanics fundamentals and applications (si units)**. McGraw Hill, 2013. Cit. on pp. 29 and 46.

ELS, R. H. van; MIRANDA, A.; JUNIOR, A.; ECHEVERRY, S. Hydrokinetic energy conversion-state of the art and perspectives in brazil. *In*: **SDEWES-1st Latin American Conference on Sustainable Development of Energy, Water and Environmental systems**. 2018. Cit. on p. 26.

Empresa de Pesquisa Energética (EPE). **Síntese do Balanço Energético Nacional 2025**. Brasília, DF, 2025. Balanço Energético Nacional – BEN. Cit. on p. 26.

GEMAQUE, M. L. A.; VAZ, J. R. P.; SAAVEDRA, O. R. Optimization of Hydrokinetic Swept Blades. **Sustainability**, v. 14, n. 21, p. 13968, Oct. 2022. ISSN 2071-1050. Available at: https://www.mdpi.com/2071-1050/14/21/13968. Cit. on pp. 36, 37, 38, 40, 53, 59, 62, 67, 68, 71, and 105.

HANSEN, M. O. L. **Aerodynamics of wind turbines**. 2nd ed. ed. London ; Sterling, VA: Earthscan, 2008. OCLC: ocm86172940. ISBN 978-1-84407-438-9. Cit. on pp. 27, 28, and 89.

HEPA. Health and energy platform of action report 2020-2022: building connections for better health. Geneva, 2024. Available at: https://www.who.int/publications/i/item/9789240071650. Cit. on p. 18.

IEA. World energy statistics and balances. Paris, 2024. Available at: https://www.iea.org/data-and-statistics/data-product/world-energy-statistics-and-balances. Cit. on pp. 19, 20, 21, 22, 23, and 24.

International Hydropower Association. **International Hydropower Association**. 2024. https://www.hydropower.org/. Accessed: 2024-06-11. Cit. on p. 25.

IRENA. Irena world energy transitions outlook 2023: 1.5°c pathway. Abu Dhabi, 2023. Available at: https://www.irena.org/publications. Cit. on pp. 18 and 22.

JUNIOR, A. C. P. B.; MENDES, R. C. F.; WIRRIG, T.; NOGUERA, R.; OLIVEIRA, T. F. On the design of propeller hydrokinetic turbines: the effect of the number of blades. **Journal of the Brazilian Society of Mechanical Sciences and Engineering**, v. 41, n. 6, p. 253, Jun. 2019. ISSN 1678-5878, 1806-3691. Available at: http://link.springer.com/10.1007/s40430-019-1753-4. Cit. on pp. 41, 43, 54, and 55.

KAYA, M. N.; KOSE, F.; INGHAM, D.; MA, L.; POURKASHANIAN, M. Aerodynamic performance of a horizontal axis wind turbine with forward and backward swept blades. **Journal of Wind Engineering and Industrial Aerodynamics**, v. 176, p. 166–173, May 2018. ISSN 01676105. Available at: https://linkinghub.elsevier.com/retrieve/pii/S0167610517309753. Cit. on p. 30.

KLEIN, A. C.; BARTHOLOMAY, S.; MARTEN, D.; LUTZ, T.; PECHLIVANOGLOU, G.; NAYERI, C. N.; PASCHEREIT, C. O.; KRäMER, E. About the suitability of different numerical methods to reproduce model wind turbine measurements in a wind tunnel with a high blockage ratio. **Wind Energy Science**, v. 3, n. 1, p. 439–460, Jun. 2018. ISSN 2366-7451. Available at: https://wes.copernicus.org/articles/3/439/2018/. Cit. on p. 58.

LARWOOD, S.; DAM, C. V.; SCHOW, D. Design studies of swept wind turbine blades. **Renewable Energy**, v. 71, p. 563–571, Nov. 2014. ISSN 09601481. Available at: https://linkinghub.elsevier.com/retrieve/pii/S0960148114003115. Cit. on pp. 29 and 30.

LIU, S.; ZHANG, J.; SUN, K.; GUO, Y.; GUAN, D. Influence of Swept Blades on the Performance and Hydrodynamic Characteristics of a Bidirectional Horizontal-Axis Tidal Turbine. **Journal of Marine Science and Engineering**, v. 10, n. 3, p. 365, Mar. 2022. ISSN 2077-1312. Number: 3 Publisher: Multidisciplinary Digital Publishing Institute. Available at: https://www.mdpi.com/2077-1312/10/3/365. Cit. on pp. 33 and 34.

MENDES, R. C. F. **Estudo do fator de indução axial em turbinas de eixo horizontal**. Dissertation (Master of Science) — Universidade de Brasília, Brasília, Jul. 2015. Available at: http://repositorio.unb.br/handle/10482/19902. Cit. on pp. 38 and 105.

MME-EPE. Plano decenal de expansão de energia 2031. Brasília, 2022. Available at: https://www.mme.gov.br. Cit. on pp. 24, 25, and 26.

NIEBUHR, C. M.; DIJK, M. V.; NEARY, V. S.; BHAGWAN, J. N. A review of hydrokinetic turbines and enhancement techniques for canal installations: Technology, applicability and potential. **Renewable and Sustainable Energy Reviews**, Elsevier, v. 113, p. 109240, 2019. Cit. on pp. 25 and 27.

Operador Nacional do Sistema Elétrico. **Operador Nacional do Sistema Elétrico (ONS)**. 2025. https://www.ons.org.br/. Acesso em: 25 jan. 2025. Cit. on p. 26.

SCHLICHTING, H.; GERSTEN, K. **Boundary-layer theory**. springer, 2016. Cit. on pp. 45, 46, 54, and 81.

SESSAREGO, M.; FENG, J.; RAMOS-GARCÍA, N.; HORCAS, S. G. Design optimization of a curved wind turbine blade using neural networks and an aero-elastic vortex method under turbulent inflow. **Renewable Energy**, Elsevier, v. 146, p. 1524–1535, 2020. Cit. on p. 36.

SILVEIRA-NETO, A. Escoamentos turbulentos: análise física e modelagem teórica. **Composer, Uberlândia**, 2020. Cit. on p. 29.

SOUZA, T. V. D.; OLIVEIRA, T.; MENDES, R. C. F. Numerical Study on the Impact of Blade Sweep Angles in Hydrokinetic Turbine Efficiency. *In*: **Proceedings of the XII Congresso Nacional de Engenharia Mecânica - CONEM 2024**. ABCM, 2024. Available at: http://abcm.org.br/anais-de-eventos/CON24/0512. Cit. on pp. 38, 39, and 53.

SOUZA, T. V. de; OLIVEIRA, T. F. de; MENDES, R. C. F. ENC-2024-0587 COMPARATIVE ANALYSIS OF BACKWARD AND FORWARD SWEPT BLADES FOR HIDROKINETIC TURBINES: A NUMERICAL STUDY. 2024. Cit. on pp. 38, 39, and 53.

VAZ, D. A. do R.; VAZ, J. R.; SILVA, P. A. An approach for the optimization of diffuser-augmented hydrokinetic blades free of cavitation. **Energy for Sustainable Development**, Elsevier, v. 45, p. 142–149, 2018. Cit. on p. 67.

WANG, T.; YU, H.; XIANG, R.; CHEN, X.; ZHANG, X. Performance and unsteady flow characteristic of forward-curved impeller with different blade inlet swept angles in a pump as turbine. **Energy**, v. 282, p. 128890, Nov. 2023. ISSN 03605442. Available at: https://linkinghub.elsevier.com/retrieve/pii/S0360544223022843. Cit. on pp. 35 and 36.

WHITE, F. M. *et al.* **Fluid mechanics**. McGraw-hill New York, 2011. Cit. on pp. 29 and 81.

WILCOX, D. C. *et al.* **Turbulence modeling for CFD**. DCW industries La Canada, CA, 1998. v. 2. Cit. on p. 29.

WIśNIEWSKI, J.; ROGOWSKI, K.; GUMOWSKI, K.; SZUMBARSKI, J. Wind tunnel comparison of four VAWT configurations to test load-limiting concept and CFD validation. **Wind Energy Science**, v. 6, n. 1, p. 287–294, Feb. 2021. ISSN 2366-7451. Available at: https://wes.copernicus.org/articles/6/287/2021/. Cit. on p. 59.

WRI. World greenhouse gas emissions: 2020. 2023. Available at: https://www.wri.org/data/world-greenhouse-gas-emissions-2020?_gl=1*qjl1v8*_up*MQ..&gclid=Cj0KCQjw1Yy5BhD-ARIsAI0RbXZ-3pj5A7xReqP0PKD_XINDRK3Zh_60ive8qCaeZ5uS59gn-grO-toaAl3XEALw_wcB. Cit. on p. 17.

ZHENG, Y.; YANG, W.; WEI, K.; CHEN, Y.; ZOU, H. Enhancing Efficiency and Reliability of Tidal Stream Energy Conversion through Swept-Blade Design. **Energies**, v. 17, n. 2, p. 334, Jan. 2024. ISSN 1996-1073. Available at: https://www.mdpi.com/1996-1073/17/2/334. Cit. on pp. 34 and 35.

ZUO, H. M.; LIU, C.; YANG, H.; WANG, F. Numerical Study on the Effect of Swept Blade on the Aerodynamic Performance of Wind Turbine at High Tip Speed Ratio. **Journal of Physics: Conference Series**, v. 753, p. 102010, Sep. 2016. ISSN 1742-6588, 1742-6596. Available at: https://iopscience.iop.org/article/10.1088/1742-6596/753/10/102010. Cit. on pp. 31, 32, and 33.

Appendices

Appendix A – Pressure contour plots

In this appendix, the contour plots of pressure distribution on the turbine surfaces, obtained under steady-state conditions, are presented for all geometries analyzed in the present work. The pressure field provides direct insight into the aerodynamic loads acting on the blades and allows the identification of regions of high or low pressure that may be associated with lift generation, drag forces, or flow separation. By comparing the pressure contours across different sweep configurations, it is possible to visualize the aerodynamic effects of blade curvature and complement the quantitative analyses discussed in chapter 3. These plots provide additional evidence of how geometric variations influence local flow characteristics and the overall performance of the turbine models.

Figure A.1 – Pressure distribution on the surface of the straight-bladed turbine model.

(a) Pressure side (b) Suction side

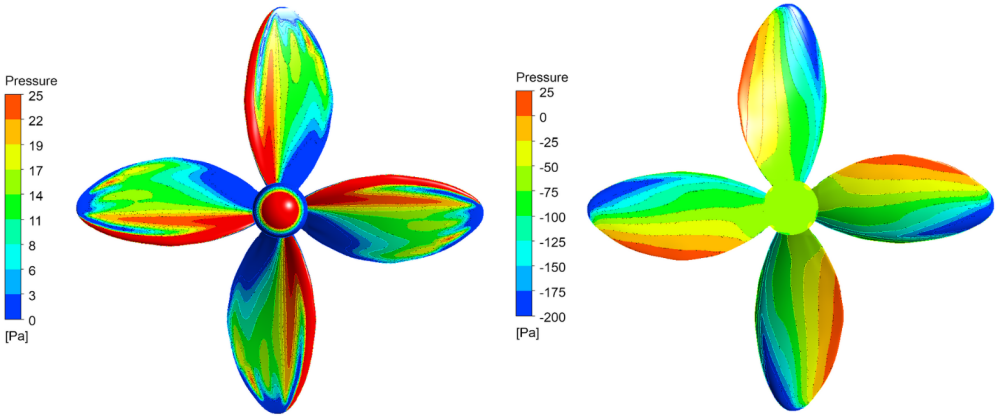

Figure A.2 – Pressure distribution on the surface of the 10° backward-swept blades turbine model.

(a) Pressure side (b) Suction side

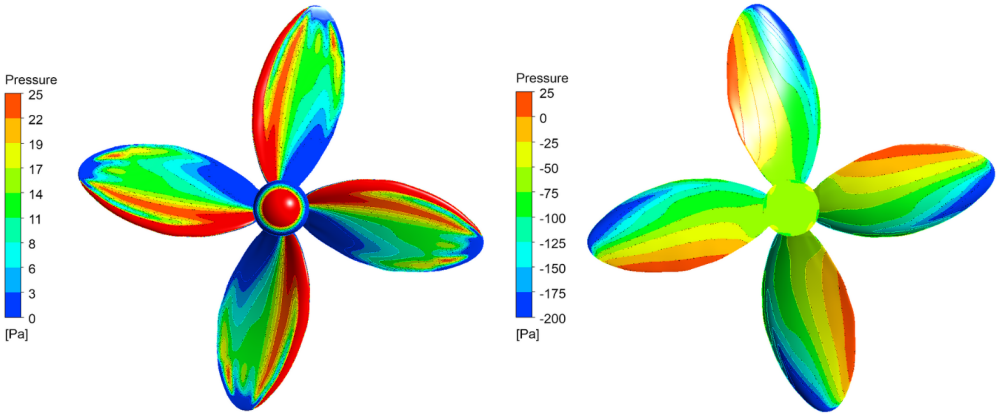

Figure A.3 – Pressure distribution on the surface of the 20° backward-swept blades turbine model.

(a) Pressure side (b) Suction side

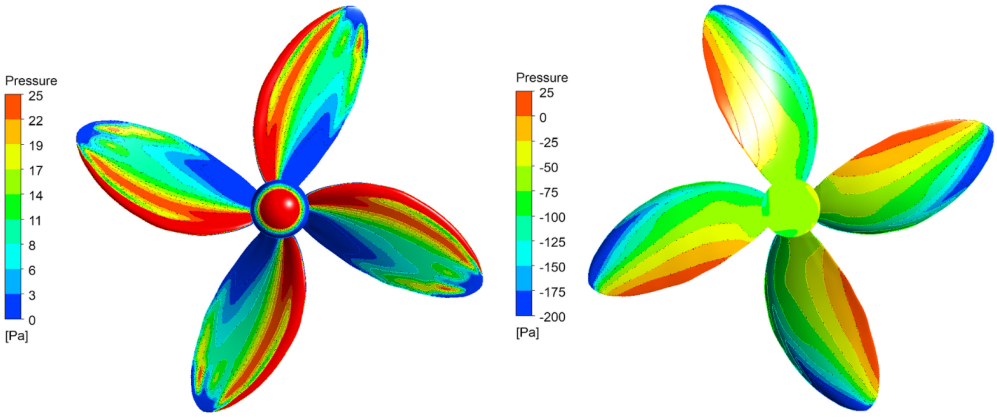

Figure A.4 – Pressure distribution on the surface of the 30° backward-swept blades turbine model.

(a) Pressure side (b) Suction side

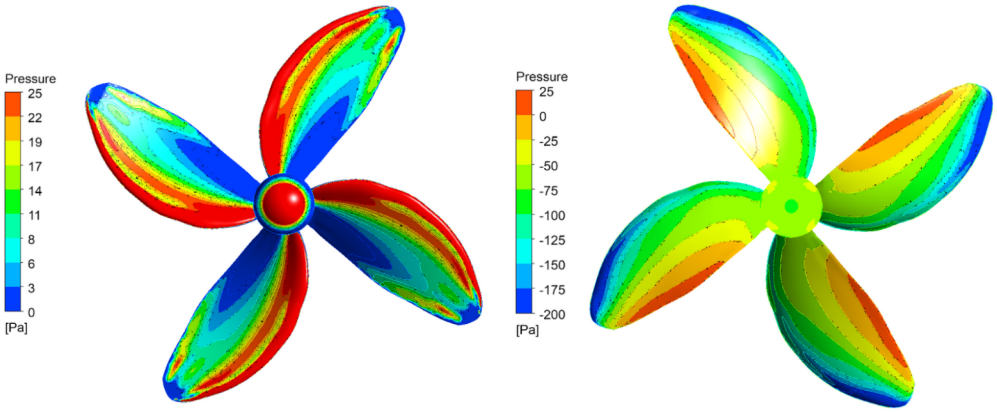

Figure A.5 – Pressure distribution on the surface of the 10° forward-swept blades turbine model.

(a) Pressure side (b) Suction side

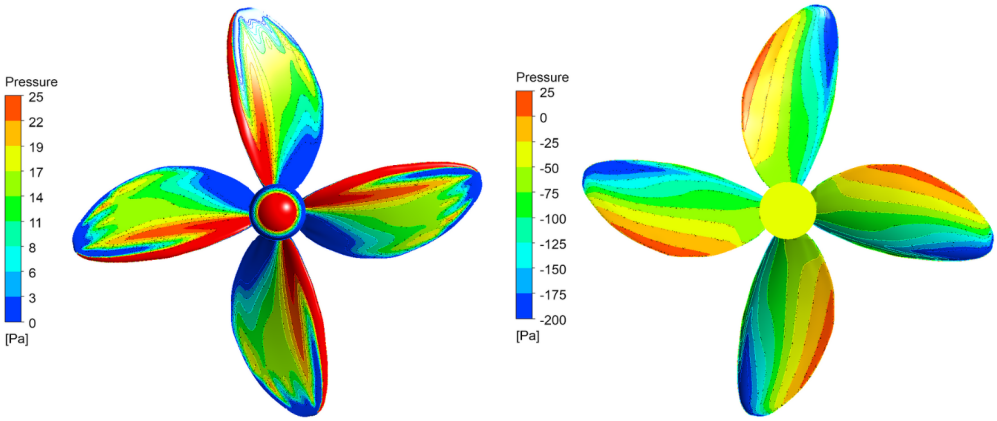

Figure A.6 – Pressure distribution on the surface of the 20° forward-swept blades turbine model.

(a) Pressure side (b) Suction side

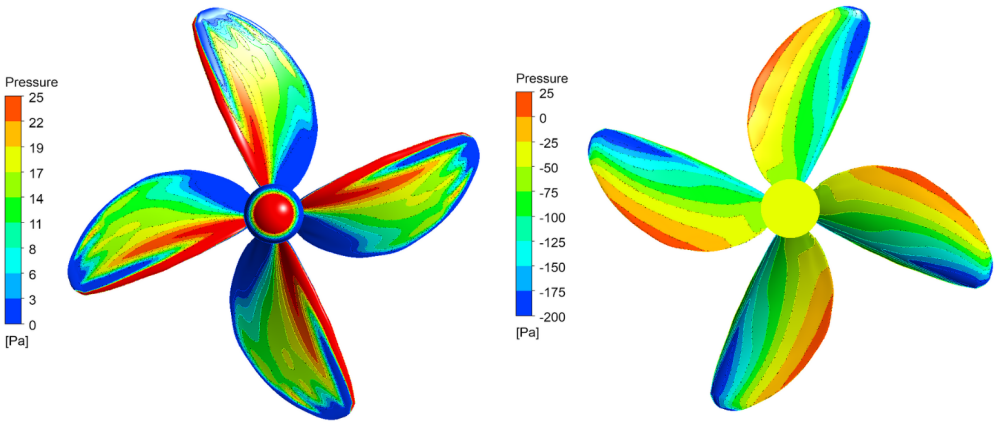

Figure A.7 – Pressure distribution on the surface of the 30° forward-swept blades turbine model.

(a) Pressure side (b) Suction side

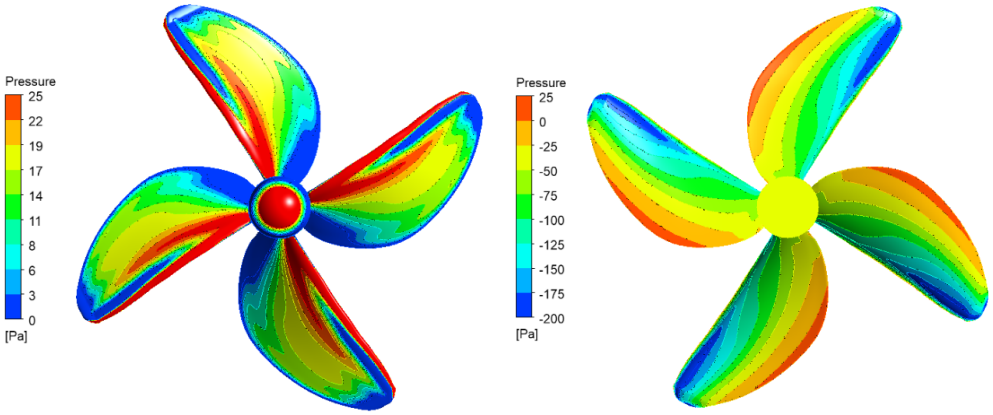

Appendix B – Turbulence intensity and turbulent kinetic energy fields

This appendix presents the turbulence intensity and turbulent kinetic energy (TKE) fields, obtained under steady-state conditions, for all geometries analyzed in this work. These quantities provide valuable insights into flow stability and the manner in which the energy extracted by the rotor is dissipated in the wake. The comparative analysis of different blade sweep configurations allows the identification of regions of greater instability and flow fluctuations, offering relevant information about wake coherence and the hydrodynamic impact of each model. The plots compiled here complement the results discussed in chapter 3, providing a broader perspective on the influence of blade geometry on the turbulent flow field.

B.1 Turbulence intensity

Figure B.1 – Turbulence intensity field downstream of the straight-bladed turbine rotor.

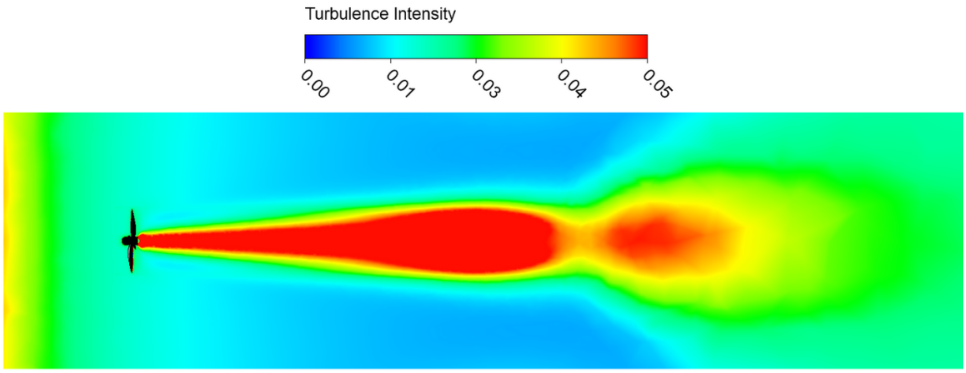

Figure B.2 – Turbulence intensity field downstream of the 10° backward-swept blade turbine rotor.

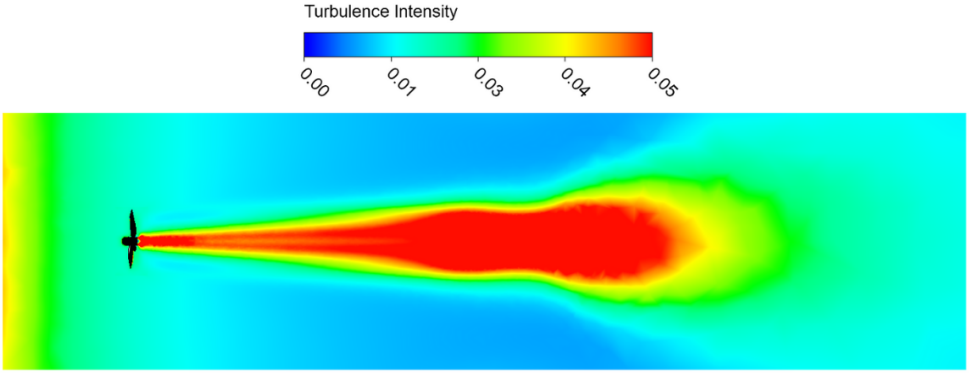

Figure B.3 – Turbulence intensity field downstream of the 20° backward-swept blade turbine rotor.

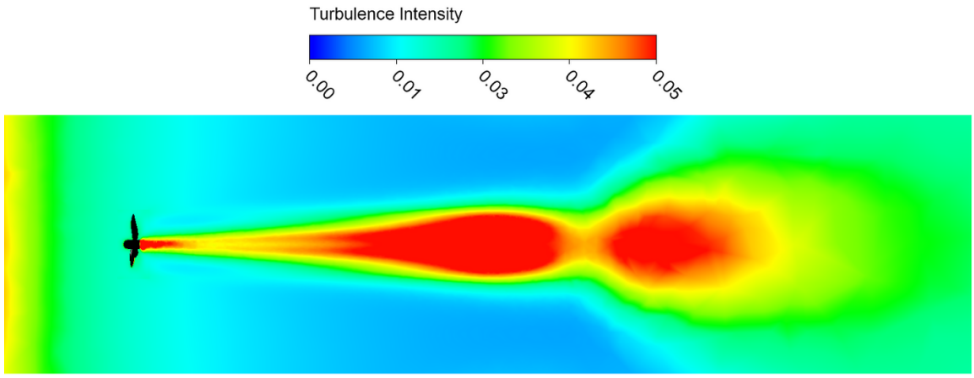

Figure B.4 – Turbulence intensity field downstream of the 30° backward-swept blade turbine rotor.

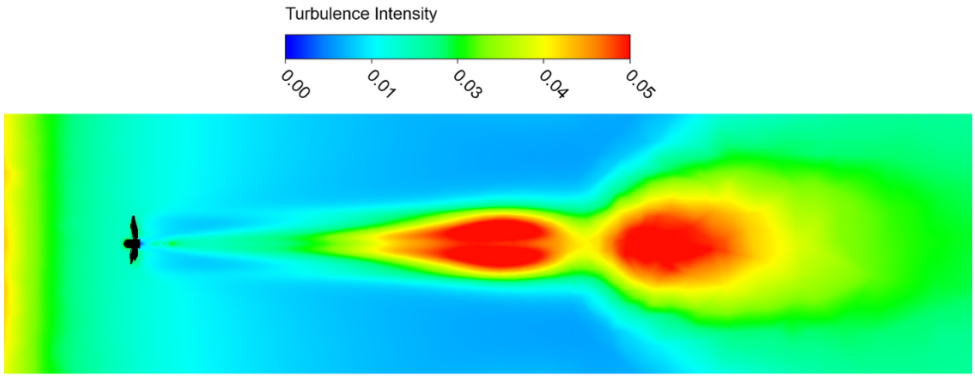

Figure B.5 – Turbulence intensity field downstream of the 10° forward-swept blade turbine rotor.

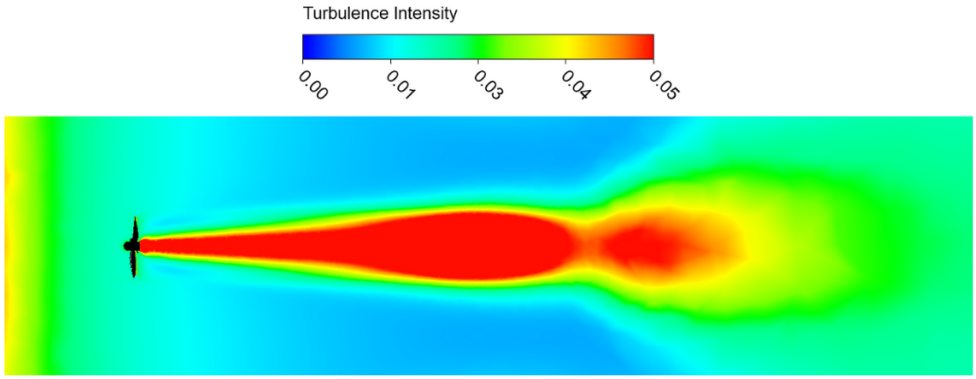

Figure B.6 – Turbulence intensity field downstream of the 20° forward-swept blade turbine rotor.

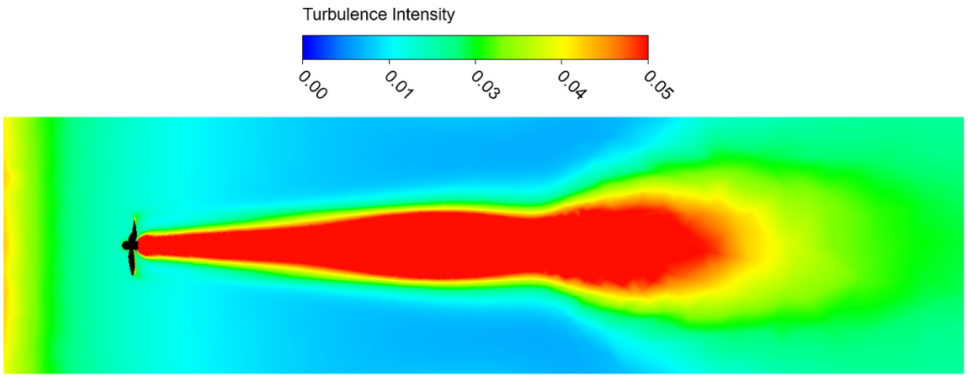

Figure B.7 – Turbulence intensity field downstream of the 30° forward-swept blade turbine rotor.

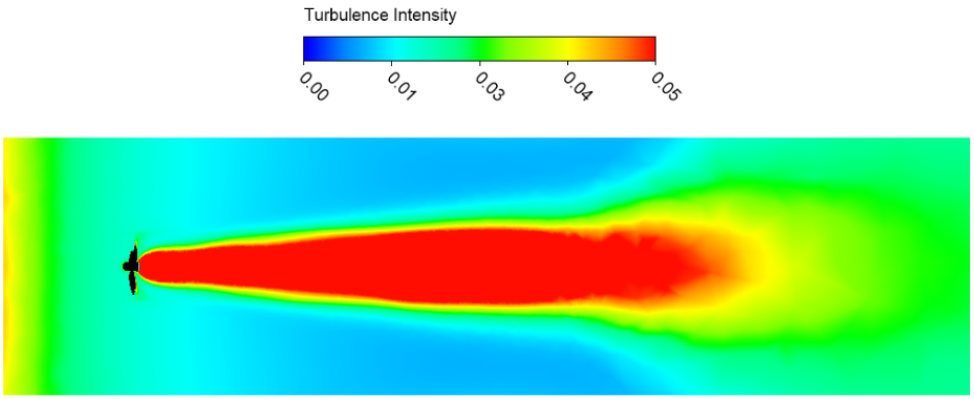

B.2 Turbulent kinetic energy (TKE)

Figure B.8 – Turbulent kinetic energy field downstream of the straight-bladed turbine rotor.

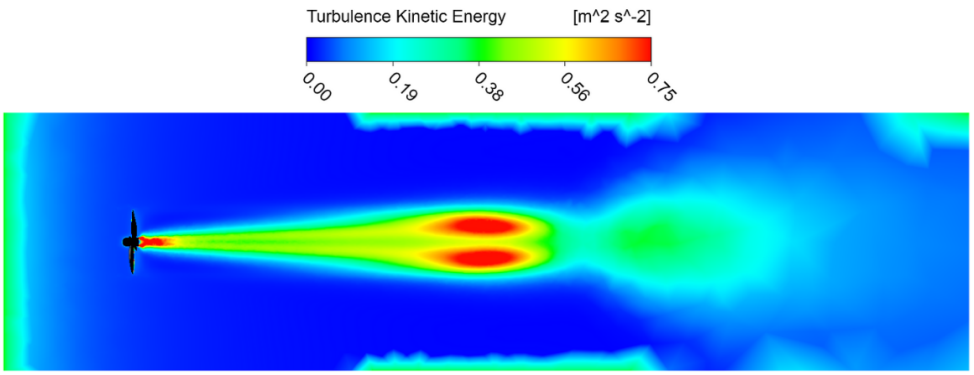

Figure B.9 – Turbulent kinetic energy field downstream of the 10° backward-swept blade turbine rotor.

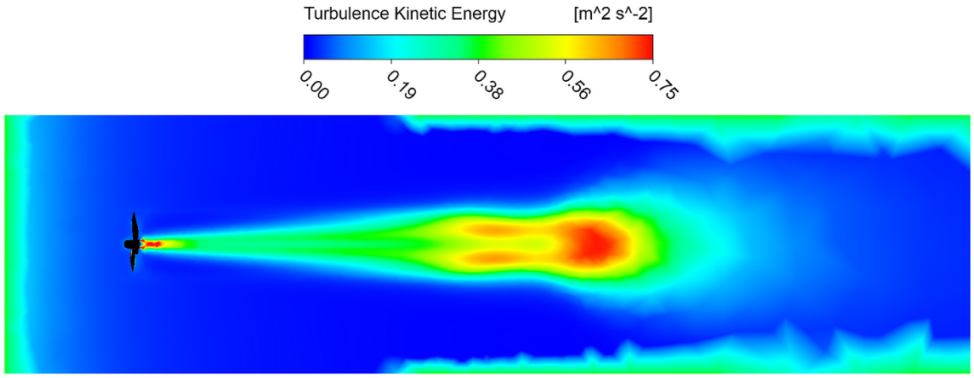

Figure B.10 – Turbulent kinetic energy field downstream of the 20° backward-swept blade turbine rotor.

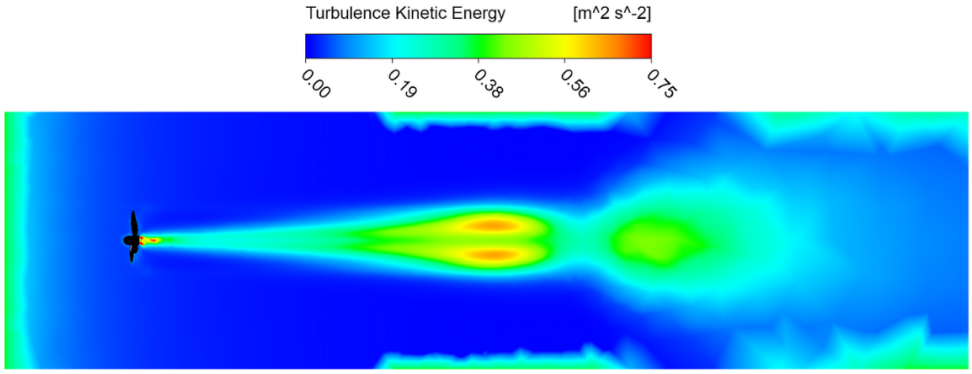

Figure B.11 – Turbulent kinetic energy field downstream of the 30° backward-swept blade turbine rotor.

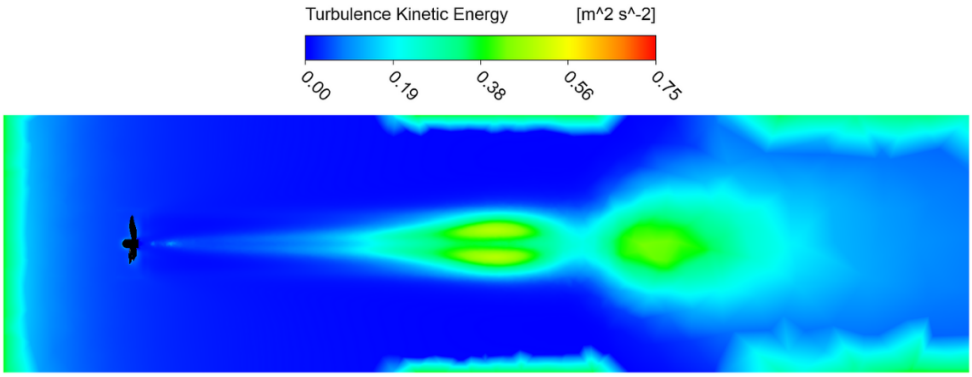

Figure B.12 – Turbulent kinetic energy field downstream of the 10° forward-swept blade turbine rotor.

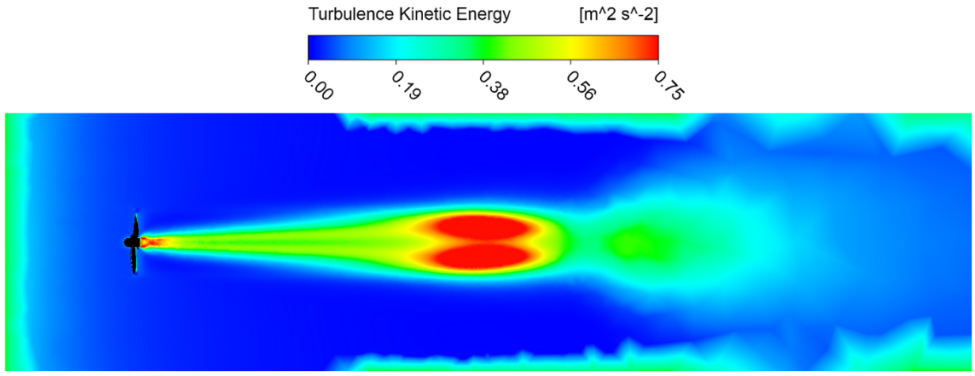

Figure B.13 – Turbulent kinetic energy field downstream of the 20° forward-swept blade turbine rotor.

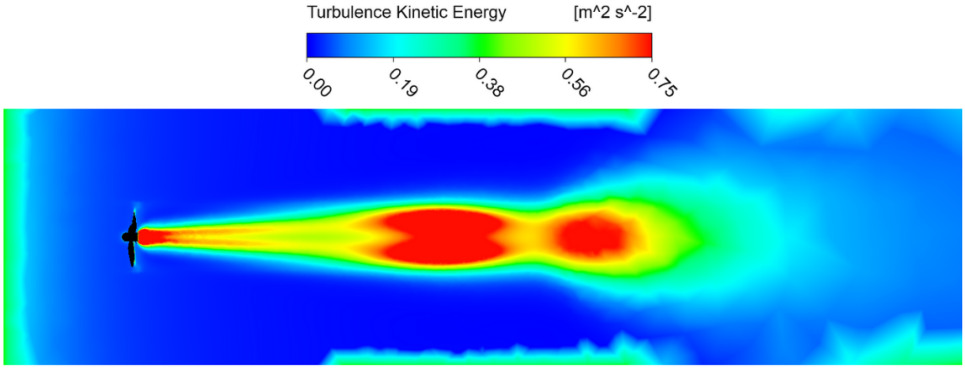

Figure B.14 – Turbulent kinetic energy field downstream of the 30° forward-swept blade turbine rotor.

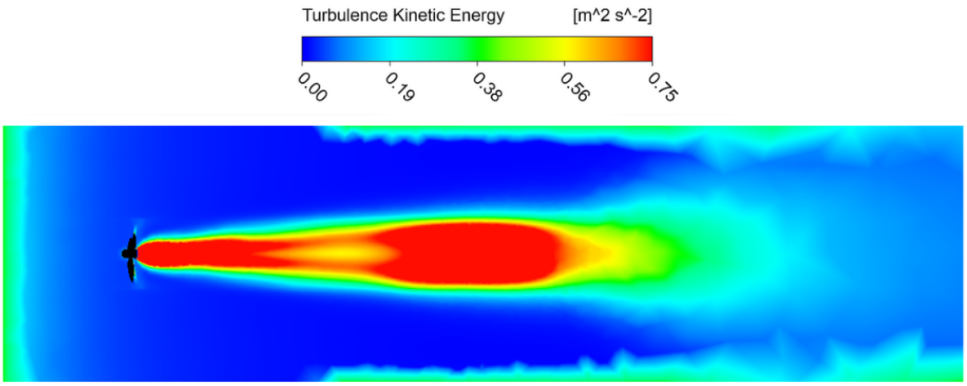

Appendix C – Projected surface streamlines on rotor blades

This appendix presents the velocity streamline plots on the surfaces of the turbine models analyzed in this work under steady-state conditions. These visualizations allow for a detailed assessment of near-wall flow behavior, highlighting regions of flow attachment, boundary layer development, and potential flow separation. The plots compiled here complement the results discussed in chapter 3. By comparing the streamline patterns across different blade geometries, it is possible to identify the influence of sweep angles on aerodynamic loading, flow organization, and the overall stability of the boundary layer along the blade span.

Figure C.1 – Velocity streamlines on the surface of the straight-bladed turbine model.

(a) Pressure side (b) Suction side

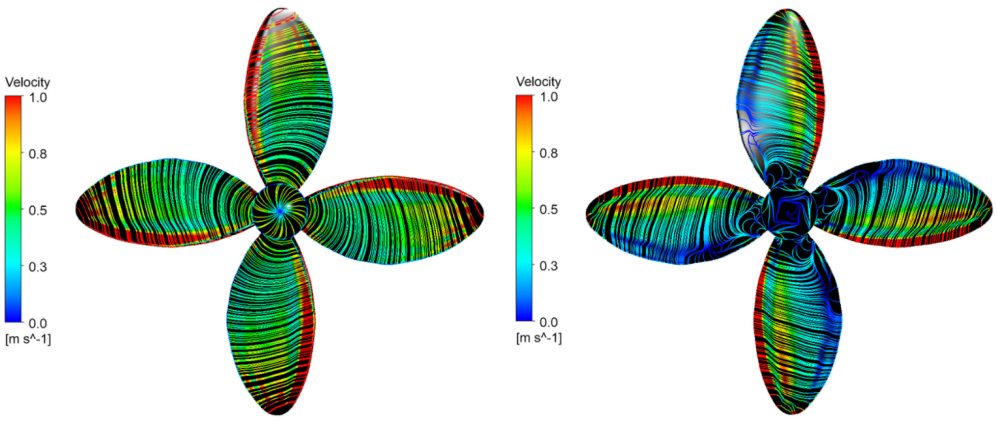

Figure C.2 – Velocity streamlines on the surface of the 10° backward-swept blade turbine model.

(a) Pressure side (b) Suction side

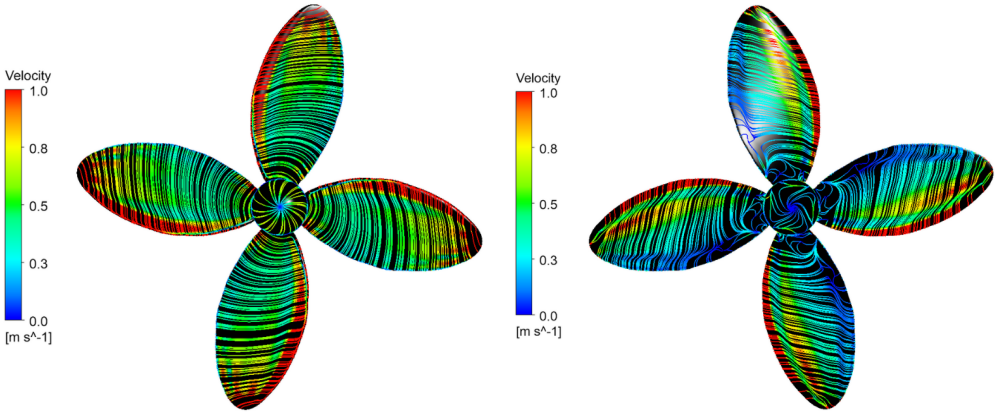

Figure C.3 – Velocity streamlines on the surface of the 20° backward-swept blade turbine model.

(a) Pressure side (b) Suction side

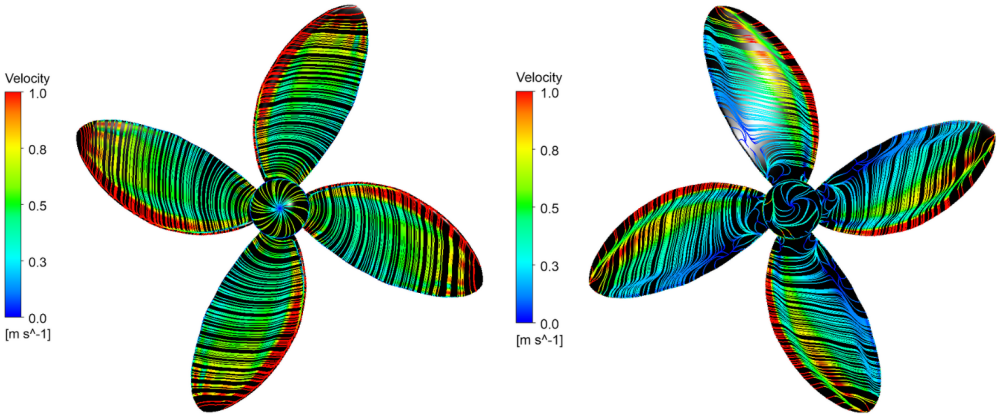

Figure C.4 – Velocity streamlines on the surface of the 30° backward-swept blade turbine model.

(a) Pressure side (b) Suction side

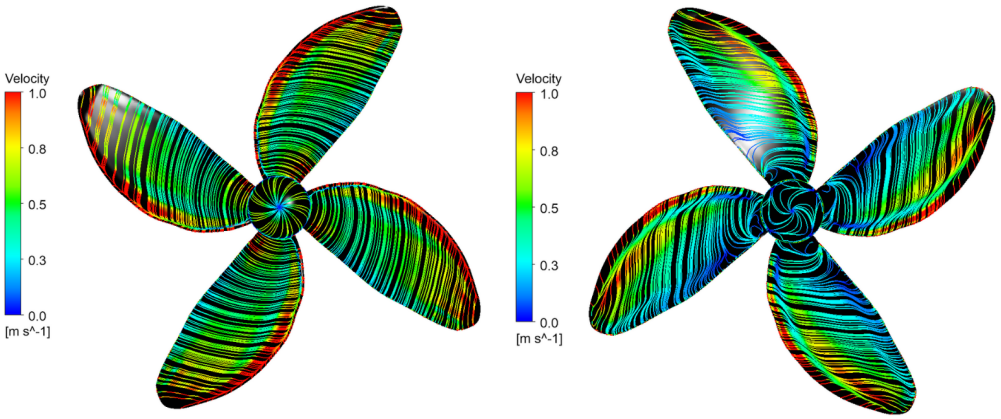

Figure C.5 – Velocity streamlines on the surface of the 10° forward-swept blade turbine model.

(a) Pressure side (b) Suction side

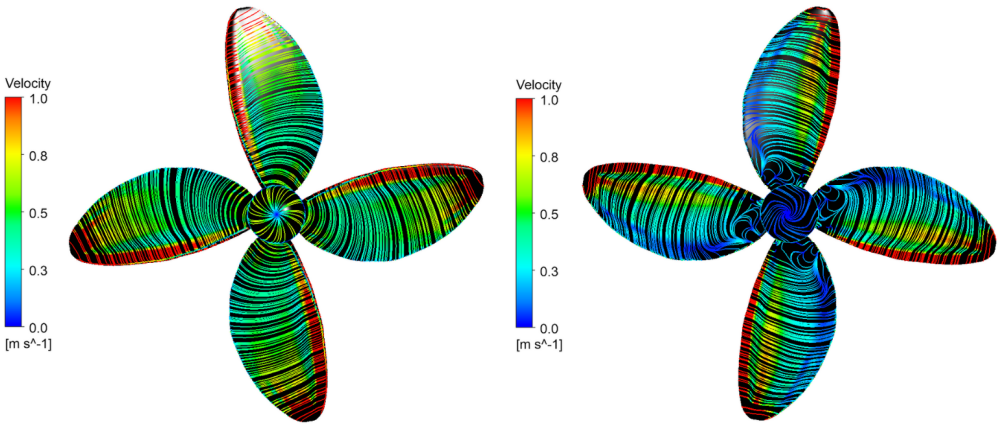

Figure C.6 – Velocity streamlines on the surface of the 20° forward-swept blade turbine model.

(a) Pressure side (b) Suction side

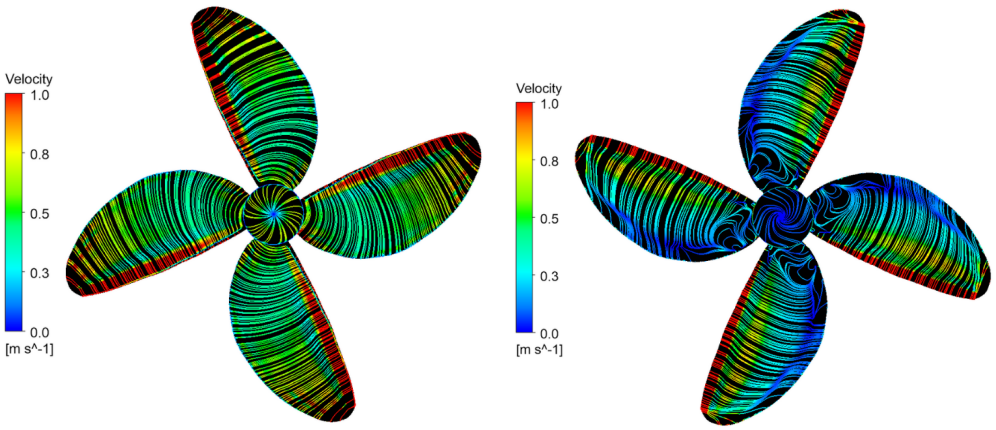

Figure C.7 – Velocity streamlines on the surface of the 30° forward-swept blade turbine model.

(a) Pressure side (b) Suction side

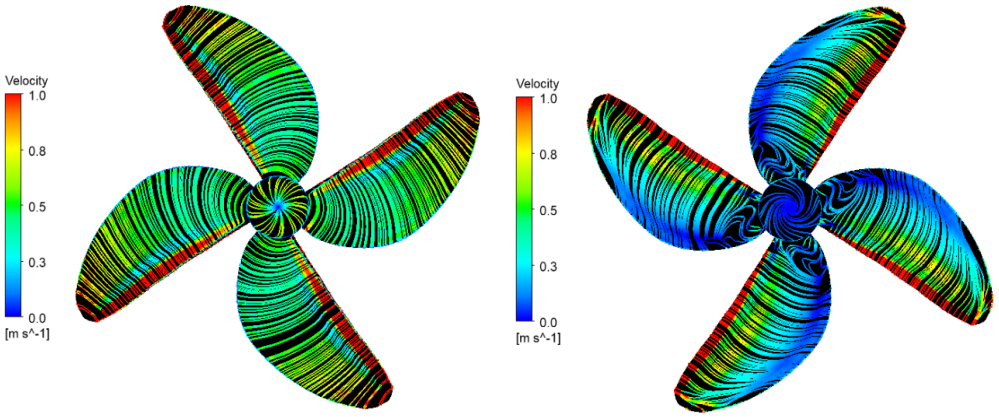

Appendix D – Wall shear vectors on the turbines' surfaces

This appendix presents the wall shear vector plots on the surfaces of the turbine models analyzed in this study. These plots provide insights into the distribution of shear stresses along the blades, enabling the identification of regions of strong flow attachment, boundary layer separation, and recirculation. The plots compiled here complement the results discussed in chapter 3. By comparing the shear vector patterns across different geometrical configurations, it is possible to evaluate the effects of sweep angles on near-wall aerodynamic behavior and their implications for turbine efficiency and stability.

Figure D.1 – Wall shear vectors on the surface of the straight-bladed turbine model.

(a) Pressure side (b) Suction side

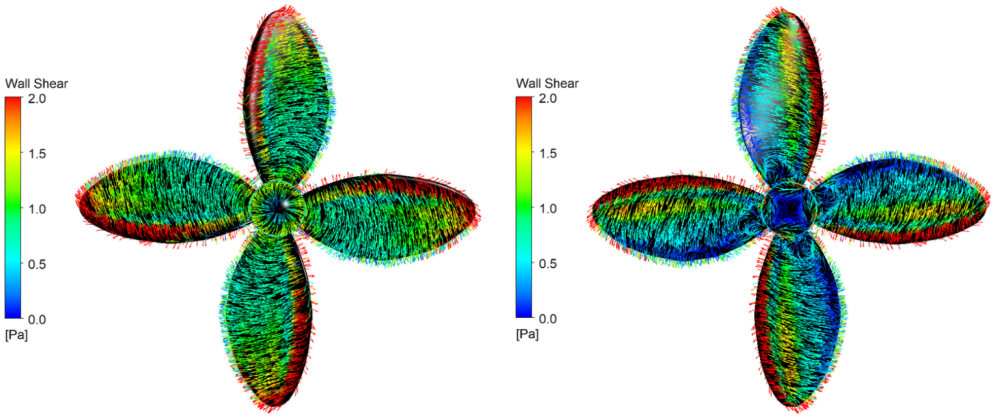

Figure D.2 – Wall shear vectors on the surface of the 10° backward-swept blade turbine model.

(a) Pressure side (b) Suction side

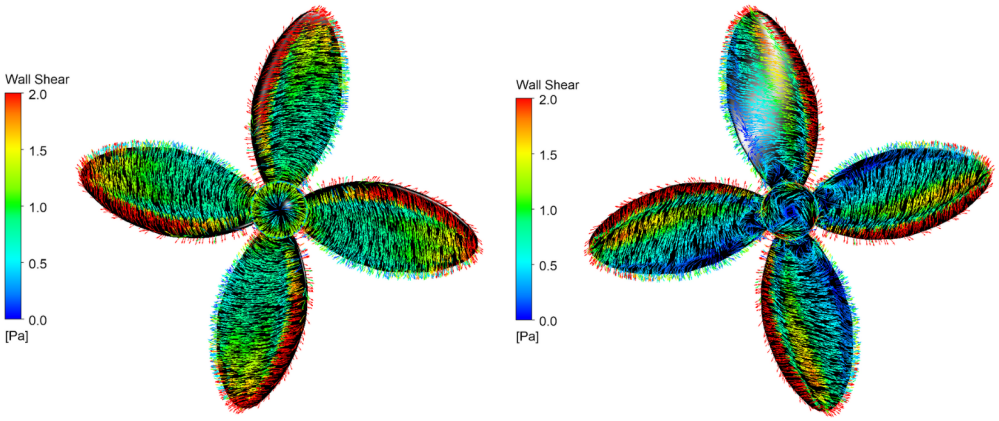

Figure D.3 – Wall shear vectors on the surface of the 20° backward-swept blade turbine model.

(a) Pressure side (b) Suction side

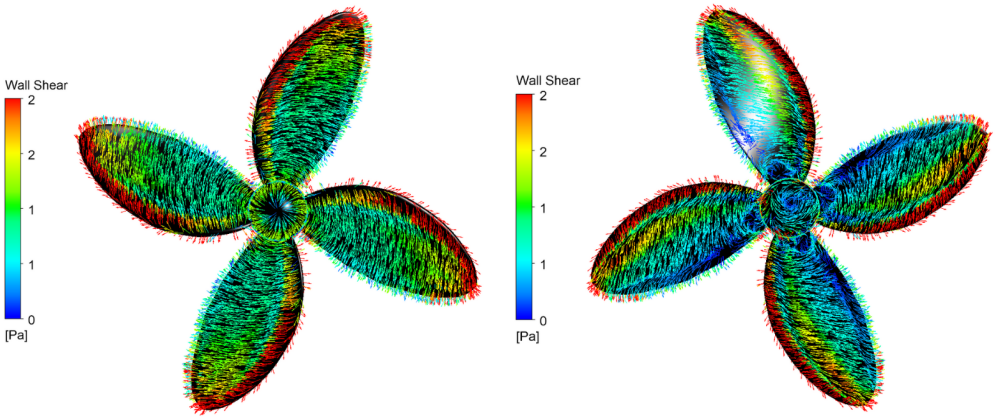

Figure D.4 – Wall shear vectors on the surface of the 30° backward-swept blade turbine model.

(a) Pressure side (b) Suction side